UNIVERSITÀ DEGLI STUDI DI CAGLIARI

DOTTORATO DI RICERCA IN FISICA FISICA NUCLEARE,
SUBNUCLEARE E ASTROFISICA
Ciclo XXV

Light vector meson production at forward rapidity in pp collisions at the LHC with the ALICE detector

Settore scientifico disciplinare di afferenza
FIS/04

Presentata da:	Elisa Incani
Coordinatore Dottorato:	Prof. P. Ruggerone
Relatori:	Dr. A. De Falco
	Prof. G. Usai

Esame finale anno accademico 2011-2012

Quas ob res ubi viderimus nil posse creari
de nihilo, tum quod sequimur iam rectius inde
perspiciemus, et unde queat res quaeque creari,
et quo quaeque modo fiant opera sine divom.
Nam si de nihilo fierent, ex omnibus rebus
omne genus nasci posset, nil semine egeret.
Titus Lucretius Carus: De rerum natura,
I, 155-160, 55 B.C.

Contents

Introduction

The aim of this thesis is to study the ϕ and ω production with the data collected by the ALICE experiment in proton-proton collisions at $\sqrt{s} = 7$ and $\sqrt{s} = 2.76$ TeV via dimuon channel in the rapidity range $2.5 < y < 4$.

The ALICE experiment at the LHC is dedicated to study the Quark-Gluon Plasma (QGP) produced in heavy-ion collisions.

Low-mass vector mesons (ρ, ω and ϕ) give us information on the hot and dense state of strongly interacting matter produced in these collisions. In fact in the QGP an enhancement of the strange particle production should be present (strangeness enhancement), which means a $N_\phi/N_{\rho+\omega}$ ratio increasing in A-A collisions with respect to pp collisions. On the other side, the measurement of the ρ spectral function can be used to reveal in-medium modifications of the hadron properties close to the QCD phase boundary. pp collisions provide a reference for these studies. Vector meson production in pp collisions is also useful by itself, to study soft Quantum ChromoDynamics (QCD) in the LHC energy range, since calculations in this regime are based on QCD inspired phenomenological models that must be tuned to the data.

The data analyses in this thesis include a sample collected by the ALICE experiment during the year 2010 at 7 TeV and in 2011 at 2.76 TeV. The mesons are detected via dimuon channel using the ALICE muon spectrometer.

The first step of this analysis was to describe the dimuon mass spectrum in the low-mass region ($m < 1.4$ GeV/c^2) as a superposition of various sources. The yield of the ϕ and $\rho + \omega$ meson was then extracted as a function of p_T and rapidity.

We have measured the ratio $N_\phi/N_{\rho+\omega}$ vs p_T, the ratios $\sigma_\rho/\sigma_\omega$ and $\sigma_\phi/\sigma_\omega$, and the ϕ and ω p_T and rapidity differential cross sections for the data sample at 7 TeV. For the data sample at 2.76 TeV, because of the limited statistics, we have evaluated only the $N_\phi/N_{\rho+\omega}$ ratio and ϕ and ω integrated cross sections.

In Chapter 1 a brief description of QGP properties and its experimental probes in the low-mass region is given, together with previous measurements of the ϕ production in A-A collisions and the models for pp collisions.

In Chapter 2, after an introduction to the LHC accelerator and the main experiments at the LHC, a description of the ALICE detector layout is carried out.

In Chapter 3, after an introduction to the dominant processes in the low-mass region, the *hadronic cocktail* Monte Carlo generator is described.

In Chapters 4 and 5 the analysis at 7 TeV and 2.76 TeV respectively is illustrated.

Finally in Chapter 6 our results are compared with theoretical models and other measurements.

1

Interest of vector meson study

Contents

A Quark-Gluon Plasma (QGP) is a phase of quantum chromodynamics (QCD) which exists at extremely high temperature and/or density. In this phase the quarks and gluons are deconfined.

Relativistic nucleus-nucleus collision can provide the ideal conditions for the achievement of the QGP phase.

The ALICE experiment has been designed to study the physics of strongly interacting matter in these collisions at the LHC.

Low-mass vector meson (ρ , ω, ϕ) production provides key information on the hot and dense state of strongly interacting matter produced in high-energy heavy ion collisions. Among the possible signatures of QGP formation, strangeness enhancement can be accessed through the measurement of ϕ meson production, while the measurement of the ρ spectral function can be used to reveal in-medium modifications of hadron properties close to the QCD phase boundary. Vector meson production in pp collisions provides a reference for these studies. Moreover, it is interesting by itself, since it provides insight into soft QCD processes in the LHC energy range. Calculations in this

regime are based on QCD inspired phenomenological models that must be tuned to the data.

In this chapter I will show a brief description of QGP and its experimental probes in the low-mass region, the previous measurements of the ϕ production in nucleus-nucleus collisions and the models for pp collisions.

1.1 QGP

In the theory of strong interactions, the Quantum ChromoDynamics (QCD) predicts a phase transition at high temperature and/or energy density between hadronic matter, where quarks and gluons are confined inside hadrons and a deconfined state of matter, the so-called quark-gluon plasma (QGP).

The possible phases of strongly interacting matter can be displayed in a phase diagram as a function of its temperature T and the net baryon number density (the number of nucleons minus that of antinucleons, per unit volume). The latter is generally specified by the corresponding baryo chemical potential μ.

In Fig. 1.1 [1] there is a phase diagram of strongly interacting matter which shows a four-phase structure: one confined and three deconfined states.

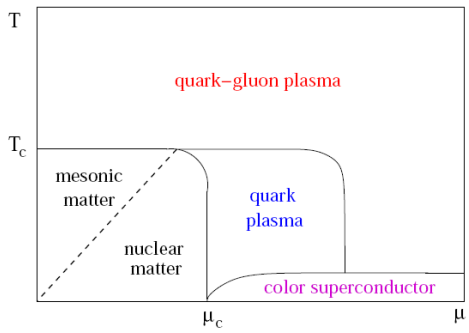

Figure 1.1: The phase diagram of strongly interacting matter.

Along the μ axis, for $T = 0$ the cold nuclear matter is compressed; for $\mu = 0$, along the T axis the matter is been heated and the overall baryon density is null, since mesons with an equal number of baryons and anti-baryons are contained together. For low T and μ the hadronic matter is confined. Increasing T and/or μ, the deconfinement is

approached: at high temperatures (for $T_c \gtrsim 0.17$ GeV, where there is a deconfinement transition coincident with an associated shift in the effective quark mass) we have a phase consisting of unbound colored quarks and gluons, the quark-gluon plasma; at high baryon density and low temperatures the liberated quarks might keep their mass for a certain range of baryon density, which would lead to a phase of unbound massive quarks, and they can choose, once deconfined, to recombine into massive colored quark pairs (locally bound bosonic *diquarks*). At very low temperature the diquarks could condense, behaving as a color superconductor. Increasing the temperature, it is recovered either the massive quark phase or the quark-gluon plasma, both behaving as normal color conductors.

The idea is that high energy nuclear collisions produce droplets of strongly interacting matter, large enough and long lived enough to allow a study of the predictions which QCD makes for macroscopic systems. Moreover, it is expected that the conditions provided in these interactions will suffice for QGP formation.

Before describing the time evolution of heavy-ion collisions, I will speak of another phase transition that may occur in the high energy nuclear collisions, the *chiral symmetry restoration*.

1.1.1 Chiral Symmetry Restoration

The chiral symmetry is a possible symmetry of the Lagrangian of QCD that can be decomposed into independent left- and right-handed massless spin one-half components. Massless fermions possess chiral symmetry, whereas in the case of massive fermions, these two components of the Lagrangian are mixed.

When the quarks are confined in hadrons, they take, through *dressing* with gluons, an effective *constituent quark* mass, and because the quarks in the Lagrangian of QCD are almost massless, the mass of the constituent quarks in the confined phase is generated spontaneously (*chiral symmetry breaking*), though the confinement interaction itself. Hence when deconfinement occurs, this additional mass is *lost* and the quarks return to the intrinsic mass that they had in the Lagrangian (*chiral symmetry restoration*).

So the effective mass of quarks is expected to change between the confined and deconfined phases; a shift in the effective quark mass is thus a further transition to look for as the density of strongly interacting matter is increased.

Remembering Fig.1.1, when the hadrons are dissolved into their quark constituents, the liberated quarks could still retain a non-vanishing effective mass, remaining massive constituent quarks. This would mean that deconfinement and chiral symmetry restoration do not coincide, since the remaining quark mass implies a continuation of chiral symmetry breaking, hence, a priori, they need not end simultaneously. However, rather basic arguments suggest that chiral symmetry restoration occurs either together with or after color deconfinement [2].

1.1.2 Time evolution of heavy-ion collisions

A schematic view of the time evolution of heavy-ion collisions is shown in Fig. 1.2. The first stage of the collision is characterized by hard interactions at the partonic level. Then a thermalized phase may take place with the formation of the QGP; the fireball expands, giving rise to the hadronization process that ends with the freeze-out.

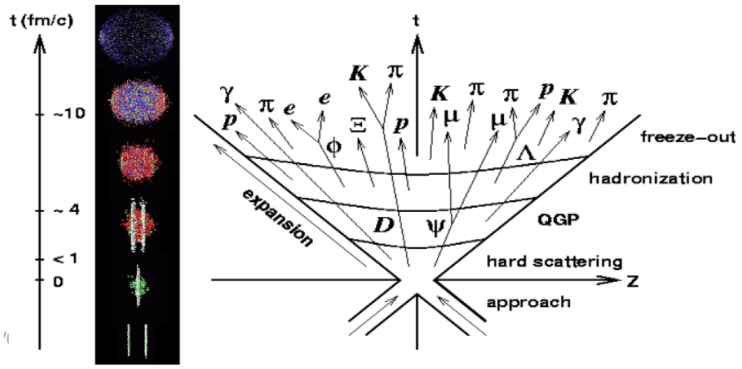

Figure 1.2: Schematic view of the time evolution of A-A collisions.

1.1.2.1 Before the QGP formation

The energetic particles produced by primary parton collisions interact with the medium itself (behaving as penetrating probes: *external probes*), indicating, by their observed behavior, if the subsequent medium was deconfined or not. These probes are:

- Quarkonium states (J/ψ, ψ', $\Upsilon(1S)$, $\Upsilon(2S)$, $\Upsilon(3S)$);
- Open heavy flavors (charm and beauty);
- Jets.

The quarkonia are useful probes for the QGP, because it is possible to dissociate them in a deconfined medium through interaction with hard gluons in hadrons, giving rise to the *quarkonia suppression* [1, 3]. [1]

The measurement of open heavy-flavor hadrons may probe the energy density of the system through the mechanism of in-medium energy loss of heavy quarks [4].

The other probes used to obtain information about the dynamical behavior of the QGP are the hadron jets, the fragmentation products of high transverse momentum partons. Also the jets, as open heavy flavors, lose energy in the high density medium with the gluon radiation and multiple collisions. These phenomena are known as *jet quenching* [5].

1.1.2.2 Thermalization, expansion and hadronization

The particles produced in the primary collisions continue to interact, creating a region of high matter and energy density at the thermal equilibrium where the QGP may be produced in less than $0.1 - 0.3$ fm/c (thermalization).

At the QGP formation energy, due to the chyral symmetry restoration, the mass of s quarks is lower ($m_s \sim 150$ MeV/c^2) than the constituent mass ($m_s \sim 450$ MeV/c^2). For this reason in heavy-ion collisions the production of the s quark and, as a consequence, of the strange hadrons should increase with respect to pp collisions.

At this point the termalized system expands and the energy density decreases. Then, when it reaches again the critical density, the hadronization phase starts and the formation of the first bound states begins. In this phase, while the temperature has a small variation (it is still $\sim T_c$), the energy density quickly decreases and the volume of the fireball increases.

1.1.2.3 Chemical and kinetical freeze-out

When the energy of collisions is too small to cause inelastic processes, the quantity of hadron species cannot change, then the abundances are fixed and the chemical freeze-out is reached. Therefore the ratio between particles species (e.g. K/π and p/π), by now determinated, can give us information on the system, but the kinematic properties of hadrons continue to modify for the elastic interactions. Only when the distances

[1] At very high energy, statistical recombination of $c\bar{c}$ pairs ($\sim 10^2$ pairs are expected in central Pb-Pb collisions at the LHC) could lead to an increase of J/ψ production, rather than suppression.

between hadrons are larger than the range of the interaction, the elastic collisions stop and the kinetical freeze-out is reached. Then the kinematical distribution of the hadrons is able to give us information on the kinetic freeze-out temperature.

1.2 Experimental probes of QGP accessible through low-mass dileptons

Correlated dileptons provide a probe of the expanding system at an early stage and are very useful since they retain the primary information of the system for the absence of any final state interaction. I will focus my attention to the low mass region, and more in detail to the light vector mesons ρ, ω and ϕ.

The ρ meson is a primary signature for chiral symmetry restoration [6–8], due to its strong coupling to the $\pi\pi$ channel and its short life time of only 1.3 fm/c, much shorter than the lifetime of the fireball created in a heavy-ion collision.

The ϕ carries information about strangeness production. In particular, if a phase transition to a QGP state takes place, one would expect an enhancement in the yields of strange and multi-strange particles in nucleus-nucleus reactions compared to those from proton-proton interactions.

Among these probes, we are interested to the ϕ meson and below I will describe the strangeness enhancement and previous measurements in heavy-ion collisions.

1.2.0.4 ϕ and strangeness enhancement

The OZI (Okubo-Zweig-Iizuka) rule states that the processes with disconnected quark lines in the initial and final state are suppressed, and for this reason the ϕ meson production is suppressed in elementary collisions [9–11]. But in heavy-ion collisions, due to the strange quark abundance, the ϕ mesons may be produced though coalescence, bypassing the OZI rule [12]. Therefore the ϕ meson has been predicted to be a probe of the QGP [13–18].

Also the ϕ may be a signature of the restoration of chiral symmetry in the nuclear medium, changing its mass and width [19–21]. Asakawa and Ko [22] and Song [23] predicted a decrease of the ϕ mass with respect to its pole mass value in the deconfinement state, and other calculations have predicted a double ϕ peak structure in the dilepton invariant mass spectrum in relativistic heavy-ion collisions [24].

1.2.0.5 Previous measurements in heavy-ion collisions of the ϕ meson

The ϕ production in heavy-ion collisions was studied extensively in fixed target experiments at the SPS with a beam energy of 158 A GeV by several experiments: NA49, CERES/NA45, NA50 and NA60. NA49 measured ϕ production in C-C, Si-Si and Pb-Pb in the $\phi \to K^+K^-$ channel, NA50 studied the low-mass region in the dimuon channel in Pb-Pb collisions and CERES accessed the ϕ meson both through e^+e^- and K^+K^- pairs in Pb-Au collisions; NA60 has studied simultaneously the leptonic and charged kaon decay modes of the ϕ in In-In collisions.

At the Relativistic Heavy Ion Collider (RHIC) vector meson production has been studied by the STAR and PHENIX experiments via the kaon decay channel in Au-Au and Cu-Cu at $\sqrt{s_{NN}} = 200$ GeV per nucleon. The latest measurements come from the ALICE experiment in Pb-Pb collisions at $\sqrt{s_{NN}} = 2.76$ TeV per nucleon via kaon channel.

1.2.0.6 The CERN experiments at the SPS

NA49 and NA50 studied the ϕ meson production, using two different decay channels, $\phi \to K^+K^-$ and $\phi \to \mu^+\mu^-$ respectively [25, 26]. NA49 measures the ratio $\langle\phi\rangle/\langle\pi\rangle$, while NA50 accesses the quantity $\langle\phi\rangle/(\langle\rho\rangle+\langle\omega\rangle)$. Also the inverse slope parameter T_{eff}, obtained fitting the ϕ p_T distributions with the form $1/p_T dN/dp_T = e^{-\sqrt{p_T^2+m^2}/T_{eff}}$, has been measured by the two experiments. Both results show an increase of these ratios as a function of the number of participants N_{part}, but there is a disagreement between the two experiments about the ϕ multiplicity and the values of T_{eff}. These discrepancies are known as the "ϕ puzzle" [27, 28]. A possible explanation for this discrepancy is that the kaons are susceptible to absorption and rescattering in the medium, that may produce a loss of signal in the kaon channel, reducing the observed yield. This effect should be higher at low p_T [28]. Subsequently CERES has studied the ϕ meson using both channels: charged kaons and dileptons (e^+e^-) [29]. The CERES results are in good agreement with the results from NA49 measured in the kaon channel. The last experiment at SPS that has studied the ϕ meson in heavy ion collisons is NA60 [30]. Also this experiment studied the ϕ meson in both decay channel: kaon channel and dileptons ($\mu^+\mu^-$).

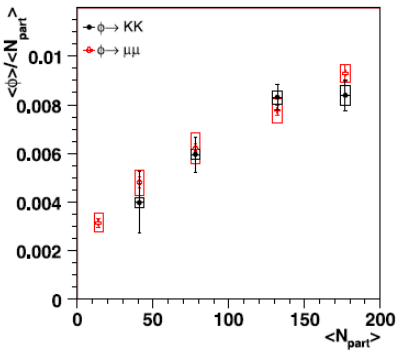

Figure 1.3: $\langle\phi\rangle/\langle N_{part}\rangle$ as a function of the number of participants in InIn collisions in the $\phi \to K^+K^-$ (full circles) and $\phi \to \mu^+\mu^-$ (open crosses) channels for $p_T > 0.9$ GeV/c measured by NA60.

The ratio $\langle\phi\rangle/\langle N_{part}\rangle$ measured by NA60 as a function of N_{part} in the kaon channel for $p_T > 0.9$ GeV/c is shown in Fig.1.3, compared to the corresponding one in dimuons. It is possible to see a good agreement within the errors in both channels. The comparison between the measurements of all these experiments is shown in Fig. 1.4. In the top panel we can see T_{eff} as a function of the number of participants, showing an initial fast increase at low N_{part} values and a less pronounced one going to higher N_{part}. The NA50 results do not seem to follow the same systematics as the other experiments. In the bottom of Fig. 1.4 the ratio $\langle\phi\rangle/\langle N_{part}\rangle$ in full p_T range as a function of N_{part} shows an increase with the number of participants. All experiments do not show differences between the dilepton and kaon channel, with the exception of the NA50 result.

1.2.0.7 The RHIC experiments

The Relativistic Heavy Ion Collider (RHIC), located at the Brookhaven National Laboratory (BNL) has collected data in pp, d-Au, Cu-Cu and Au-Au collisions. The two biggest experiments are STAR and PHENIX.

As a first step I will present results for the measurement of ϕ meson production via its charged kaon decay channel $\phi \to K^+K^-$ in Au-Au, Cu-Cu, pp and d-Au collisions at $\sqrt{s_{NN}} = 62.4$ GeV and $\sqrt{s_{NN}} = 200$ GeV from the STAR experiment. The pp and p-A collisions serve as a robust reference baseline for the heavy-ion data.

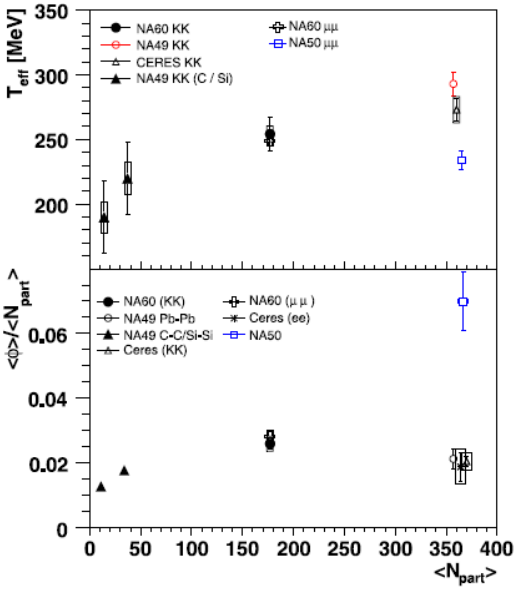

Figure 1.4: Inverse slope (top) and $\langle\phi\rangle/\langle N_{part}\rangle$ in full p_T range (bottom) as a function of N_{part} for central collisions.

In the following the main results are briefly summarized. Information on radial flow, obtained through the measurement of $\langle p_T\rangle$, is useful because, since the ϕ meson is weakly coupled to the hadron medium, its radial flow will be mostly from the partonic stage. From Fig. 1.5 it can be observed that the $\langle p_T\rangle$ of the ϕ (and hyperons) does not follow the $\langle p_T\rangle$ vs mass trend determined by π, K and $\overline{p}$, which may indicate that ϕ and strange baryons retain more information from the early stages of collision.

The p_T spectra, reported in Fig. 1.6 in central Au-Au collisions are well described by an exponential, while the spectra for pp, d-Au and most peripheral Au-Au collisions are better fitted by a Lévi-Tsallis function, that describes more accurately the high-p_T tails. This indicates that the environment created in central Au-Au collisions favors the production of soft ϕ mesons.

The most important tool to probe the production dynamics and hadronization process in relativistic heavy-ion collisions is the nuclear modification factor R_{AB}.

R_{AB} is the yield ratio of nucleus (A) + nucleus (B) collisions to inelastic pp collisions

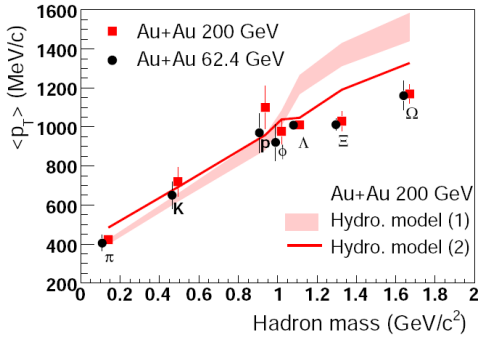

Figure 1.5: Hadron mass dependence of $\langle p_T \rangle$ in central Au-Au collisions at 62.4 and 200 GeV. The band and curve show two hydrodynamic model calculations for central Au-Au collisions at 200 GeV.

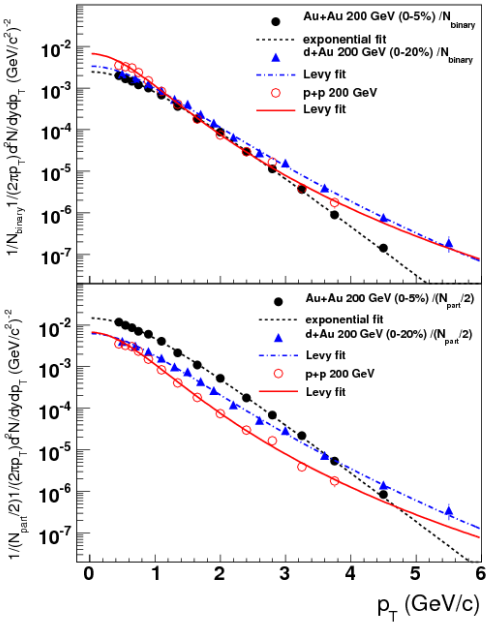

Figure 1.6: Comparison of transverse momentum spectra shape among different 200 GeV collision systems: Au+Au $(0-5\%)$, d-Au $(0-20\%)$ and pp (inelastic)). The spectra are normalized by $N_{part/2}$.

normalized by N_{part} or N_{bin}. The definition is:

$$R_{bin}^{AB}(p_T) = \frac{[dN/(N_{bin}dp_T)]^{AB}}{[dN/dp_T]^{pp}}, \tag{1.1}$$

This ratio should be unity if nucleus-nucleus collisions are just simple superpositions

of nucleon-nucleon collisions. On the other hand, deviations of these ratios from unity would imply contributions from nuclear or QGP effects.

Fig. 1.7 presents the ϕ R_{AA} as a function of p_T of Au-Au and Cu-Cu collisions at 200 GeV [31] for two centrality bins ($0-10\%$ and $20-30\%$).

For $0-10\%$, within the errors, $R_{AA}^{N_{part}}$ values show a similar shape and yields. On the other hand, a correspondence like that is not seen for other collision centralities and the Au-Au results are higher than Cu-Cu results for $p_T > 1$ GeV/c.

Besides, looking at the first bin of $R_{AA}^{N_{bin}}$, Cu-Cu is higher than Au-Au collisions for $p_T < 3$ GeV/c, and for $20-30\%$ central collisions $R_{AA}^{N_{bin}}$ is similar for both colliding systems. In the most central collisions both $R_{AA}^{N_{bin}}$ for $p_T > 3.5$ GeV/c are below unity, meaning that there is a parton energy loss in hot and dense medium formed in central heavy-ion collisions.

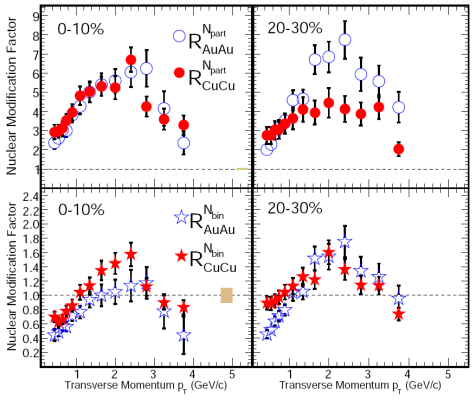

Figure 1.7: Nuclear modification factor as a function of p_T of ϕ mesons for $0-10\%$ and $20-30\%$ Cu-Cu and Au-Au collisions at $\sqrt{s_{NN}}$= 200 GeV.

Also the PHENIX experiment has performed systematic measurements of ϕ meson production in the K^+K^- decay channel at midrapidity in pp, d-Au, Cu-Cu and Au-Au collisions at $\sqrt{s_{NN}} = 200$ GeV[32].

Figure 1.8 shows the R_{AA} of the ϕ integrated for $p_T > 2.2$ GeV/c in Cu-Cu and Au-Au collisions versus N_{part}. In PHENIX no difference in the R_{AA} of ϕ between the two systems is found, i.e. it scales with the average size of the nuclear overlap, without considering the details of its shape.

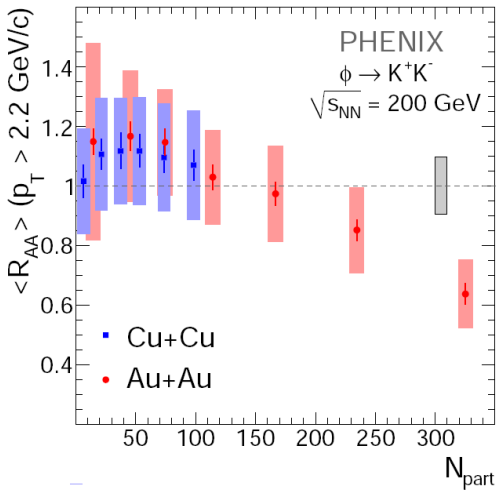

Figure 1.8: R_{AA} for ϕ integrated at $p_T > 2.2$ GeV/c in Cu-Cu and Au-Au collisions vs. N_{part} .

1.2.0.8 The ALICE experiment

The ϕ production has been studied by the ALICE experiment in Pb-Pb collisions at $\sqrt{s_{NN}} = 2.76$ TeV per nucleon via kaon channel, in the rapidity range $|y| < 0.5$ [33]. In Figure 1.9 the particle yield ratios ϕ/K^- and K^{*0}/K^- as a function of the mean number of participating nucleons ($\langle N_{part} \rangle$) is plotted. The ϕ/K ratio is flat, therefore it is independent from collision centrality, while the K^{*0}/K^- ratio shows a weak centrality dependence, that suggests a possible increase in rescattering in the most central collisions.

Figure 1.10 shows ϕ/K and ϕ/π as a function of beam energy dependence. The results are compared with the SPS [34] , RHIC [35, 36] and pp [37] measurements. It can be observed that the ratios are independent of beam energy.

1.3 Models for pp collisions

Vector mesons in pp collisions provide a reference for heavy ion collisions, as mentioned above. Moreover, they are interesting by themselves, since they are low-p_T processes that involve soft interactions, and cannot be treated in the frame of perturbative QCD.

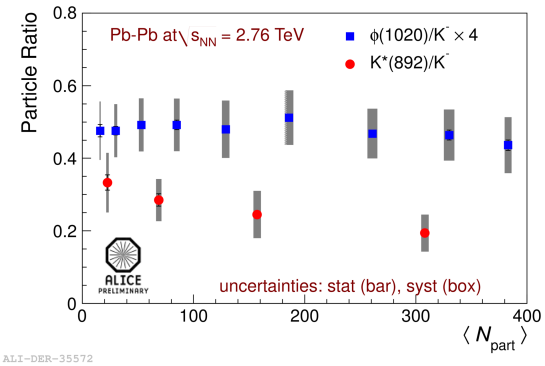

Figure 1.9: Particle ratios as a function of mean number of participating nucleons ($\langle N_{part} \rangle$) in Pb-Pb collisions at $\sqrt{s_{NN}} = 2.76$ TeV.

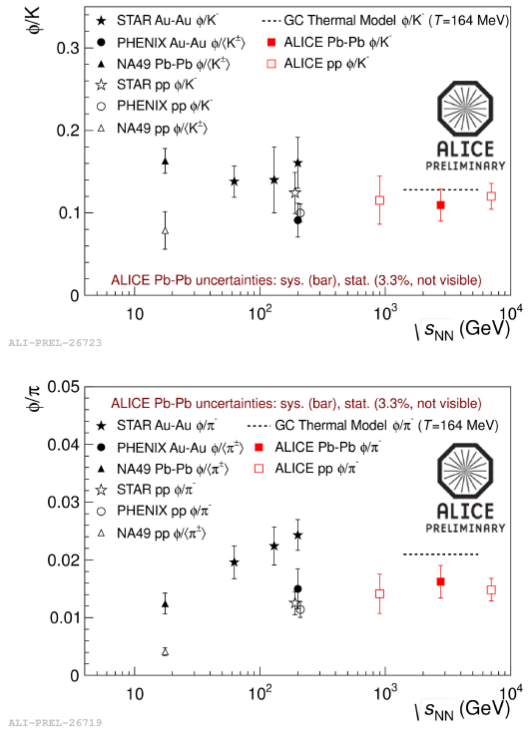

Figure 1.10: Particle ratios ϕ/K and ϕ/π as a function of beam energy.

In the absence of any reliable theoretical approach to the problem, the calculations are based on QCD inspired phenomenological models that must be tuned to the data.

Useful tools for the modeling of complex physics processes, as the vector meson

production in pp collisions, are the Monte Carlo (MC) event generators, that implement the state-of-the-art knowledge about QCD using numerical MC techniques [38].

In Chapter 6 we will compare the data analysed in this thesis to two event generators: PYTHIA [39] (in some commonly used tunes: Perugia-0 [40], Perugia-11 [41], ATLAS-CSC [42, 43] and D6T [44, 45]) and PHOJET [46, 47].

PYTHIA is a program that can be used to generate high-energy physics events, in particular for the collisions at high energies between elementary particles such as electron-positron, proton-antiproton and in their various combinations. Instead PHOJET is a program that simulates hadron-hadron, photon-hadron and photon-photon collisions. PYTHIA relies on multiple parton-parton interactions [39] to describe the non-perturbative phenomena, while PHOJET uses the Dual Parton Model [47]. As I have said before, the models must be tuned to the data, the data used by Perugia tunes include hadronic Z^0 decays at LEP, Tevatron min-bias data at 630, 1800, and 1960 GeV, Tevatron Drell-Yan data at 1800 and 1960 GeV, and SPS min-bias data at 200, 546, and 900 GeV. In addition Perugia-11 uses the early LHC data. The PYTHIA-D6T is tuned to the measurement of jets by CDF experiment, and PYTHIA-ATLAS-CSC, a tune developed by ATLAS collaboration, tune the minimum bias data from UA5, E735 and CDF experiments for energies ranging from 0.1 to 1.8 TeV. In the following we report some predictions based on these generators.

In figure 1.11 I report the cross section for ϕ and ω production evaluated with the different tunes of PYTHIA and PHOJET, calculated at $\sqrt{s} = 27.5$ GeV (corresponding to a typical SPS beam energy of 400 GeV in a fixed target experiment), 2.76 TeV, 7 TeV and 8 TeV.

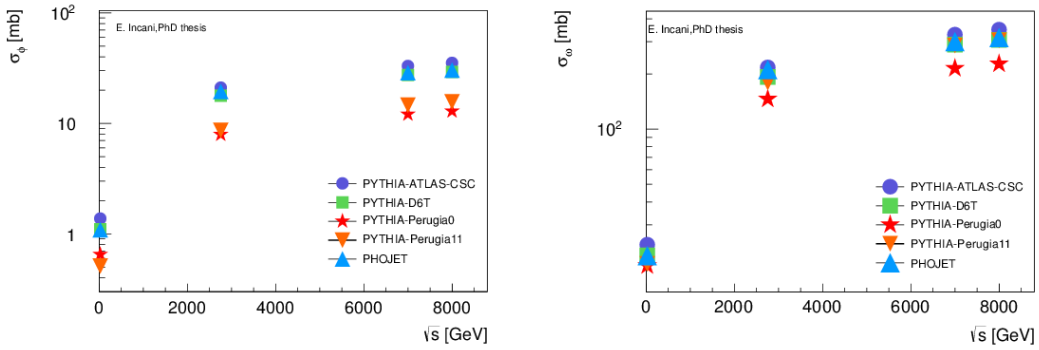

Figure 1.11: σ_ϕ and σ_ω in full phase space calculated with different event generators.

The cross sections increase with the energy for each generator with about the same rate, but the calculations show some differences: PYTHIA-ATLAS-CSC gives the highest value at every energy, while Perugia tunes give the lowest values. The highest value is about 2.7 times higher than the lowest value for the ϕ, and about 1.5 times higher for the ω.

In Fig. 1.12 the differential cross sections as a function of p_T at 7 TeV are displayed: for the ϕ, p_T distributions of Perugia tunes are slightly harder than the other ones, as this is better visible from the ϕ differential cross section normalized (Fig. 1.12 on the right); on the other hand, also the ω p_T distributions of PHOJET and D6T are harder than the ATLAS-CSC.

In Fig. 1.13 the differential cross sections as a function of rapidity are shown: PYTHIA-D6T has a plateau at mid-rapidity; on the other hand, the other generators give similar profiles with a smoothly decreasing cross section from mid to forward rapidities.

Moreover we can observe the shapes of rapidity distributions changing the range of p_T. In Fig. 1.14 the ϕ and ω differential cross sections, evaluated with PYTHIA Perugia-0, as a function of rapidity are shown: the shapes become narrower moving from low p_T to high p_T. On the other hand the p_T distributions have similar trend in different ranges of rapidity, as it is shown in Figure 1.15, where the ϕ and ω cross sections as a function of p_T, again evaluated with PYTHIA Perugia-0, are plotted.

In Table 1.1 the $[\sigma_\phi(2.5 < y < 4)/1.5]/\sigma_\phi(|y| < 0.5)$ and $[\sigma_\omega(2.5 < y < 4)/1.5]/\sigma_\omega(|y| < 0.5)$ ratios for all p_T and $p_T > 1$ GeV/c are listed, calculated using the different tunes of PYTHIA and PHOJET. The cross sections between 2.5 and 4 are divided by the width of the rapidity interval. Every simulation gives similar ratios and similar shapes to that shown in Figure 1.15, with the exception of PYTHIA D6T, that gives ratios higher than the other ones; on the other hand the D6T shapes are similar to the other p_T distributions.

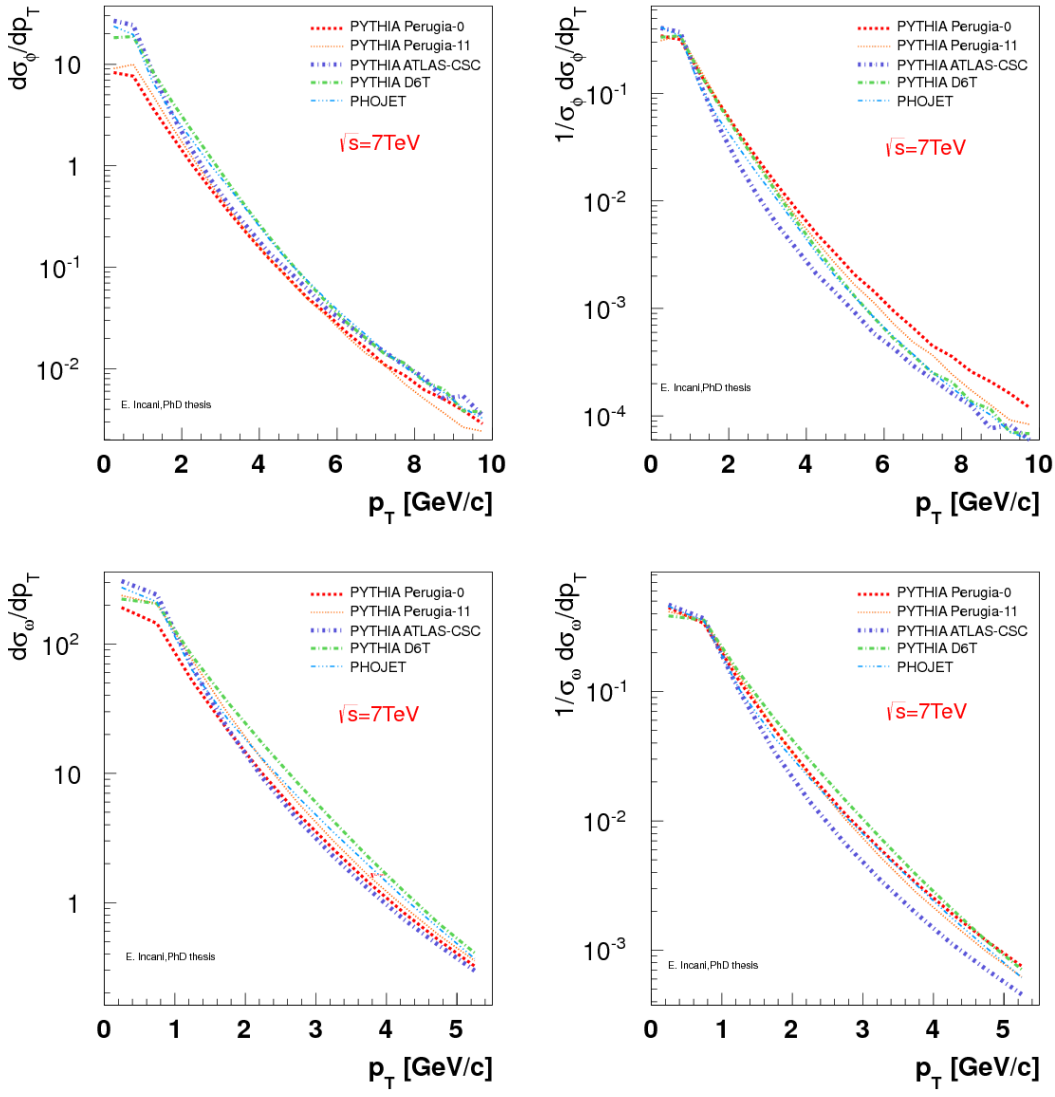

Figure 1.12: $d\sigma_\phi/dp_T$ and $d\sigma_\omega/dp_T$ in full phase space calculated with different event generators. In the top: at left $d\sigma_\phi/dp_T$, at right $1/\sigma_\phi d\sigma_\phi/dp_T$. In the bottom: at left $d\sigma_\omega/dp_T$, at right $1/\sigma_\omega d\sigma_\omega/dp_T$.

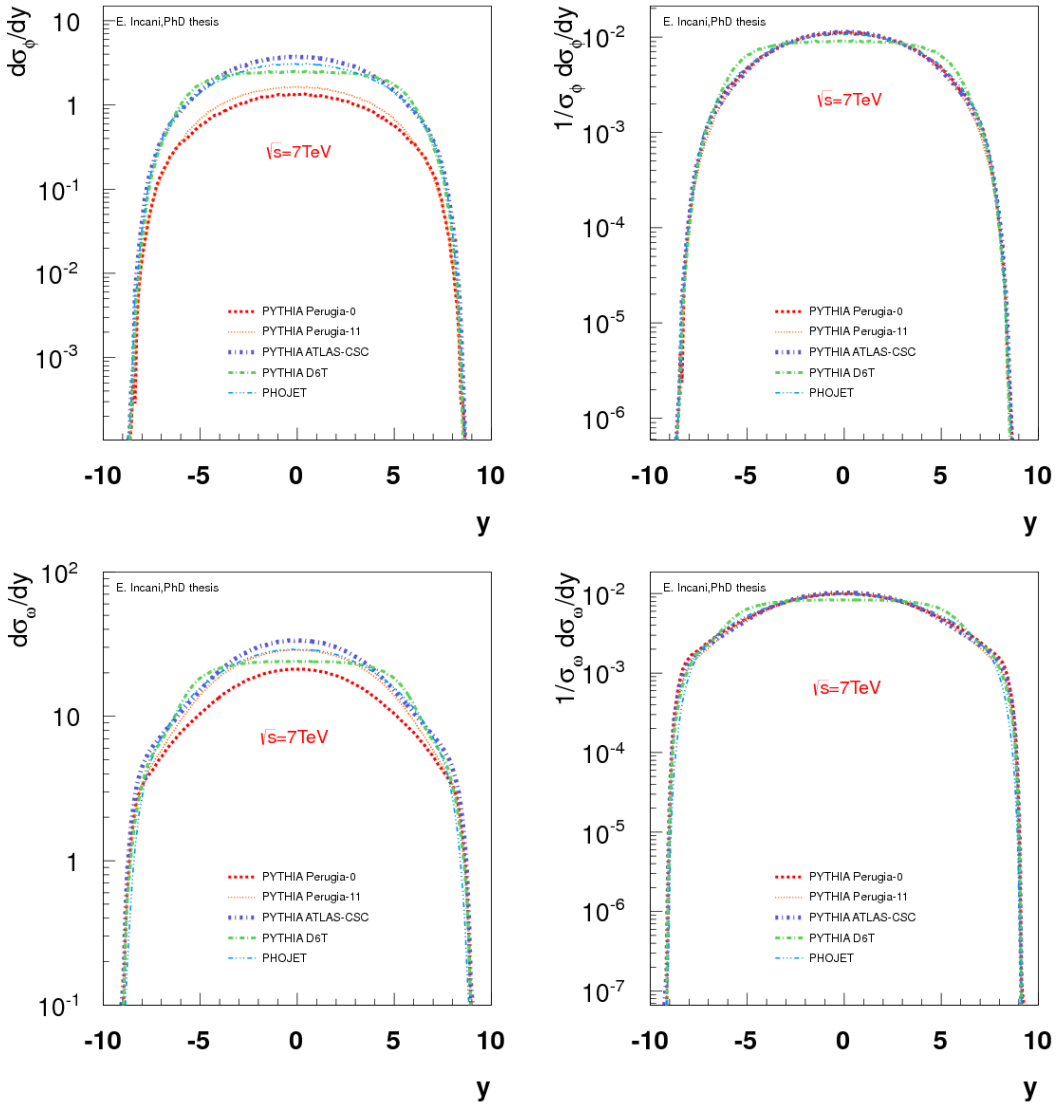

Figure 1.13: $1/\sigma_\phi \; d\sigma_\phi/dy$ and $1/\sigma_\omega \; d\sigma_\omega/dy$ in full phase space calculated with different event generators. In the top: at left $d\sigma_\phi/dy$, at right $1/\sigma_\phi d\sigma_\phi/dy$. In the bottom: at left $d\sigma_\omega/dy$, at right $1/\sigma_\omega d\sigma_\omega/dy$

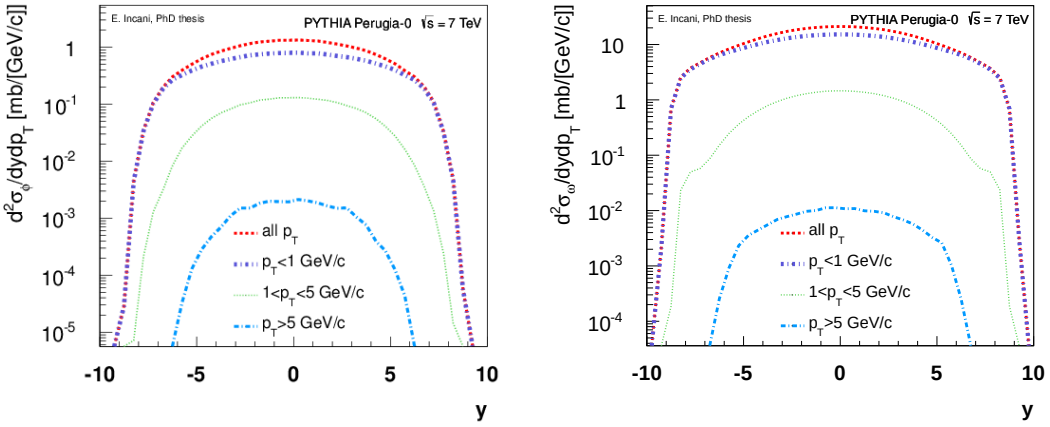

Figure 1.14: $d\sigma_\phi/dy$ (left) and $d\sigma_\omega/dy$ (right) in full phase space calculated with different p_T range.

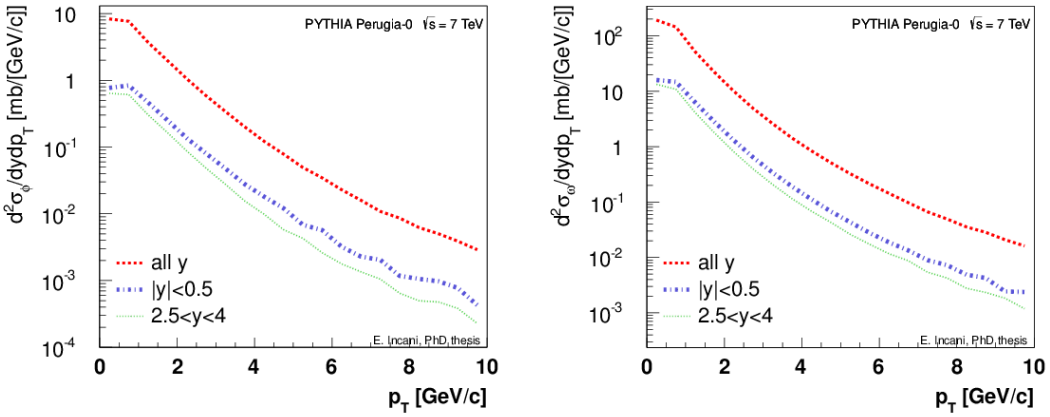

Figure 1.15: $d\sigma_\phi/dp_T$ (left) and $d\sigma_\omega/dp_T$ (right) calculated with different rapidity range.

Table 1.1: $[\sigma_\phi(2.5 < y < 4)/1.5]/\sigma_\phi(|y| < 0.5)$ and $[\sigma_\omega(2.5 < y < 4)/1.5]/\sigma_\omega(|y| < 0.5)$ calculated with PYTHIA with several tunes and PHOJET at $\sqrt{s} = 7$ TeV

	$[\sigma_\phi(2.5 < y < 4)/1.5]/\sigma_\phi(\|y\| < 0.5)$		$[\sigma_\omega(2.5 < y < 4)/1.5]/\sigma_\omega(\|y\| < 0.5)$	
	all p_T	$p_T > 1$ GeV/c	all p_T	$p_T > 1$ GeV/c
Perugia-0	0.72	0.63	0.75	0.64
Perugia-11	0.73	0.63	0.76	0.64
ATLAS-CSC	0.71	0.65	0.74	0.66
D6T	0.92	0.75	0.94	0.76
PHOJET	0.75	0.68	0.79	0.73

2

The ALICE experiment

Contents

ALICE (A Large Ion Collider Experiment) is one of the six experiments at the Large Hadron Collider at CERN [48]. It is optimized to study the physics of strongly interacting matter and the QGP at energy densities never accessed before in heavy ion collisions, through a set of experimental probes. Pb-Pb nuclei collisions are studied at a centre of mass energy of 2.76 TeV per nucleon. The resulting temperature and energy density are expected to be large enough to generate a QGP. ALICE also collects data in pp and p-A collisions, in order to provide a reference for measurements in heavy ion collisions.

The first pp collisions at a centre-of-mass energy of 7 TeV took place on 30th March 2010. Data at this kind of collisions were collected in the 2010 and 2011 and the record luminosity is $7.91 \times 10^{32}\mathrm{cm}^{-2}\mathrm{s}^{-1}$ (30 October 2011).

Pb-Pb collisions with an energy of 2.76 TeV per nucleon were exploited for a month in 2010 and for a month in 2011 and the record luminosity is $4.27 \times 10^{26}\mathrm{cm}^{-2}\mathrm{s}^{-1}$ (5 December 2011).

ALICE also collected data in pp collisions at 2.76 TeV (2011) and at 8 TeV (2012), and it is currently (beginning of 2013) running with p-Pb collisions.

In this chapter, after an introduction concerning the LHC acceleration facility and the main experiments at the LHC, a brief description of the ALICE detector layout is

carried out.

2.1 The Large Hadron Collider

LHC (Large Hadron Collider) is the largest collider in the world, with a circumference of 26.7 km [49]. It is housed in the tunnel of the previous LEP (Large Electron Positron) collider, constructed between 1984 and 1989. It is made of eight arcs and eight straight sections (see Figure 2.1). Each straight section is approximately 528 m long and can serve as an experimental or utility insertion. The experiments are located: at Point 1, the ATLAS experiment; at Point 5, the CMS experiment; at Point 2, the ALICE experiment and at Point 8, the LHCb experiment. The last two sections include also the injection systems for Beam 1 and Beam 2 respectively. The other straight sections do not have beam crossings: at Point 3 and 7 there are two collimation systems; at Point 4 there are two RF systems; Point 6 contains the beam dump insertion.

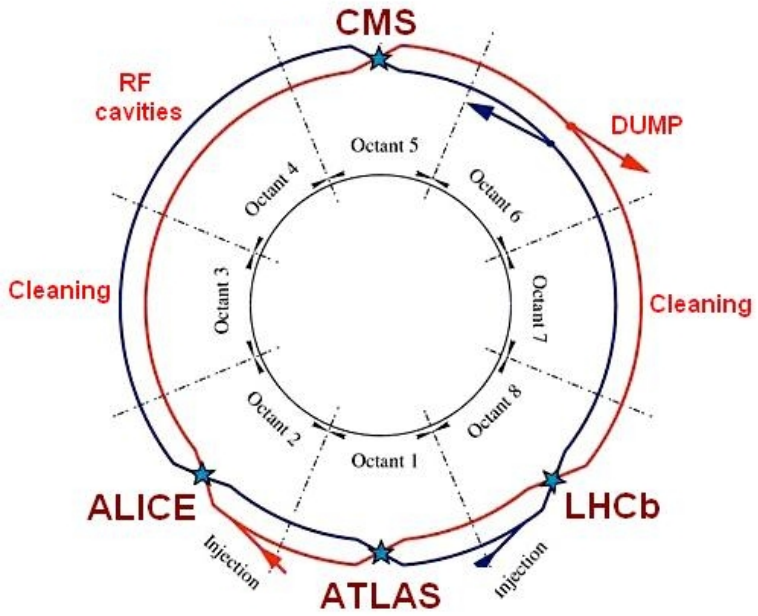

Figure 2.1: Schematic layout of the LHC.

The superconducting magnet system is the most arduous part in the LHC, it uses NbTi superconductors and operates at fields above 8 T. Magnets are cooled to a temperature below 2 K, using superfluid helium at atmospheric pressure.

LHC has the particularity of having not one, but three vacuum systems:

- insulation vacuum for cryomagnets;
- insulation vacuum for helium distribution line (QRL);
- beam vacuum.

The beam vacuum system is designed to take into account the requirements of 2 K operation and to protect the cryogenic system from heat sources. Three main heat sources have been identified and quantified at nominal intensity and energy:

- Synchrotron light radiated by the circulating proton beams;
- Energy loss by nuclear scattering;
- Image currents.

The injected beam is captured, accelerated and stored using a 400 MHz superconducting cavity system, and the longitudinal injection errors are damped using the same system.

The PS and SPS rings are used as injectors for the machine; in particular the SPS injects protons in the LHC ring with an energy of 450 GeV. The beams are accelerated in two separate rings, with intersections corresponding to the experiments.

The main experiments running at the LHC are:

- A Toroidal LHC ApparatuS (ATLAS);
- Compact Muon Solenoid (CMS);
- LHC-beauty (LHCb);
- A Large Ion Collider Experiment (ALICE).

In the next section I will give a brief description of the main experiments of LHC, focusing in particular on the ALICE experiment.

2.1.1 ATLAS

The ATLAS detector [50] is the world's largest general-purpose particle detector, measuring 46 metres long, 25 metres high and 25 metres wide; it weighs 7000 tons and consists of a series of ever-larger concentric cylinders around the interaction point (IP) where the proton beams from the LHC collide. This apparatus can be divided into four major parts: an inner detector, a set of calorimeters, situated outside the solenoidal magnet that surrounds the inner detector, a muon spectrometer and a magnet system. It covers the pseudorapidity range $|\eta| < 2.5$ for leptons and photons, and $|\eta| < 4.9$ for jets.

The main goal is the search for the Higgs boson and on 4 July 2012, ATLAS (together with CMS) reported evidence for the existence of a particle consistent with the Higgs boson at the level of five σ, with a mass of $126.0 \pm 0.4(stat) \pm 0.4(sys)$ GeV. This new "Higgs-like" particle was detected by its decay into two photons, and four leptons [51].

ATLAS has also a full heavy-ion program (see for instance [52]).

2.1.2 CMS

Together with ATLAS, CMS [53] is designed to discover the Higgs boson. The two experiments are designed to complement each other both to extend reach and to support the results. The search at CMS of Higgs boson is performed in five decay modes: $\gamma\gamma$, ZZ, W^+W , $\tau^+\tau^-$ and $b\bar{b}$, and an excess of events is observed at a mass $125.3 \pm 0.4(stat.) \pm 0.5(syst.)$ GeV [54].

CMS studies also the properties of the hot and dense matter produced in the Pb-Pb collisions, in particular it is studying the production rates of several quarkonium states (Υ(1S,2S,3S), J/Ψ, ψ(2S)) in Pb-Pb and pp collisions [55].

In the center of the CMS detector there are a high-magnetic-field and large-bore superconducting solenoid that encircles an all-silicon pixel and strip tracker, a lead-tungstate scintillating-crystals electromagnetic calorimeter, and a brass-scintillator sampling hadron calorimeter. The tracker and the calorimetry are fit inside the solenoid which generates a powerful magnetic field of 3.8 T. Outside the magnet are the large muon detectors. The detector is 25 m long, has a diameter of 15 m and covers the pseudorapidity range of $|\eta| < 2.5$.

2.1.3 LHCb

LHCb [56] studies the rare decays of beauty and charm hadrons and the CP violation in the interactions of b-hadrons. Such studies can help to explain the Matter-Antimatter asymmetry of the Universe. The detector is also able to perform measurements of production cross sections and electroweak physics in the forward region.

The detector is a single-arm forward spectrometer covering the pseudorapidity range $2 < \eta < 5$.

2.2 The ALICE detector

Nucleus-nucleus collisions have been proposed to create the QGP in the laboratory and the ALICE experiment has been designed to study the physics of strongly interacting matter in these collisions at the LHC.

Different detector systems form the ALICE experiment, each with its own specific technology choice and design constraints, driven both by the physics requirements and the experimental conditions present at LHC. The main aim is to resist the particle multiplicity in central Pb-Pb collisions and to provide high-momentum resolution as well as excellent particle identification over an ample momentum range, up to the highest LHC multiplicities (the charged particle multiplicity measured in $|\eta| < 0.5$ is $dN_{ch}/d\eta = 1601 \pm 60$ in 5% most central Pb-Pb collisions [57])

The ALICE experimental apparatus consists of:

- a central region which covers the pseudorapidity range $|\eta| < 0.9$, dedicated to the study of hadronic signals, dielectrons and photons;
- a forward muon spectrometer, to identify single muons or muon pairs in the range $2.5 < \eta < 4.0$;
- forward detectors ($|\eta| > 4.0$), to evaluate the photon and charged particle multiplicity and collision centrality.

In addition to the detectors used in Pb-Pb, pp and p-Pb collisions, there is an array of scintillators (ALICE COsmic Ray DEtector, ACORDE) installed on top of the L3 magnet to trigger on cosmic rays for ALICE calibration.

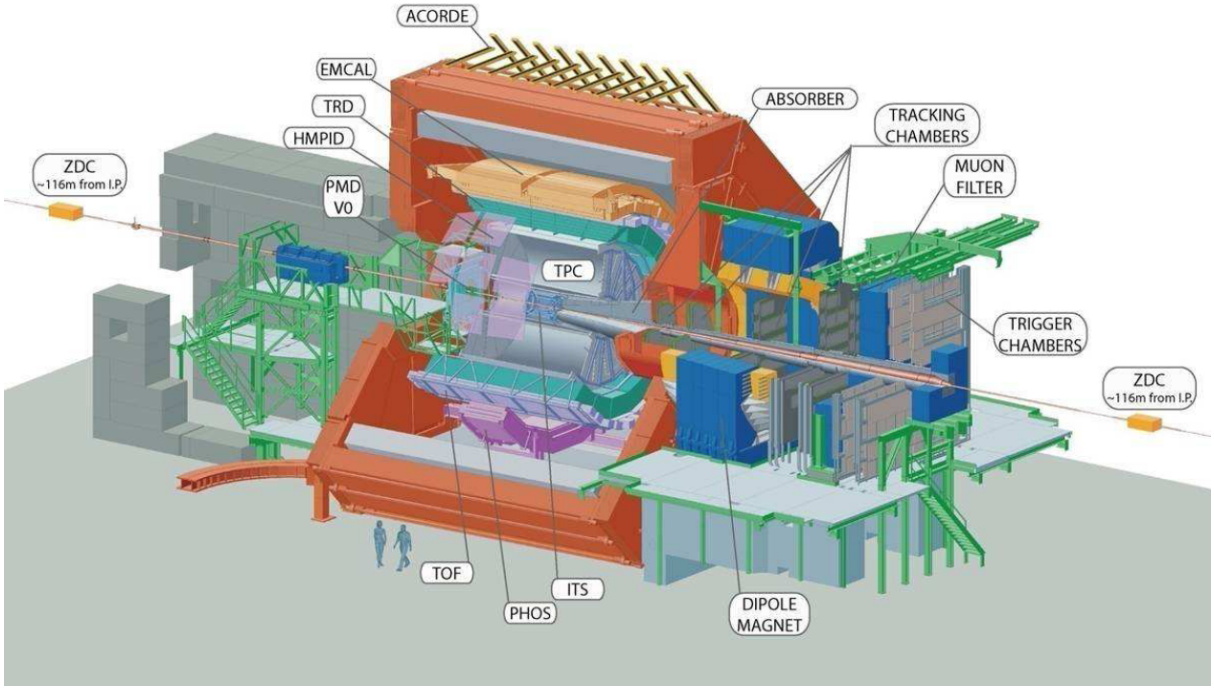

Figure 2.2: Layout of the ALICE detector.

2.2.1 Central detectors

The central detectors are housed in a solenoidal magnet previously used by the L3 experiment at LEP, which produces a 0.5 T field parallel to the beam axis. They are mainly dedicated to the vertex reconstruction, tracking, particle identification and momentum measurement.

In the following there is a description of the capabilities of each subdetector.

2.2.1.1 Inner Tracking System (ITS).

The ITS, shown in Figure 2.3, surrounds the beam pipe and is the ALICE detector situated closest to the interaction point.

It consists of six cylindrical layers of silicon detectors covering the central rapidity region ($|\eta| \leq 0.9$) located at radii between 3.9 cm and 43 cm.

The two innermost layers, for which a higher granularity is required, are the Silicon Pixel Detectors (SPD). Layers 3 and 4 consist of Silicon Drift Detectors (SDD), while

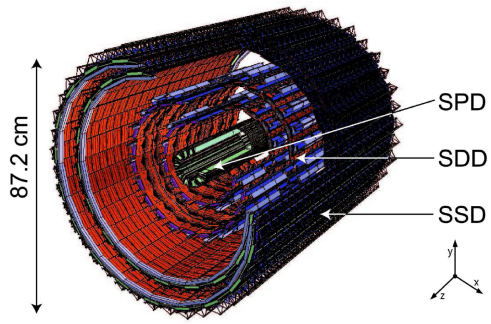

Figure 2.3: ITS detector.

Table 2.1: Main parameters of the ITS.

Parameter	SPD	SDD	SSD
radius r (cm)	3.9 and 7.6	15.0 and 23.9	38.0 and 43.0
length ± z (cm)	14.1 and 14.1	22.2 and 29.7	43.1 and 48.9
Number of channels	9.8 M	133k	2.6M
spatial precision rϕ (μm)	12	35	20
spatial precision z (μm)	100	25	830

the other layers (5 and 6) are the Silicon Strip Detectors (SSD).

The ITS performs primary and secondary vertex reconstruction, multiplicity measurements, tracking and identification via dE/dx measurements of low momentum particles (p below 200 MeV/c) to improve the momentum and angular resolution for tracks reconstructed by the TPC or which do not reach the TPC.

The main parameters of the ITS are summarized in Table 2.1.

2.2.1.2 Time Projection Chamber (TPC).

The TPC (shown in Fig. 2.4) is the main tracking detector of the central barrel and is optimised to provide, together with the other central barrel detectors, charged-particle momentum measurements from about $p_T \sim 0.1$ GeV/c up to $p_T \sim 100$ GeV/c, with good two-track separation, particle identification and vertex determination. The phase

Table 2.2: Main parameters of the TPC.

Parameter	Value
pseudo-rapidity coverage	$\|\eta\| < 0.9$
Azimuthal coverage	360°
active volume radial position	$84.8 < r < 246.6$ (cm)
active volume length	2×2.5 m
maximal drift time	90 μs

space covered by the TPC in pseudo-rapidity is $|\eta| < 0.9$. The TPC covers the full azimuth (with the exception of the dead zones).

It has cylindrical shape, 5 m long, with an inner and outer radius of ~ 85 cm and ~ 250 cm respectively. The readout planes are divided in 18 sectors in which multiwire proportional chambers are housed.

The TPC can identify particles with $p_T < 1$ GeV/c thanks to the good dE/dx resolution ($< 10\%$). The tracking efficiency is $> 90\%$ for $p_T > 100$ MeV/c, where the limiting factor are the interactions in the ITS material.

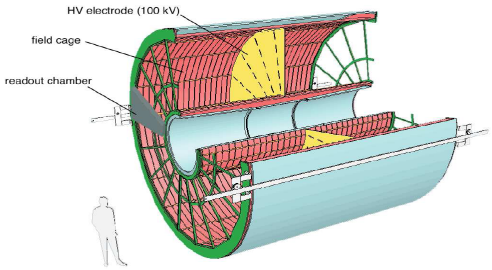

Figure 2.4: TPC detector.

The basic parameters of the TPC are summarized in Table 2.2.

2.2.1.3 Transition Radiation Detector (TRD).

The TRD provides electron identification for momenta greater than 1 GeV/c, where the pion rejection capability through energy loss measurement in the TPC is no longer sufficient.

Its use, in conjunction with TPC and ITS, allows to measure the production of light

Table 2.3: Main parameters of the TRD.

Parameter	Value
pseudo-rapidity coverage	$\|\eta\| < 0.84$
Azimuthal coverage	360°
active volume radial position	$290 < r < 368$ (cm)
mass resolution at the Υ mass	100 MeV/c^2
momentum resolution	3.5 % at 5 GeV/c

and heavy vector meson resonances and, thanks to the determination of the impact parameter, of open charm and beauty.

It is segmented along the azimuthal angle in 18 sectors. Each sector contains 30 modules arranged in 5 stacks along z and 6 layers in radius. Each detector element consists of a radiator of 4.8 cm thickness, a drift section of 30 mm thickness and a multiwire proportional chamber with pad readout. The TRD parameters are summarized Table 2.3.

2.2.1.4 Time Of Flight (TOF).

The main aim of the TOF detector is charged particle identification.

It performs π/K (π/p) separation for momenta above 0.5 GeV/c and up to 2.5 GeV/c, and protons up to 4 GeV/c in the central pseudorapidity region ($|\eta| \leq 0.9$), with full azimuthal coverage.

The time of flight is measured by means of Multigap Resistive Plate Chambers with an intrinsic time resolution of about 50 ps.

The TOF is made of 1638 MRPCs situated in 90 gas-tight modules distributed over 18 azimuthal sectors. Each MRPC is composed of 96 readout pads and and 152928 readout channels (2.5×3.5 cm^2 each) covering a total area of 141 m^2 .

2.2.1.5 High Momentum Particle Identification Detector (HMPID).

The HMPID, composed of seven modules of Ring Imaging Cherenkov detectors, is designed to extend the useful range in ALICE for the identification of p and K up to 3 GeV/c and of p up to 5 GeV/c.

It is designed as a single-arm array with a pseudo-rapidity acceptance of $|\eta| < 0.6$ and an azimuthal coverage of about 58°, corresponding to 5% of the central barrel phase space, and has a radial position of 5 m.

2.2.1.6 PHOton Spectrometer (PHOS).

The PHOS is a high-resolution electromagnetic spectrometer dedicated to test the thermal and dynamical properties of the initial phase of the collision, that can be extracted from low p_T direct photon measurements, and to the study of the jet quenching effect through the measurement of high-p_T π^0 and γ-jet correlations.

Due to the high multiplicity in nuclear collisions, the calorimeter has a high granularity and is located at a large distance from the interaction point (4600 mm), in order to keep the occupancy at a reasonable level, and covers the pseudorapidity region $|\eta| \leq 0.12$.

2.2.1.7 ElectroMagnetic Calorimeter (EMCal).

The last detector added to the ALICE design is a Pb-scintillator sampling calorimeter. It is located adjacent to the ALICE magnet coil at a radius of 4.5 m from the beam line. It covers the pseudorapidity range $|\eta| < 0.7$, and a 107° interval in azimuthal angle and is positioned approximately opposite in azimuth to the PHOS detector.

The EMCal provides a fast and efficient trigger (L0, L1 [1]) for hard jets, photons and electrons and combined with ALICE capabilities to track and identify particles from very low to high p_T, it makes possible a comprehensive study of jet interactions in the medium produced in heavy ion collisions at the LHC.

2.2.2 Muon Spectrometer.

Muon detection is performed in the pseudo-rapidity region $-4 < \eta < -2.5$ by the muon spectrometer, which is composed of three absorbers, a dipole magnet, five stations of tracking chambers and two stations of trigger chambers. These components are described in the following paragraphs (see Figure 2.5).

[1] There are two levels of the "fast" part of the ALICE trigger: a Level 0 (L0) signal which reaches detectors at 1.2 μs, but which is too fast to receive all the trigger inputs, and a Level 1 (L1) signal sent at 6.5 μs which picks up all remaining fast inputs.

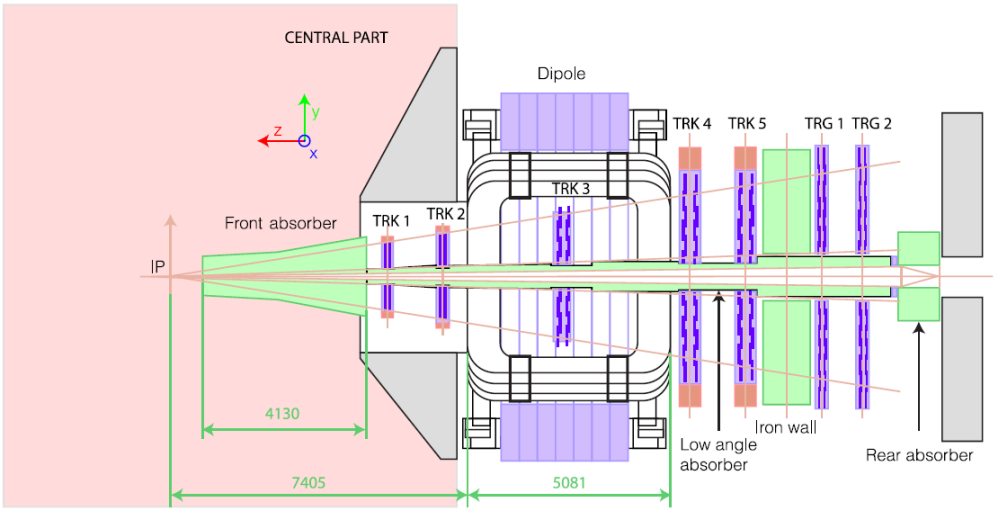

Figure 2.5: The ALICE muon spectrometer layout

2.2.2.1 Absorbers.

Three absorber sections are designed to shield the detectors from the large particle flux: a front absorber, a beam shield that surrounds the beam pipe and a muon filter (iron wall), just before the trigger chambers.

The **Front absorber** (Fig. 2.6) has to attenuate the hadronic flux by at least two orders of magnitude and decreases the background coming from π and K decays into muons by limiting their free path. It is located inside the L3 magnet, 0.9 m away from the interaction point. Its total extent of material corresponds to ten hadronic interaction lengths. The central part, near the interaction vertex, is made of carbon (a low Z material), to reduce muon multiple scattering effects, which leads to a worse mass resolution. The rear region is made of concrete, lead, tungsten and borated polyethylene to absorb the secondary particles produced in the absorber, low energy neutrons and protons. The external part is made of lead and tungsten to protect the detectors from the particle flux originated by particles crossing the absorber.

The **Muon Filter** is put between the last tracking Station and the first trigger plane. It is made of an iron layer 1.2 m thick, corresponding to 7.2 hadronic interaction lengths. It enhances the trigger chamber performance by stopping the hadrons not absorbed by the front absorber or produced in the beam pipe. Together with the

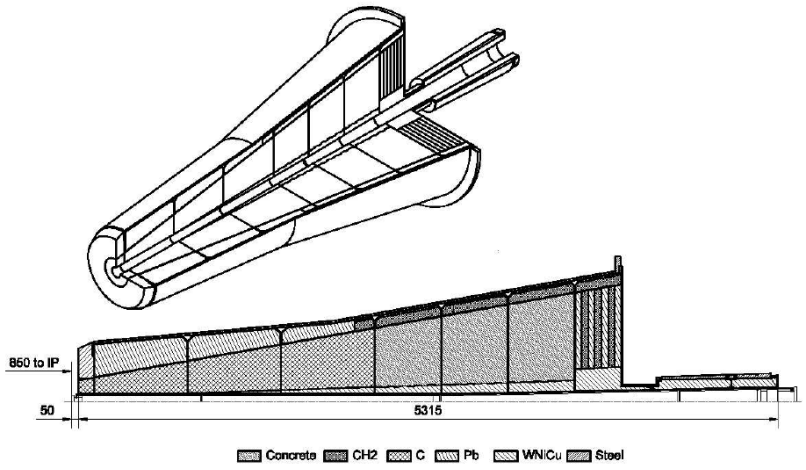

Figure 2.6: Layout of the front absorber.

front absorber it also stops muons with momentum lower than 4 GeV/c, to reduce the background due to pion and kaon decays.

The **Beam Shield** has to protect the muon spectrometer detectors from high rapidity particles and secondaries along the beam pipe. It is composed of tungsten and lead and is covered by a stainless steel layer.

2.2.2.2 Dipole Magnet.

The dipole magnet is 5 m long and provides a magnetic field of up to 0.7 T and a field integral along the beam axis $\int |B| dz \sim 3$ Tm. It is designed to provide a horizontal magnetic field perpendicular to the beam axis, whose polarity can be reverted within a short time and it is placed about 7 m away from the IP.

2.2.2.3 Tracking system

The muon tracking system is made of a set of five tracking stations. Each station is made of two chamber planes, with two cathode planes each, which are readout in order to provide bi-dimensional information.

The stations are located between 5.2 and 14.4 m from the IP, the first two upstream of the dipole magnet, the third in its gap and the last two downstream. The spatial

resolution of the tracking chambers is ~ 100 μm in the bending direction and 1 mm in the non-bending plane.

The tracking chambers are composed of multiwire proportional chambers, filled with an Ar/CO_2 (80/20) gas mixture. To limit the occupation rate to a maximum of 5% a very fine segmentation is needed and since the hit density decreases with the distance from the beam pipe, larger pads are used at larger radii and pads near the beam pipe in the first station are as small as 4.2×6 mm^2. The total number of read-out channels is about 1 million. The chambers in station 1 and 2 have a quadrant geometry (Figure 2.7(a,c) shows a layout of the cathode plane for one of the quadrants of Station 2), with read-out electronics on the surface, while those in stations 3 through 5 have a slat geometry and read-out electronics on the side (Figure 2.7(b,d)). In order

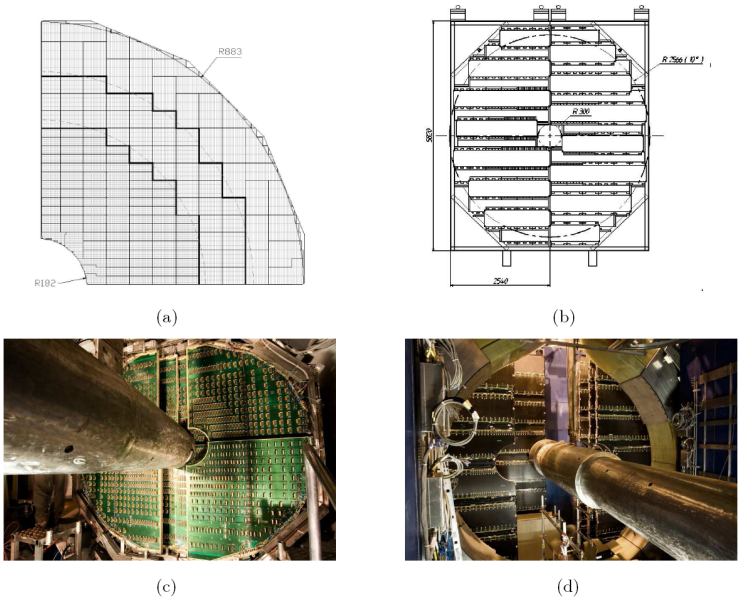

Figure 2.7: Tracking chambers: the cathode plane layout of Station 2 (a,c) and the scheme (b) of a station with slat architecture (d).

to minimise multiple scattering of the muons, the materials in the tracking system are composite materials such as carbon fibre, so that the total thickness of chambers is 0.03 X_0. Given the strict spatial resolution requirements, the position of the chambers is monitored optically by a Global Monitoring System within a 20 μm accuracy.

16 channel chips are the front-end electronics for all stations (Multiplexed ANAlogic

Signal, MANAS). Four of these chips are mounted on a front end MANAS Numerical card (MANU), equipped with a 12-bit ADC, read by the Muon Arm Read-out Chip (MARC) with zero suppression.

2.2.2.4 Trigger system.

The trigger has to select, between the background sources, the events of interest. It consists of two detector stations (MT1 and MT2), placed at 16.1 and 17.1 m from the IP, respectively, placed behind the iron muon filter. Each one is composed of two planes of resistive plate chambers (RPC), with a time resolution of about 2 ns. Each plane, segmented into strips, provides the x and y coordinates. The horizontal strips (aligned with the x axis in the ALICE reference system) measure the bending deviation due to the dipole magnetic field, while vertical strips (aligned with the y axis) measure the non-bending direction. The two layers of read-out pads are therefore called bending and non-bending plane respectively. The total system is composed of 234 detection areas, each of them associated with a local trigger board. The local board density reflects the strip segmentation. The strip dimensions are about 1, 2 and 4 cm in the bending plane, moving from the beam pipe outwards, and about 2 and 4 cm in the non-bending plane.

The signals are discriminated and sent to the redout electronics to be processed. The muon trigger is fired when at least three of the four RPC planes give a signal compatible to a tracklet in the muon trigger system. A dimuon trigger (single muon trigger) is generated when at least two tracks (at least one track), satisfy the predefined p_T cut, chosen as a compromise between efficiency and background rejection. The trigger information is also used to identify the tracks in the offline analysis, since muons are not absorbed by the iron wall, differently from the residual hadrons.

2.2.3 Forward detectors

A good resolution on the centrality measurement is important to characterize the heavy-ion collisions. In fact, QGP signatures show different characteristics as a function of the energy density, estimated through the measurement of collision centrality.

2.2.3.1 Zero Degree Calorimeter (ZDC).

The aim of the ZDC is the estimation of the heavy-ion collision geometry through the measurement of the energy carried in the forward direction (at zero degrees relative to the beam direction) by the non-interacting beam nucleons (the "spectators").

The ZDC system consists of four hadronic calorimeters, two for neutrons (ZN) and two for protons (ZP), placed at 116 m from the interaction point and it is completed by two electromagnetic calorimeters (ZEM), both placed at about 7 m from I.P., which allow to resolve ambiguities in the determination of the centrality. In fact, spectator nuclear fragments with Z/A$\sim$ 0.5, usually produced in peripheral collisions, are bent in the beam pipe, and do not reach the hadronic calorimeters, causing a low energy deposit for these collisions. These ones can be discriminated from central collisions giving the same amount of energy deposit by measuring the electromagnetic energy produced [58].

Each detector is made of quartz fibers inset in a dense material and oriented at 0° with respect to the beam axis. The Cherenkov light produced in the fibers is driven to photomultipliers.

The neutron detectors, due to the constraints imposed by their location in the reduced space between the beam pipes, have dimensions $7 \times 7 \times 100$ cm^3 and use very dense passive material (tungsten).

The proton devices, not subject to stringent geometrical constraints, have larger dimensions ($20.8 \times 12 \times 150$ cm^3) and are made of brass.

Differently from the ZN and ZP, the ZEM fibres are oriented at 45°, a choice that maximizes the detector response.

2.2.3.2 Photon Multiplicity Detector (PMD).

The PMD measures the multiplicity and spatial distribution of photons in order to provide estimates of the transverse electromagnetic energy and reaction plane.

It is installed at 350 cm from the interaction point, on the opposite side of the muon spectrometer and it covers the region $1.8 \leq \eta \leq 2.6$.

It consists of two planes of proportional gas counters with a $3X^0$ thick lead converter in between them.

2.2.3.3 Forward Multiplicity Detector (FMD).

The FMD is a silicon strip detector divided in seven disks perpendicular to the beam pipe and placed at distances between 42 and 225 cm from the IP. Its purpose is to measure $dN/d\eta$ in the pseudorapidity region outside the central acceptance ($1.7 < \eta < 3.4$ and $-5.1 < \eta < -1.7$). This detector is designed in order to measure charged particle multiplicities from tens (in pp runs) to thousands (in Pb-Pb runs) per unit of pseudorapidity.

2.2.3.4 T0 and V0.

The T0 detector, made of two arrays of Cerenkov counters, produces the T0 signal for the TOF with a precision of 50 ps, and measures the vertex position with a precision of ± 1.5 cm, thus providing a L01 trigger when the position is within the preset values. It also measures the particle multiplicity and generates a centrality trigger. The two arrays are placed asymmetrically with respect to the IP due to the constraint imposed by the muon spectrometer front absorber: one is placed at 72.7 cm with a pseudo-rapidity coverage of $3.28 < \eta < 2.97$ and the other one is at 375 cm, covering $4.61 < \eta < 4.92$.

The V0 detector consists of scintillators placed at -3.4 m and 0.9 m from the IP and covering the pseudo-rapidity regions $-5.1 < \eta < -2.8$ and $1.7 < \eta < 3.7$, respectively. It is used for trigger purposes and for beam-gas rejection.

2.2.4 ALICE trigger and data acquisition

When a bunch crossing in the LHC machine occurs, the Central Trigger Processor (CTP) decides within less than one microsecond if to collect the data resulting from a particular collision.

There are two levels of the "fast" part of the ALICE trigger: a Level 0 (L0) signal which reaches detectors at 1.2 μs, but which is too fast to receive all the trigger inputs, and a Level 1 (L1) signal sent at 6.5 μs which picks up all the remaining fast inputs. The L0 signals from the fastest detectors, such as the SPD, V0, T0 and the muon trigger system, are treated with a three states logic (asserted, not relevant, negated) and combined with logic AND and OR in order to select a certain class of events. On the other hand the information of slower detectors is used to create a Level 1.

The last level of trigger, the so called Level-2 (L2), arrives after 88 μs.

3

Monte Carlo simulation of the dimuon sources

Contents

In this chapter, the dimuon mass spectrum in pp collisions is described as a superposition of various sources and their simulation is performed with a parametric generator, named AliGenMUONLMR.

The dominant processes in the low mass region ($M < 1.5$ GeV/c^2) are the electromagnetic decays of the light pseudoscalar and vector mesons (η, η', ρ, ω and ϕ) and the semi-leptonic open charm and beauty decays. Open charm and beauty have been simulated with a parametrization of PYTHIA (AliGenCorrHF [59]).

3.1 Expected Contributions

Mesons are composed of a quark and an antiquark, bound together by the strong interaction. Two quarks can have their spins aligned, in which case the two spin vectors add to make a vector of length $J_S = 1$, called the spin triplet states. If two quarks have unaligned spins, the spin vectors add up to make a vector of length $J_S = 0$, called the spin singlet states. Since mesons are made of one quark and one antiquark, they can be found in triplet and singlet spin states. Quarks and antiquarks have opposite intrinsic

parities and as a consequence, mesons with no orbital angular momentum ($L = 0$) all have odd parity ($P = 1$). Thus, the $J_S = 0$ states have the quantum numbers $J^P = 0^-$ and are called pseudoscalar mesons, while the $J_S = 1$ states have $J^P = 1^-$ and are called vector mesons.

The lightest mesons contain the first three quark flavors (u,d,s) and we expect that pseudoscalar and vector meson families contain $3^2 = 9$ states. The pseudoscalars are divided into an iso-vector triplet, namely the three pions, $\pi^+ = u\overline{d}$, $\pi^0 = 1/\sqrt{2}(u\overline{u}-d\overline{d})$, $\pi^- = \overline{u}d$, two iso-doublets, the $K^+ = u\overline{s}$ and the $K^- = \overline{u}s$ with $\overline{K}^0 = \overline{d}s$ and the last two pseudoscalars mesons, η and η', whose actual states appear to be the following linear combinations:

$$\eta = \left(\frac{\cos\theta_P}{\sqrt{6}} - \frac{\sin\theta_P}{\sqrt{3}}\right) u\overline{u} + \left(\frac{\cos\theta_P}{\sqrt{6}} - \frac{\sin\theta_P}{\sqrt{3}}\right) d\overline{d} - \left(\frac{\cos\theta_P}{\sqrt{6}/2} + \frac{\sin\theta_P}{\sqrt{3}}\right) s\overline{s}$$

$$\eta' = \left(\frac{\sin\theta_P}{\sqrt{6}} + \frac{\cos\theta_P}{\sqrt{3}}\right) u\overline{u} + \left(\frac{\sin\theta_P}{\sqrt{6}} + \frac{\cos\theta_P}{\sqrt{3}}\right) d\overline{d} - \left(\frac{\sin\theta_P}{\sqrt{6}/2} - \frac{\cos\theta_P}{\sqrt{3}}\right) s\overline{s}$$

The pseudoscalar mixing angle, θ_P, is thought to be $\approx -10°$, with a large uncertainty: this is compatible with the mixing $\eta = 1/\sqrt{6}(u\overline{u}+d\overline{d}-2s\overline{s})$ and $\eta' = 1/\sqrt{3}(u\overline{u}+d\overline{d}+s\overline{s})$, which would decompose the pseudoscalar nonet into an $SU(3)$ octet and $SU(3)$ singlet.

For the vector meson states we have the quark structure analogous of the pseudoscalars, with the ρ^+, ρ^-, ρ^0 corresponding to the pions, the K^* mesons corresponding to the pseudoscalar K mesons, the ϕ and the ω corresponding to the η and η' respectively. The observed ϕ and ω states are again mixtures of the pure states $u\overline{u}$, $d\overline{d}$ and $s\overline{s}$, but the measured angle $\theta_V \approx 35°$ is much larger than θ_P and is compatible with the ideal mixing angle for which the ϕ becomes a pure $s\overline{s}$ state:

$$\omega = \frac{1}{\sqrt{2}}(u\overline{u} + d\overline{d}), \qquad \phi = s\overline{s}$$

By contrast to the pseudoscalar case, hence, neither the ω nor the ϕ are a $SU(3)$ singlet.

In the following it is shown a description of the dominant processes in the low mass region.

Table 3.1: The properties of the pseudoscalar which contribute significantly to the dimuon mass spectrum [60].

Particle	Mass [MeV/c^2]	Γ [MeV/c^2]	Quark Content
η	547.853 ± 0.024	$(1.30 \pm 0.07) \cdot 10^{-3}$	$\eta = 1/\sqrt{6}(u\overline{u} + d\overline{d} - 2s\overline{s})$
η'	957.78 ± 0.06	0.194 ± 0.009	$\eta' = 1/\sqrt{3}(u\overline{u} + d\overline{d} + s\overline{s})$

3.1.1 The Pseudoscalar Mesons, η and η'

The η and η' mesons have Dalitz and 2-body decays. The (single) Dalitz decay is a 2γ decay, in which one of the photons is virtual and converts into a lepton pair, $PS \to \gamma^*\gamma \to \mu^+\mu^-\gamma$. There is also a double Dalitz decay in which both γ are virtual photons and convert into a lepton pair, but with a much smaller branching ratio. The properties of the pseudoscalars which contribute significantly to the dimuon mass spectrum, either through a decay into two muons or via a Dalitz decay, are summarized in Table 3.1.

Branching ratios for the η are [60]:

$$BR(\eta \to \mu^+\mu^-) = (5.8 \pm 0.8) \times 10^{-6}$$

$$BR(\eta \to \mu^+\mu^-\gamma) = (3.1 \pm 0.4) \times 10^{-4}$$

For the η' we have [60]:

$$BR(\eta \to \mu^+\mu^-\gamma) = (1.09 \pm 0.27) \times 10^{-4}$$

The η' 2-body decay is strongly suppressed, since the branching ratio for a pseudoscalar decay into a lepton pair is proportional to $(m_l/m_P)^2$, where m_l and m_P are the lepton and pseudoscalar meson masses, respectively [61]. We can thus neglect its contribution to dimuon mass spectrum.

3.1.2 The Light Vector Mesons: ρ, ω and ϕ

The vector mesons that mainly contribute to the dimuon mass spectrum are ρ, ω and ϕ. Their properties are summarized in Table 3.2.

The vector mesons decay into two muons via a virtual photon, $V \to \gamma^* \to \mu^+\mu^-$. In addition, the ω has a Dalitz decay in which the lepton pair is accompanied by a π, $\omega \to \gamma^*\pi^0 \to \mu^+\mu^-\pi^0$.

Table 3.2: The properties of the Light Vector Mesons which contribute significantly to the dimuon mass spectrum [60].

Particle	Mass [MeV/c^2]	Γ [MeV/cc^2]	Quark Content
ρ	775.49 ± 0.034	149.1 ± 0.8	$\rho = \frac{1}{\sqrt{2}}(u\overline{u} - d\overline{d})$
ω	782.65 ± 0.12	8.49 ± 0.08	$\omega = \frac{1}{\sqrt{2}}(u\overline{u} + d\overline{d})$
ϕ	1019.455 ± 0.020	4.26 ± 0.04	$\phi = s\overline{s}$

The branching ratios are[60, 62]:

$$BR(\rho \to \mu^+\mu^-) = (4.55 \pm 0.28) \times 10^{-5}$$

$$BR(\omega \to \mu^+\mu^-) = (9.0 \pm 3.1) \times 10^{-5}$$

$$BR(\omega \to \mu^+\mu^-\pi^0) = (1.3 \pm 0.4) \times 10^{-4}$$

$$BR(\phi \to \mu^+\mu^-) = (2.87 \pm 0.19) \times 10^{-4}$$

For the ω-Dalitz decay, we used the most recent result, obtained by the NA60 collaboration. For the ω and ϕ 2-body decays, we have assumed the lepton universality, which states that the electro-weak interaction couples to all leptons with the same strength.

The dilepton decay width of a vector meson of mass m_V is described, within the vector meson dominance model (derived from the appropriate Feynman diagram and integrating over available phase space), by [63]:

$$\Gamma(V \to l^+l^-) = \frac{4\pi}{3}\left(\frac{\alpha}{g_V}\right)^2\left(1 + 2\frac{m_l^2}{m_V^2}\right)(m_V^2 - 4m_l^2)^{0.5}$$

where g_V is the vector meson coupling constant and the value for ϕ is -12.02 [63]. For the ϕ and ω, one has:

$$\frac{\Gamma(\phi \to e^+e^-)}{\Gamma(\phi \to \mu^+\mu^-)} = 0.999$$

$$\frac{\Gamma(\omega \to e^+e^-)}{\Gamma(\omega \to \mu^+\mu^-)} = 0.9979$$

The difference between the two decay channels is at the per mil level. Therefore, due to the much larger uncertainty in the $\mu\mu$ channel, we used the values measured in dielectrons: $BR(\omega \to e^+e^-) = (7.28 \pm 0.14) \times 10^{-5}$, $BR(\phi \to e^+e^-) = (2.954 \pm 0.030) \times 10^{-4}$.

3.1.3 Open Charm and Open Beauty

The main contribution to the dimuon mass spectrum in the mass region between the ϕ and the J/ψ is due to simultaneous semi-muonic decay of pairs of D mesons (open charm). Over 4 GeV/c^2 the open beauty contribution is the most important one in the continuum. These sources also give a non-negligible contribution in the mass region from the threshold to the ϕ.

D mesons are formed via the creation of a $c\bar{c}$ pair and the subsequent hadronization (fragmentation) of the charmed quarks, when each of them binds with a u, d or s quark (or antiquark). If both charmed hadrons then decay semi-muonically, they may contribute to the dimuon mass spectrum, if the two muons are accepted and reconstructed. Since the energy of the muons depends on the decay kinematics which is not fixed, the formed muon pair will have a continuum spectrum of invariant masses.

The B meson is the bottom analog to the D meson. The open beauty production, differently from the open charm, gives also a signal in the like-sign sample (positive or negative pairs of muons); these come from various beauty decay chains , such as:

$$B^+ \to \overline{D^0} l^+ \nu, \quad \text{with} \quad \overline{D^0} \to l^- X$$

$$B^- \to D^0 \pi^-, \quad \text{with} \quad D^0 \to l^+ X$$

Above, there are three correlated muons in the final state from which we obtain a like-sign dimuon, apart from the standard opposite-sign dimuons. Correlated like-sign muon pairs can be also obtained when the neutral B mesons (B_d^0 and B_s^0) first oscillate into their anti-particle and then decay muonically. The decay muons will have like-sign charge if one of them decayed from an oscillated mother.

3.2 Parametric Generator

As already described, the processes included in the hadronic decay cocktail have been simulated with AliGenMUONLMR. This generator is based on a parametric generation of the light resonances contributing to the low mass spectrum, where the kinematic distributions and multiplicities are extracted from the data, where available, or parameterized according to a simulation performed with PYTHIA 6.4 (Perugia-0 tune). This generator presents some advantages with respect to PYTHIA: it is faster (about 200

times faster than PYTHIA MB) and more flexible, allowing to set up parameters and to select only one process to generate, in order to calculate the acceptance fastly. There is no correlation among the mothers, which are generated independently. Muons coming from pions and kaons produced in jets are not simulated as well: this processes should be present in the low mass region, but simulations made with PYTHIA have shown that they are negligible.

The simulated processes are:

$$\eta \to \mu^+\mu^-$$

$$\eta \to \mu^+\mu^-\gamma$$

$$\rho \to \mu^+\mu^-$$

$$\omega \to \mu^+\mu^-$$

$$\omega \to \mu^+\mu^-\pi^0$$

$$\eta' \to \mu^+\mu^-\gamma$$

$$\phi \to \mu^+\mu^-$$

In the following we are going to describe the parameterizations.

3.2.1 Transverse Momentum

The p_T distributions for the light mesons have been generated according to a power-law used also by the HERA-B experiment to fit the ϕ p_T spectrum [64]:

$$\frac{dN}{dp_T} \propto \frac{p_T}{\left[1 + \left(\frac{p_T}{A}\right)^2\right]^n} \tag{3.1}$$

The parameters for the p_T distributions are summarized in the Table 3.3. For the ρ, ω and ϕ distributions at 7 TeV we have used an iterative tuning based on the ALICE data in the $\mu^+\mu^-$ channel obtained in the analysis described in the next chapter. At 2.76 TeV we tried two different parameterizations: the first one uses the p_T distributions measured at 7 TeV; for the second one we scaled the average p_T value at 7 TeV based on Pythia, according to the formula:

$$\langle p_T \rangle^{ALICE}_{2.76\ TeV} = \langle p_T \rangle^{ALICE}_{7\ TeV} \cdot \frac{\langle p_T \rangle^{PYTHIA}_{2.76\ TeV}}{\langle p_T \rangle^{PYTHIA}_{7\ TeV}} \tag{3.2}$$

Table 3.3: Input parameters for the generation of the p_T distribution, relative to the power-law 3.1.

Particle	A (GeV/c) at 7 TeV	n at 7 TeV	A (GeV/c) at 2.76 TeV	n at 2.76 TeV
η	0.641	2.62	0.641	2.62
ρ and ω	1.44	3.16	1.3551	3.16
ϕ	1.16	2.74	1.0811	2.74
η'	0.72	2.5	0.72	2.5

The values found for the ϕ are: $\langle p_T \rangle^{PYTHIA}_{2.76\ TeV} = 0.6790$ GeV/c and $\langle p_T \rangle^{PYTHIA}_{7\ TeV} = 0.7283$ GeV/c obtained with PYTHIA-Perugia-0 that gives a scale factor of 0.9323; $\langle p_T \rangle^{ALICE}_{7\ TeV} = 1.0174$ GeV/c obtained from the low mass region analysis at 7 TeV and $\langle p_T \rangle^{ALICE}_{2.76\ TeV} = 0.9455$ GeV/c is the final value. The two p_T distributions for $\rho+\omega$ and ϕ at 2.76 TeV (using the second method) and at 7 TeV obtained with AliGenMUONLMR are shown in figure 3.1.

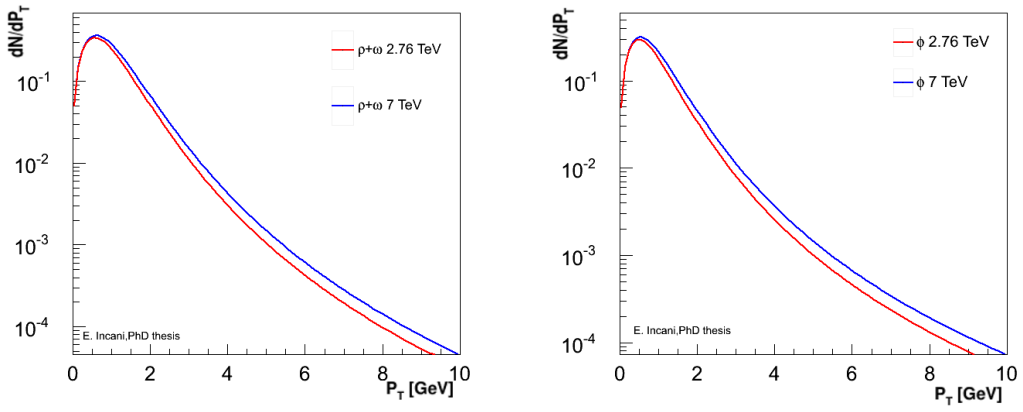

Figure 3.1: The p_T distributions at 7 TeV and 2.76 TeV for the $\rho+\omega$ (left) and ϕ (right) obtained with AliGenMUONLMR.

The default choice is the parameterization obtained scaling the 7 TeV distribution (eq.3.2).

The η' distribution is based on a parametrization of PYTHIA and the η distribution is based on preliminary results from η production yields measured in the two-photon decay channel by ALICE [65].

Table 3.4: Input parameters for the generation of the y distribution (3.3).

Particle	y_0 at 7 TeV	σ_y at 7 TeV	y_0 at 2.76 TeV	σ_y at 2.76 TeV
η	1.169	3.282	0.011	3.474
ρ	1.234	3.264	-0.01	3.409
ω	1.311	3.223	-0.037	3.294
ϕ	2.388	2.129	-0.016	2.717
η'	1.13	3.3	-0.010	3.312

3.2.2 Rapidity

The input rapidity distributions for all particles are based on a parametrization of PYTHIA 6.4.

For the rapidity distribution, it is assumed that the function is constant around mid-rapidity, and falls as a gaussian starting from a certain value y_0 (Fig: 3.2):

$$\frac{dN}{dy} = \begin{cases} \text{const.} & \text{for } |y| < y_0 \\ e^{-\frac{1}{2}\frac{(|y|-y_0)^2}{\sigma_y^2}} & \text{for } |y| > y_0 \end{cases} \tag{3.3}$$

The parameters for the y distributions are summarized in the Table 3.4.

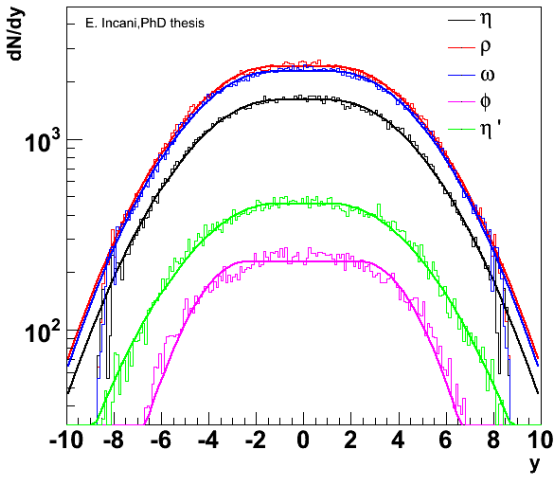

Figure 3.2: The y distributions at 7 TeV for the light mesons obtained with PYTHIA-Perugia-0.

Table 3.5: Input parameters for the generation of the multiplicity distribution.

Particle	a at 7 TeV	a at 2.76 TeV
η	-0.2647	-0.351
ρ	-0.1786	-0.2471
ω	-0.1896	-0.2583
ϕ	-1.167	-1.393
η'	-0.714	-0.9005

3.2.3 Multiplicity

Also the input multiplicity distributions are based on a parametrization of PYTHIA 6.4. The multiplicity distribution follows roughly an exponential trend. In figure 3.3 we can see the multiplicity distributions for the light mesons at 7 TeV, while in Table 3.5 the parameters used for the multiplicity distributions are summarized.

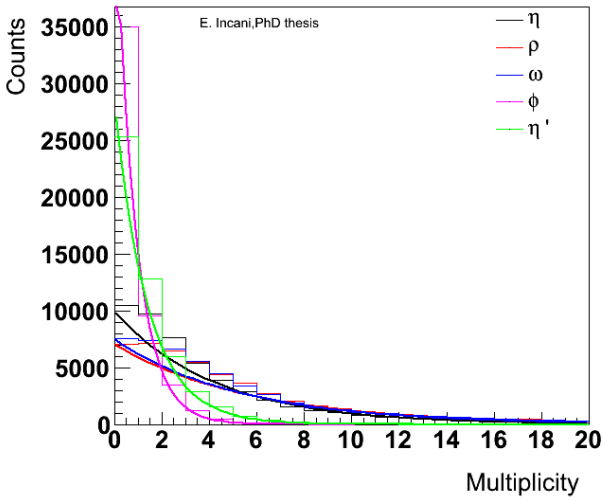

Figure 3.3: The multiplicity distributions at 7 TeV for the light mesons obtained with PYTHIA-Perugia-0.

3.2.4 Polar Angle

θ polar angle of muons is generated flat in the Collins-Soper frame (the polar angle is defined as the angle between the direction of the positive muon and the z beam axis,

in the center of mass frame of the two colliding particles).

3.2.5 Resonance Mass Line Shapes

The mass line shapes of the narrow resonances η, ω and ϕ, have been generated like a Dirac δ because the decay widths are narrower than the mass resolution of the apparatus, about 60 MeV ($\Gamma_\eta = 1.30 \pm 0.07$ keV, $\Gamma_\omega = 8.49 \pm 0.08$ MeV and $\Gamma_\phi = 4.26 \pm 0.04$ MeV). The ρ, on the other hand, is a wide resonance($\Gamma_\rho = 149.1 \pm 0.8$ MeV) because it predominantly decays in the two pions channel ($BR(\rho \to \pi^+\pi^-) \approx 100\%$) and the particles decaying via the strong interaction are characterized by lifetimes of the order of $\tau \sim 10^{-22} - 10^{-24}$ s, resulting in decay widths ($\Gamma \equiv 1/\tau$) of around 100 MeV. Due to its broadness, the shape of the ρ is highly influenced by phase space effects and by the production mechanism. The ρ line shape is described by the following expression:

$$\frac{dN}{dM} = \frac{\alpha^2 m_\rho^4}{3(2\pi)^4} \frac{\left(1 - \frac{4m_\pi^2}{M^2}\right)^{3/2} \left(1 - \frac{4m_\mu^2}{M^2}\right)^{1/2} \left(1 + \frac{2m_\mu^2}{M^2}\right)}{\left(M^2 - m_\rho^2\right)^2 + M^2\Gamma(M)^2} \left(2\pi MT\right)^{3/2} e^{-\frac{M}{T}} \tag{3.4}$$

T, 170 MeV[66], is a "temperature" parameter related to hadronisation. Figure 3.4 shows the ρ line shape obtained with AliGenMUONLMR.

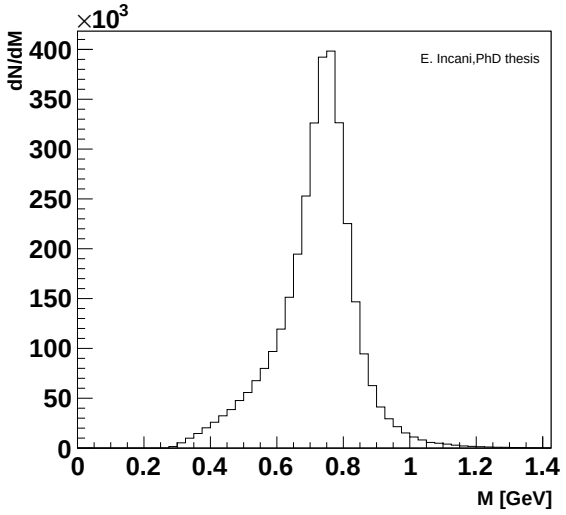

Figure 3.4: ρ line shape obtained with AliGenMUONLMR.

3.2.6 Form Factor for the Dalitz decays

The lepton pair mass distribution in Dalitz decays involving a photon was derived by N. Kroll and W. Wada [67], for the $\eta \to \mu^+\mu^-\gamma$ and $\eta' \to \mu^+\mu^-\gamma$ the distributions have the following shape:

$$\frac{dN}{dM} = \frac{1}{M}\left(1 + 2\frac{m_\mu^2}{M^2}\right)\left(1 - \frac{M^2}{m_{res}^2}\right)^3 \sqrt{1 - \frac{4m_\mu^2}{M^2}} \tag{3.5}$$

where M is the dimuon invariant mass and m_{res} is the resonance mass. The expression for the ω Dalitz conversion decay is different because the third particle π^0 is not massless:

$$\frac{dN}{dM} = \frac{1}{M}\left(1 + 2\frac{m_\mu^2}{M^2}\right)\left[\left(1 + \frac{M^2}{m_\omega^2 - m_{\pi^0}^2}\right)^2 - \frac{4m_\omega^2 M^2}{(m_\omega^2 - m_{\pi^0}^2)}\right]^{\frac{3}{2}} \sqrt{1 - \frac{4m_\mu^2}{M^2}} \tag{3.6}$$

To describe the dimuon mass spectra in the Dalitz decays we have to multiply the formulae 3.5 and 3.6 for the electromagnetic transition form factor, $|F(q^2)|^2$. The form factors for the η, η' and ω Dalitz decays are calculated in the environment of the vector meson dominance model.

3.2.6.1 Vector meson Dominance Model

The Vector meson Dominance Model (VDM) is a phenomenological model which describes the interactions between hadrons and photons mediated by vector mesons. In this model, in fact, a virtual photon can interact with a hadron only after a transition into a virtual vector meson state. This is possible since vector mesons (like ρ, ω and ϕ) have the same quantum numbers as the photon, $J^P = 1^-$. This mechanism works especially well when the transferred momentum squared, q^2, approaches the squared mass of an observed vector meson.

3.2.6.2 Electromagnetic transition form-factor

The probability of formation of a lepton pair with an invariant mass M in a conversion decay $A \to Bl^+l^-$ is proportional to the probability of emitting a virtual γ quantum with $q^2 = M^2$. The probability of emission of this photon is strongly influenced by the dynamic electromagnetic structure arising at the vertex of the transition $A \to B\gamma^*$. This structure is due to the creation of virtual states and is described by a transition

form factor, which modifies the dilepton effective mass spectrum. The transition form factor has been parameterized with the pole approximation [61]:

$$F(q^2) \equiv F(M^2) = \left[1 - \frac{M^2}{\Lambda^2}\right]^{-1} \tag{3.7}$$

Figure 3.5 reports the Λ values obtained by the NA60 experiment in proton-nucleus collisions at 400 GeV/c [62]. These values were used for the generation of the η and ω Dalitz mass line shapes. The η' form factor is parametrized with a Breit-Wigner

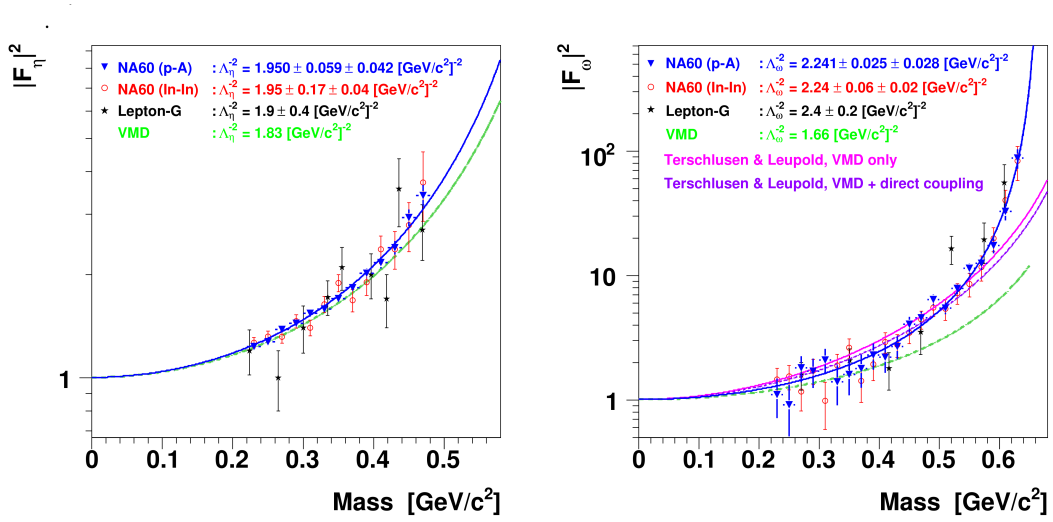

Figure 3.5: Electromagnetic transition form factors for the η (left) and ω (right) mesons as a function of M.

function fitted to data of Lepton-G [61].

3.3 Acceptance and Efficiency correction

The acceptance times efficiency ($A \times \epsilon$) of the detector has been evaluated through a Monte Carlo simulation using the parametric generator AliGenMUONLMR described above and the software framework of the ALICE Collaboration, AliRoot, which contains an interface to the GEANT3 [68] transport code and all the informations on the geometry of the detector. AliRoot uses the Offline Conditions Data Base (OCDB), which contains informations on the performances of each detector during each run, in order to simulate a realistic response of the different detectors. In figure 3.6 $A \times \epsilon$ is shown as a function of p_T for all processes at 7 TeV (on the left) and 2.76 TeV (on

the right): we can see that for $p_T < 1$ GeV/c ϕ has a bigger acceptance than the other processes and in general the acceptances increase with p_T and above 1 GeV/c rise smoothly.

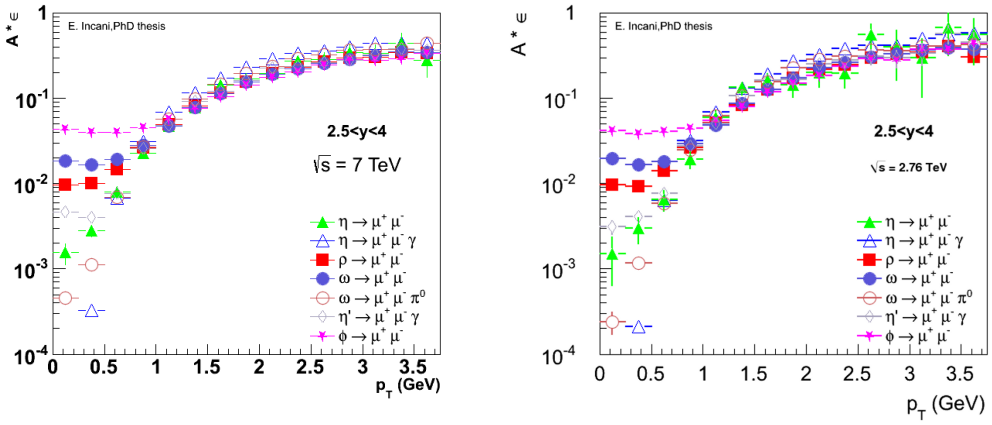

Figure 3.6: $A \times \epsilon$ as a function of p_T for all processes at 7 TeV and 2.76 TeV in the rapidity range $2.5 < y < 4$.

4

Low mass vector meson analysis via dimuon channel in pp collision at $\sqrt{s} = 7$ TeV

Contents

In this chapter I present the data sample, collected during the 2010 pp run at $\sqrt{s} = 7$ TeV from ALICE muon arm, used to analyze the low mass region ($m < 1.4$ GeV/c^2) via the dimuon channel. The ALICE experiment can measure the dimuon production in the rapidity range $-4.0 < y < -2.5$ [1]. We have measured the invariant mass spectrum for opposite-sign muon pairs (OS) for $p_T > 1$ GeV/c and we have described it, after combinatorial background subtraction, as a superposition of the light meson decays in muon pairs, with the additional contribution coming from correlated semileptonic decays of charm and beauty mesons. The ratio $N_\phi/N_{\rho+\omega}$ vs p_T, the ratio $\sigma_\rho/\sigma_\omega$ and the ϕ and ω p_T-differential cross sections are measured. This analysis is already published in [69]. An additional measurement of the differential cross sections as a function of rapidity, not previously studied, is treated at the end of this chapter.

[1] Data have been collected in the rapidity range $-4 < y < -2.5$ but the physics results will be given in the rapidity range $2.5 < y < 4$

4.1 Data sample

The results shown in this chapter were obtained by analyzing data collected during six months of data taking, from the end of April 2010 to the beginning of October of the same year. These data were divided into five sub-periods, each one homogeneous in average luminosity and pile-up rates, and characterized by reasonably stable tracking and trigger detector configuration and performance (the run list is reported in the Appendix 6.3.2).

During these six months the instantaneous luminosity given by the LHC to ALICE ranged from 0.6×10^{29} to 1.2×10^{30} cm^{-2}s^{-1}.

In this analysis we have used data collected with a single-muon trigger, which is activated when at least three of the four RPC planes in the two muon trigger stations give a signal compatible with a track in the muon trigger system.

To evaluate the integrated luminosity we have to use another sample, collected in parallel with a minimum bias (MB) trigger, independent of the muon trigger. It is activated when at least one out of the 1200 SPD readout chips detects a hit or when at least one of the two VZERO scintillator arrays is fired, in coincidence with the arrival of bunches from both sides.

The integrated luminosity was determined by measuring the MB cross section σ_{MB} and the number of MB events using this formula:

$$L_{int} = \frac{N_{MB}}{\sigma_{MB}} \frac{N_{\mu}^{\mu-MB}}{N_{\mu}^{MB}}. \tag{4.1}$$

N_{MB} is the number of minimum bias collisions, σ_{MB} is the measured cross section for such events, $\frac{N_{\mu}^{MB}}{N_{\mu}^{\mu-MB}}$ is the ratio between the number of single muons collected with the minimum bias trigger and with the muon trigger in the region $-4 < y_{\mu} < -2.5$, $p_T > 1$ GeV/c.

The number of minimum bias collisions was corrected, as a function of time, by the probability to have multiple interactions in a single bunch crossing. The σ_{MB} value at 7 TeV is 62.3 mb, and is affected by a 4% systematic uncertainty [70]. It was obtained measuring the cross section σ_{V0AND}, for the occurrence of coincident signals in the two VZERO detectors (V0AND) in a van der Meer scan [71]. The factor $\sigma_{V0AND}/\sigma_{MB}$ was obtained as the fraction of MB events where the L0 trigger input corresponding to the V0AND condition is fired. Its value is 0.87 and is stable within 0.5% over the analyzed

data. For some of the runs the information on the number of minimum bias trigger was missing, so these runs could not be used to calculate the integrated luminosity. The remaining sub-sample corresponds to L_{int}=55.7nb^{-1}, while a rough estimation based on the number of muon triggers taken in this sub-sample and in the full data set gives a total integrated luminosity of about 85 nb^{-1}.

4.2 Data selection and analysis

4.2.1 Track reconstruction

A Kalman filter algorithm [72, 73] has been used to reconstruct the muon track: the method starts from the most downstream tracking stations (4 and 5), since these are less affected by the background coming from soft particles that emerge from the front absorber, and straight line segments are formed from the clusters on the two planes of each station. A first estimate of the track properties is done assuming that tracks originate from the IP (Interaction Point) and are bent in a uniform magnetic field in the dipole. Subsequently, track candidates starting in station 4 are extrapolated to station 5, or vice versa, and match with at least one cluster on the basis of a χ^2 cut. At this point, parameters are recalculated using the Kalman filter. The same procedure is applied to the upstream stations, rejecting track candidates that cannot be matched to a cluster in the acceptance of the spectrometer. At last, fake tracks that share the same cluster with other tracks are removed and a correction for energy loss and multiple Coulomb scattering in the absorber is applied, by using the Branson correction [72]. The relative momentum resolution of the reconstructed tracks is 1% at 13 GeV/c, corresponding to the average momentum of muons coming from the ϕ decay.

4.2.2 Data selection

It is possible to select the muons requiring that the direction and position of each muon track reconstructed in the tracking chambers match the corresponding ones in the trigger stations (*trigger matching*): in this way it is possible to reject the hadrons produced in the absorber, which are stopped by the iron wall, or the muons that had a too low momentum to pass the absorber, or that had not high enough transverse momentum for the trigger.

In Fig. 4.1 the transverse momentum distributions for positive and negative muons, with and without trigger matching, are shown. We can observe a relative loss of low transverse momentum matched muons with respect to the non-matched, due to the trigger selection, which has a threshold at about 0.5 GeV/c. To understand better the trigger threshold, we have to note that the effect of such a cut is not sharp, as we can see in Fig. 5.8, where the ratio between the p_T distributions of Monte-Carlo muons that match the trigger and the ones of all muons is shown. The ratio increases from ~ 0 at low p_T to $\sim 50\%$ at $p_T = 0.5$ GeV/c, and reaches a plateau above 1 GeV/c [1].

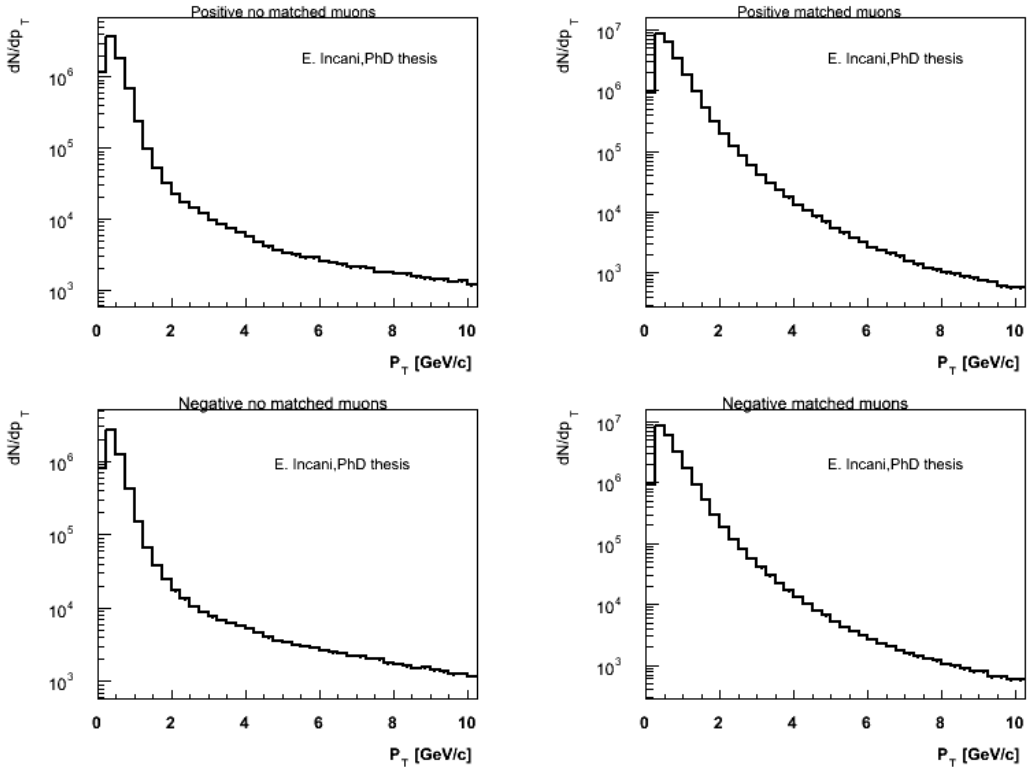

Figure 4.1: Top: transverse momentum distributions of positive muons without (left) and with trigger matching (right). Bottom: same for negative muons.

A plot useful to understand that the matching requirement is important to select the muons coming from the signal is the p_T of single muons as a function of DCA (Distance of Closest Approach). The DCA corresponds to the distance between the interaction

[1] We have used the MC muons instead of the real ones to be sure that the sub-sample used is composed only by muons and avoid pollution by hadrons

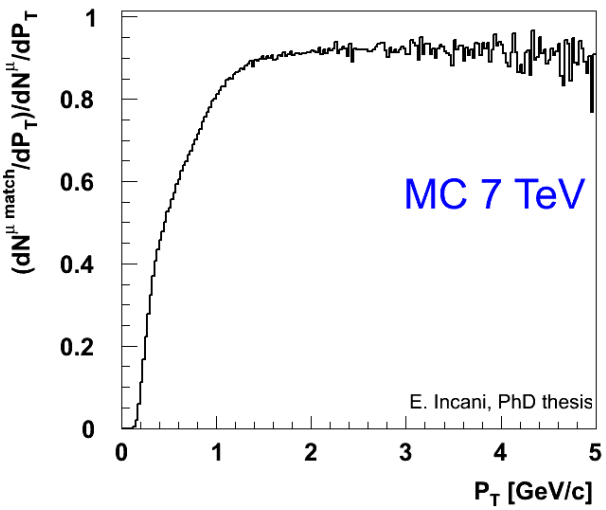

Figure 4.2: Ratio between the p_T distributions of MC muons that match the trigger and all muons.

vertex, in the plane perpendicular to the beam direction, and the extrapolated muon track. In fact the DCA of the muons coming from the interaction vertex is expected to be proportional to $1/p$. This is due to the multiple scattering in the front absorber and the tracks coming from the background do not follow this trend. This plot is shown in Fig. 4.3: on the top we have the momentum as a function of DCA for the MC muons coming from OS dimuons and the correlation between p and DCA is visible both with and without trigger matching requirement; on the bottom on the left, we have p as a function of DCA for the muons without trigger matching and on the right, the same plot is shown only for the matched muons coming from the OS dimuons. In the second one we can see that the muons with high DCA and high momentum have been cut.

The trigger matching rejects $\sim 85\%$ of muons pairs, as can be seen in Fig. 4.4. In the same figure, we can note that the only sample where the resonance peaks are clearly visible is the one where both muons match the trigger. Therefore, we decided to restrict our analysis to this sample.

In addition, we have applied a cut on the muon rapidity $-4 < y_\mu < -2.5$ [1], in order to remove the tracks close to the acceptance borders. Muon pairs, obtained combining the muons in each event, were selected requiring that both muons satisfy these cuts.

[1] In the relativistic limit the pseudorapidity η is equivalent to the rapidity y.

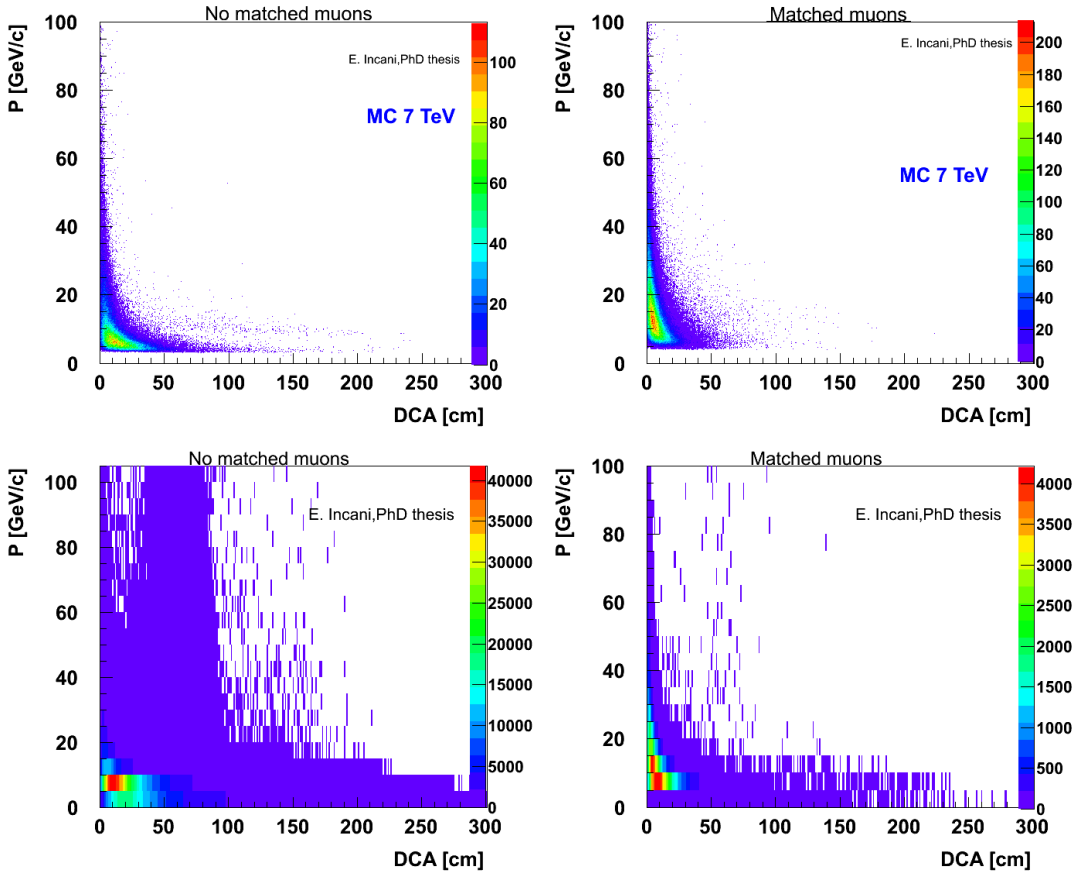

Figure 4.3: Single muon momentum as a function of DCA (Distance of Closest Approach): on the top: MC muons coming from OS dimuons; on the bottom: same for real muons without (on the left) and with trigger matching requirement (on the right).

An additional cut on the dimuon rapidity ($-4 < y_{\mu\mu} < -2.5$) was applied. Statistics analyzed in this work is summarized in table 4.1.

4.2.3 The Combinatorial Background and background subtraction

The OS are composed of correlated and uncorrelated pairs. The first mentioned constitute the signal, while the latter, coming from decays of hadrons into muons (especially pions and kaons), form the *combinatorial background*.

To extract the signal, a good description and subtraction of combinatorial background is important. The probability to have a pion/kaon that decays before being stopped by the hadron absorber is independent of the probability that another

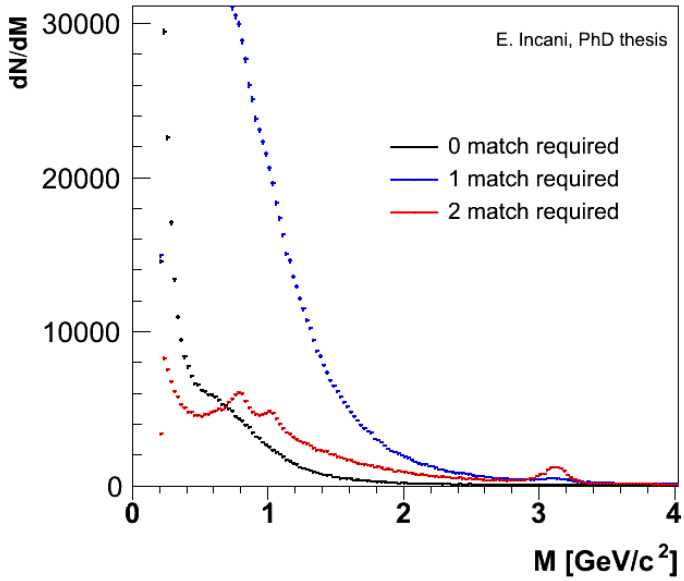

Figure 4.4: Mass distribution of OS pairs: in red both muons match the trigger; in blue only a muon matches the trigger; in black both muons do not match the trigger.

Table 4.1: Analyzed statistics at $\sqrt{s} = 7$ TeV.

Single muons	$5.40 \cdot 10^7$
Single matched muons	$4.19 \cdot 10^7$
Opposite-sign (OS) matched muon pairs	291,000
Matched negative muon pairs (like-sign LS^{--})	106,000
Matched positive muon pairs (like-sign LS^{++})	91,000

pion/kaon will also decay. Consequently, from the numbers of like-sign muon pairs, LS^{++} and LS^{--} (assumed to be uncorrelated), it is possible to determine the number of uncorrelated OS muon pairs, using the relation:

$$OS = 2\sqrt{LS^{++}LS^{--}} \tag{4.2}$$

This formula is correct if the acceptance of the LS and OS pairs have the same acceptance, otherwise the full formula should be used:

$$2R\sqrt{LS^{++}LS^{--}} \tag{4.3}$$

where the R factor is defined as:

$$R = \frac{A^{+-}}{\sqrt{A^{++}A^{--}}} \tag{4.4}$$

where A_{+-}, A_{++} and A_{--} are respectively the acceptances for OS, LS^{++} and LS^{--}.

The background is evaluated with two methods:

- evaluation using the event mixing technique.
- evaluation of the combinatorial background using the like-sign dimuons spectra.

4.2.3.1 Event mixing technique

In the event mixing two muons, coming from two different events, are coupled to build the invariant mass spectrum. This spectrum is normalized using the formula 4.3, and because the events are independent, the pairs are uncorrelated.

To be sure that the muons chosen for the event mixing are uncorrelated among other muons, we have chosen only muons coming from events that contain a single track in the muon spectrometer. To reproduce the uncorrelated pairs spectra we have chosen similar events: we have mixed events coming from the same sub-periods of data taking, such that these events are taken with the same experimental conditions. In principle, one should mix events with similar z-vertex positions, to make sure that the accepance seen by the muons is the same. We performed the event mixing grouping the events in z bins (2 cm wide between -20 and 20 cm) and mixing only the muons coming from events in the same bin.

We have done the event mixing also without any binning in z and calculated the ratio between the two, to look for possible differences. Fig. 4.5 shows that this ratio is flat. Because the differences between the two methods are negligible we decided not to apply the z binning in the mixing in order to recover part of the statistics for the LHC10f period, where the z-vertex information was missing.

The event mixing was normalized using the like-sign pairs, according to the formula 4.3, where the LS values are integrated in the whole mass spectrum. The R factor (Eq: 4.4) has been calculated using the event-mixed pairs to obtain $R = \frac{OS_{mixed}}{2\sqrt{LS^{++}_{mixed}LS^{--}_{mixed}}}$, where $LS^{\pm\pm}_{mixed}$ is the number of mixed pairs for a given sign combination. In Fig. 4.6 the R factor is plotted as a function of mass in different p_T bins.

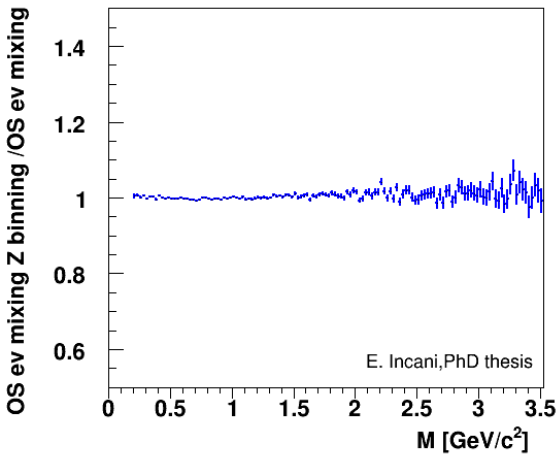

Figure 4.5: Ratio between the OS mixed pairs with and without z binning.

This factor changes its trend in different p_T ranges: for the lowest p_T bin it varies from ~ 0.7 at the mass threshold to ~ 1.2 around m_ϕ, it is about 1 at higher masses, and becomes flat and about 1, therefore less important, at higher p_T.

In order to verify the event mixing results, we compared the like-sign mass spectra obtained from the data and from the event mixing. Because both spectra are composed of uncorrelated pairs, we expect the same trend. In Fig. 4.7 we can see the ratio between the like-sign real and mixed spectra as a function of the mass for $0 < p_T < 1$ GeV/c and for $p_T > 1$ GeV/c. In the first plot we can see that the ratio is not flat, therefore the event mixing does not describe properly the combinatorial background at low p_T. In the second one the ratio is flat, differing from the unity by about 5% (we take this value as an estimate of the systematic error in the normalization).

4.2.3.2 LS method and comparison with the event mixing technique

The combinatorial background contribution to the opposite-sign mass spectrum for a given ΔM mass bin is evaluated from the like-sign mass spectra using the following formula:

$$OS^{bkg}(\Delta M) = 2R(\Delta M)\sqrt{LS^{++}(\Delta M)LS^{--}(\Delta M)} \tag{4.5}$$

where the R factor is defined based on the formula 4.4 evaluated for every mass bin.

The two methods for the calculation of the combinatorial background were compared for several p_T bins. For $p_T < 1$ GeV/c the two methods are in disagreement,

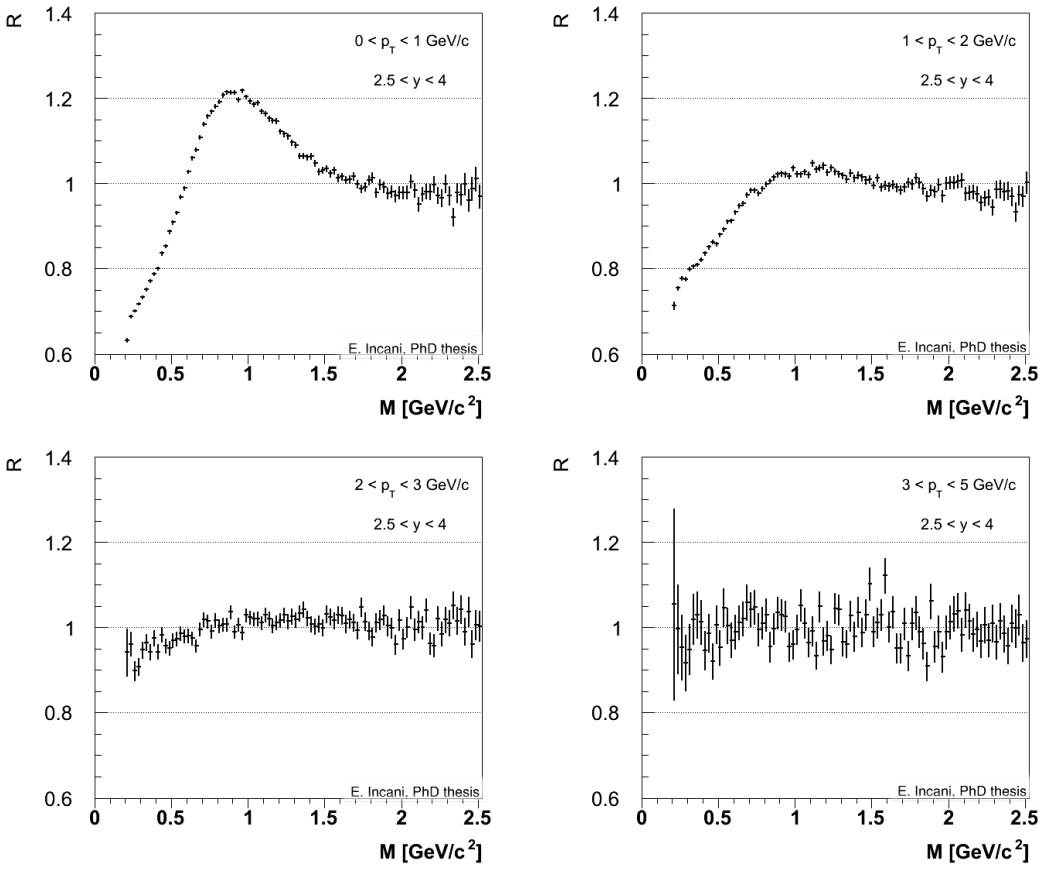

Figure 4.6: R factor versus mass for different p_T bins evaluated using the event mixed pairs.

see (Fig 4.8): in the case of the like-sign pairs method the estimated background overshoots the opposite-sign spectrum; as we have seen above, in the same p_T region, the ratio between the like-sign real and mixed spectra is not flat. We conclude that for $p_T < 1$ GeV/c the combinatorial background is not under sufficient control, and limit our analysis to $p_T > 1$ GeV/c.

The comparison between the two methods at higher p_T is shown in Fig. 4.9. We see that we have a good agreement between the two techniques. We choose to use the event mixing estimation of the background which has smaller statistical fluctuations.

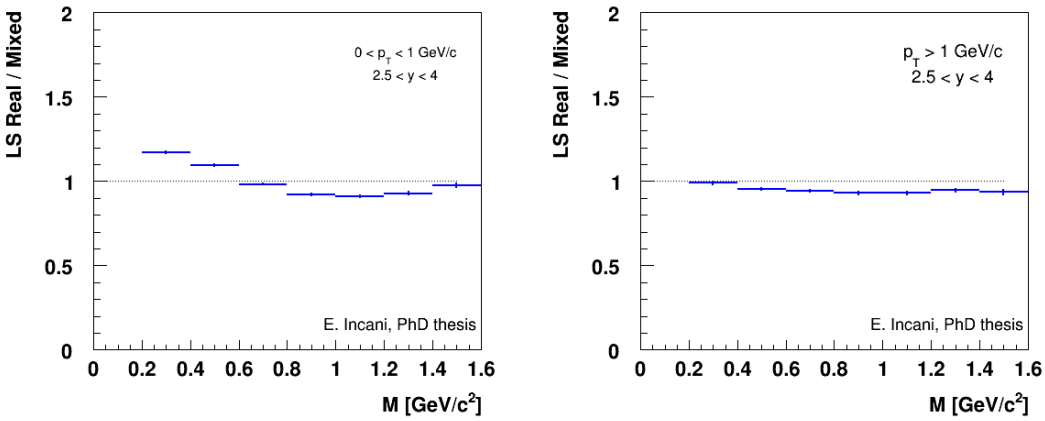

Figure 4.7: Ratio between the real and mixed LS mass spectra.

4.2.3.3 Evaluation of the fraction of correlated like-sign pairs

The background subtraction based on formula 4.3 assumes implicitly that the like-sign pairs are uncorrelated. In principle, decay chain of beauty mesons and $B - \overline{B}$ oscillations (as described in the previous chapter) can give correlated like-sign pairs. This contribution can be estimated once the open beauty content in the OS sample is known. This one is extracted measuring the open charm contribution in the OS mass spectrum, as it will be shown in the following sections, and using the ratio between open charm and open beauty cross sections measured by LHCb ($\sigma_c BR^2 = 6.1$ mb$\cdot 0.10^2$, $\sigma_b BR^2 = 0.284$ mb$\cdot 0.11^2$ [74][75]). In figure 4.10 we show the mass spectrum for LS pairs. In the region $M < 1.5$ GeV/c^2 the open beauty amounts to $\approx 0.5\%$, thus it can be neglected.

4.2.3.4 Ratio between signal and background

To conclude this section about the combinatorial background, we have evaluated the signal to background ratio for p_T greater than 1 GeV/c. As it is shown in the Figure 4.11 at the light vector mesons mass this ratio is of the order of 1. In Fig. 4.12 this ratio is shown in different p_T bins in the range covered in this analysis.

4.2.4 Signal extraction

After subtracting the combinatorial background from the OS mass spectrum, we obtain the raw signal mass spectrum, shown in Fig. 4.13.

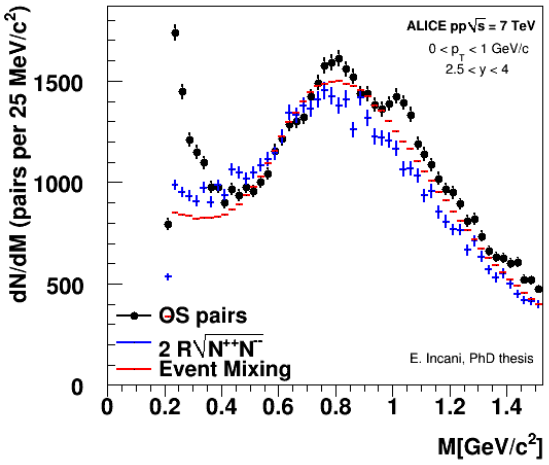

Figure 4.8: Comparison of background estimation using event mixing (red line) or like sign pairs (blue points) for $p_T < 1$ GeV/c. The opposite-sign mass spectrum is superimposed.

The processes contributing to the dimuon mass spectrum are the light meson (η, ρ, ω, η' , ϕ) decays into muons and the correlated semi-leptonic open charm and beauty decays, which are simulated as detailed in Chapter 3. The simulation results are then subjected to the same reconstruction and selection chain as the real data. The invariant mass spectrum is fitted with a superposition of these contributions (Fig. 4.14).

The free parameters of the fit are the normalizations of the $\eta \to \mu^+\mu^-\gamma$, $\omega \to \mu^+\mu^-$, $\phi \to \mu^+\mu^-$, and open charm signals. The processes $\eta \to \mu^+\mu^-$ and $\omega \to \mu^+\mu^-\pi^0$ are fixed to $\eta \to \mu^+\mu^-\gamma$ and $\omega \to \mu^+\mu^-$ respectively, according to the relative branching ratios. These are taken from the PDG [60] with the exception of the BR for the ω-Dalitz decay, for which the value found by the NA60 experiment [62] is used (for the values see previous chapter). The contribution from $\rho \to \mu^+\mu^-$ was fixed by the assumption that the production cross sections of ρ and ω are equal [29, 62, 76, 77]. The η' contribution was set fixing the ratio between the η and η' cross sections according to PYTHIA-Perugia-0 [78]. The ratio between the open beauty and open charm was fixed according to the results from the LHCb Collaboration [74, 75].

The main sources of systematic uncertainty are the background normalization (light blue band) and the relative normalization of the sources, mainly due to the error on the branching ratios for the ω and η Dalitz decays (red band).

Thanks to this fit we have obtained the raw numbers of ϕ and $\rho + \omega$ resonances

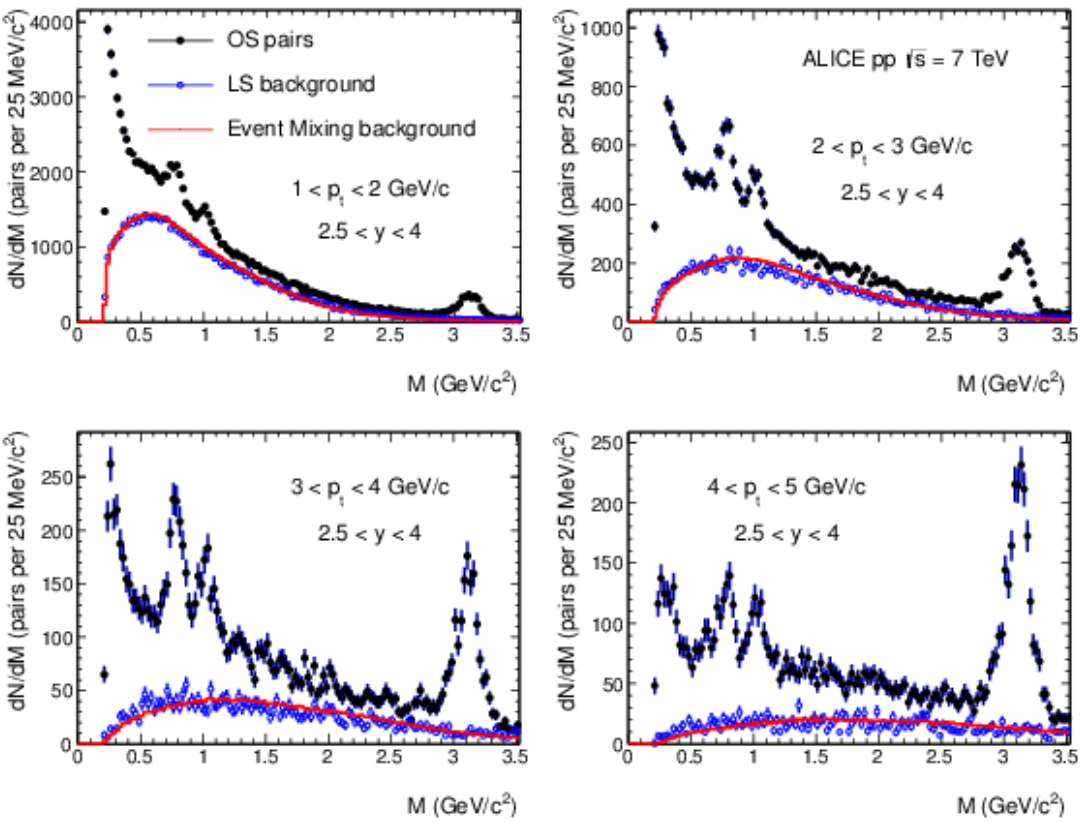

Figure 4.9: Comparison of background estimation using event mixing (red line) or like-sign pairs (blue points) for four bins in p_T. The opposite-sign mass spectra are superimposed.

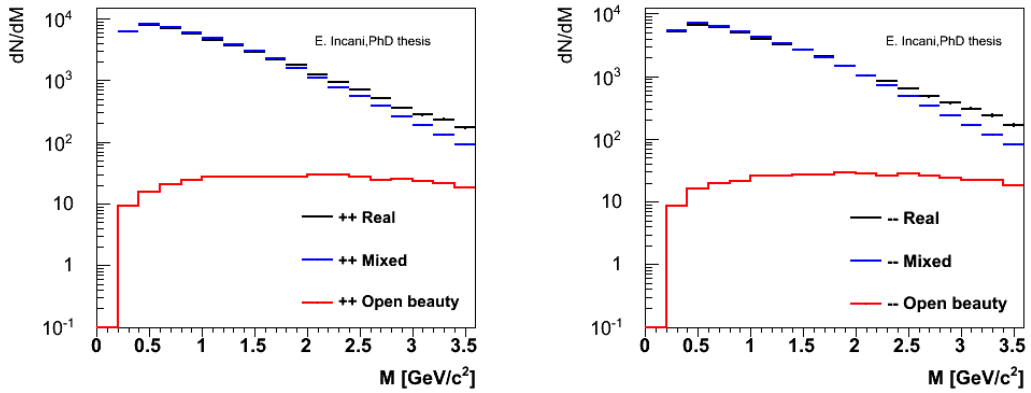

Figure 4.10: Mass spectrum for LS positive (left) and negative (right) real pairs (black histogram), superimposed with the mixed pairs (blue) and correlated open beauty contribution (red).

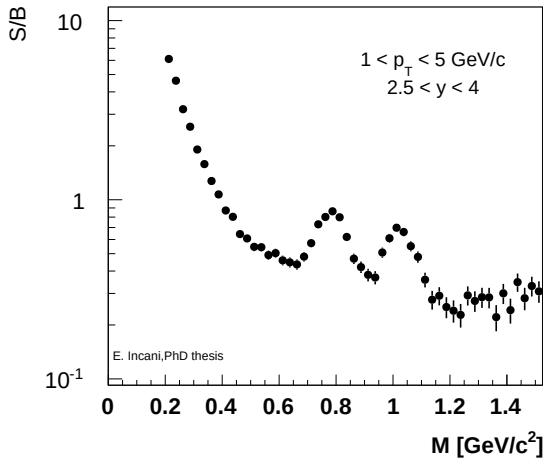

Figure 4.11: Signal over background ratio as a function of the invariant mass.

$N_{\phi}^{raw} = (3.20 \pm 0.15) \times 10^3$ and $N_{\rho+\omega}^{raw} = (6.83 \pm 0.15) \times 10^3$.

As we have already said in Section 4.1, for some runs the information on the number of MB trigger needed to calculate the integrated luminosity was missing, therefore for these runs we cannot compute the cross section. The raw numbers of ϕ and $\rho + \omega$ resonances in the sub-sample used to calculate the σ_{ϕ} and σ_{ω} are: $N_{\phi}^{raw} = (1.93 \pm 0.13) \times 10^3$ and $N_{\rho+\omega}^{raw} = (3.90 \pm 0.16) \times 10^3$.

However, the full statistics can be used for the measurement of the p_T distributions.

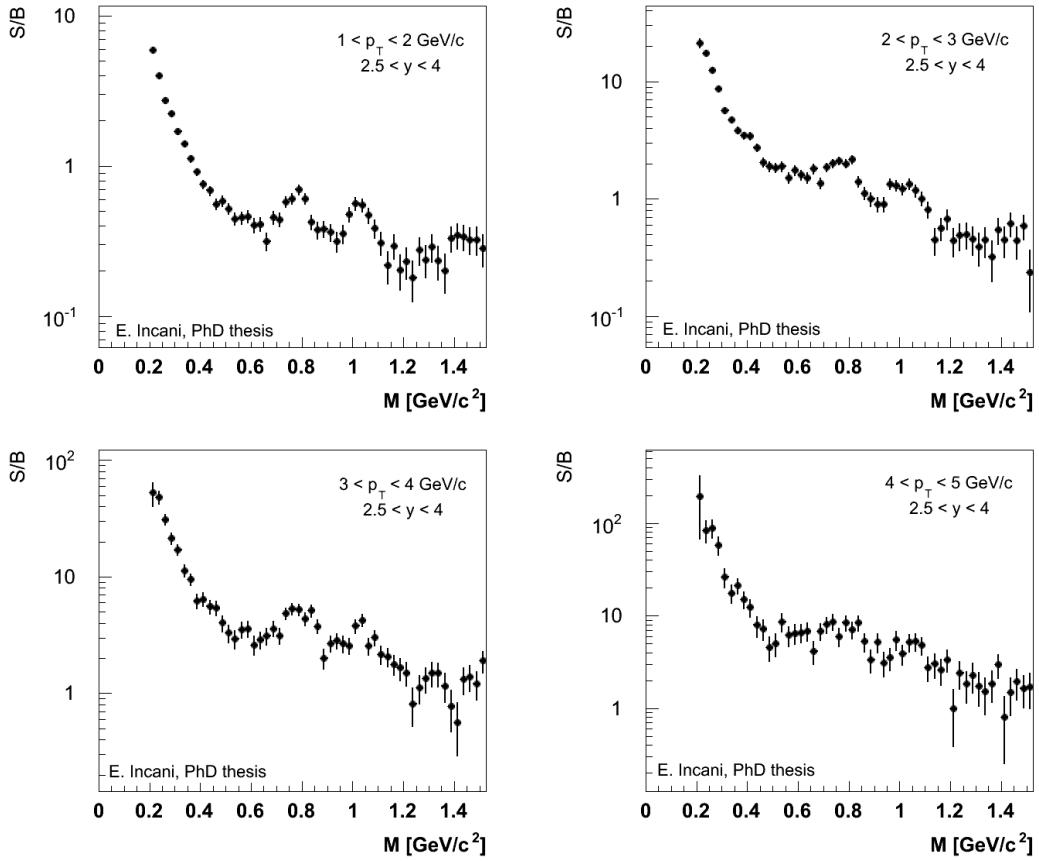

Figure 4.12: Signal over background ratio as a function of the invariant mass for several p_T bins.

4.3 Results

4.3.1 p_T distributions

We have evaluated the number of the ϕ mesons also by performing a fit to the mass spectrum for each $p_T = 0.5$ GeV/c interval in the transverse momentum range covered by the analysis. In Fig. 4.15 the fits from 1 to 5 GeV/c are displayed.

Plots of figure 4.16 show the raw p_T distributions of $\rho + \omega$ (left) and ϕ (right), obtained using the full statistics.

The raw p_T distributions have been corrected for the acceptance×efficiency, evaluated in the previous chapter, in order to obtain the p_T distributions for $\rho+\omega$ (Fig. 4.17 left) and ϕ (Fig. 4.17 right).

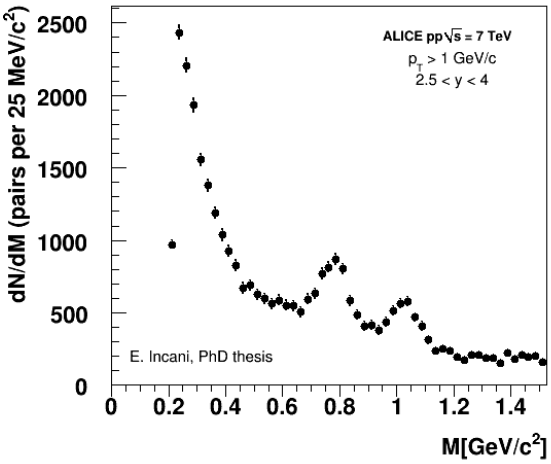

Figure 4.13: Signal after subtraction of the combinatorial background evaluated with the event mixing technique.

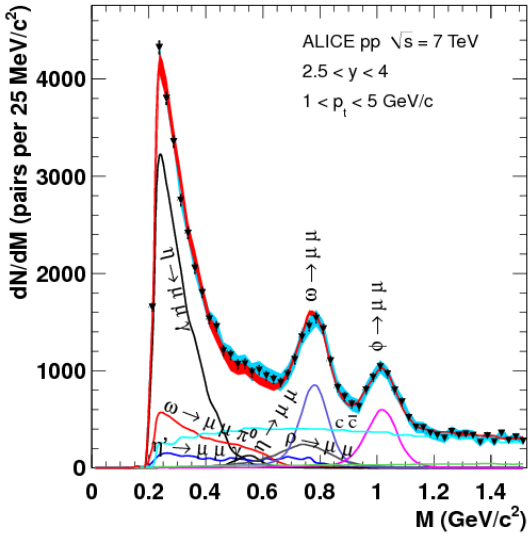

Figure 4.14: Fit to the signal mass spectrum at 7 TeV. Light blue band: systematic uncertainty from the background subtraction. Red band: sum of all the simulated contributions; the width of the red band represents the uncertainty on the relative normalization of the sources.

The distributions are fitted with a power-law function:

$$\frac{dN}{dp_T} \propto \frac{p_t}{\left[1 + \left(\frac{p_t}{A}\right)^2\right]^n} \tag{4.6}$$

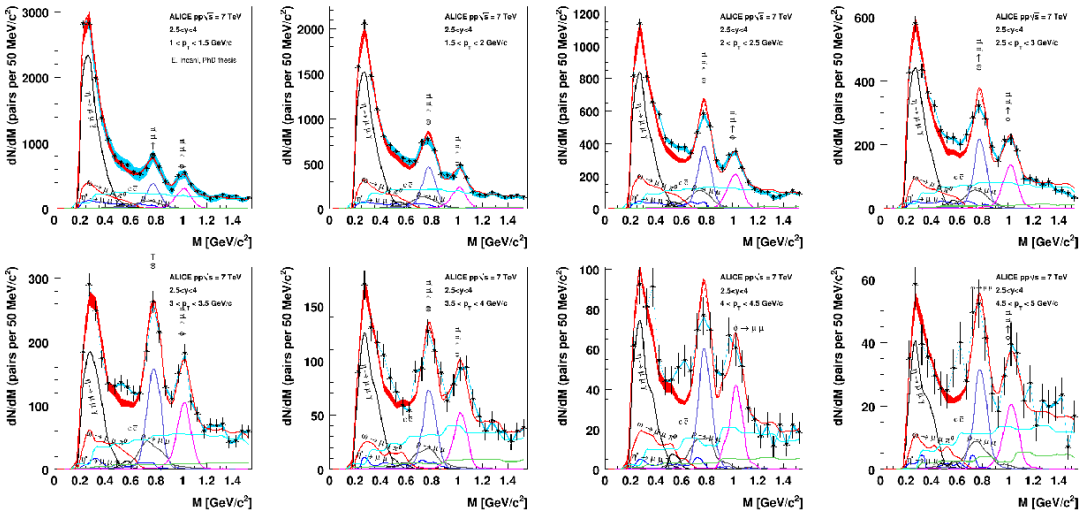

Figure 4.15: Fit to the signal mass spectrum at 7 TeV in several p_T bins.

Table 4.2: Coefficients of the fit to the corrected p_T distributions using 4.6.

	A	n
$\rho + \omega$	1.49 ± 0.16	3.16 ± 0.19
ϕ	1.38 ± 0.28	2.93 ± 0.30

this formula is the same used in AliGenMUONLMR to generate the p_T distributions for the light mesons (see Chapter 3), and Table 4.2 gives the fit parameters.

We have compared the fit using also a Lévi-Tsallis function (eq:4.7 [37]) and the parameters are shown in Table 4.3.

$$\frac{dN}{dp_T} \propto \frac{(n-1)(n-2)}{nT[nT + m(n-2)]} p_T \left(1 + \frac{m_T - m}{nT}\right)^{-n} \tag{4.7}$$

where $m_T = \sqrt{m^2 + p_T^2}$.

As it is shown in Fig. 4.17, in our range of p_T we can not observe differences between the two functions, but at lower p_T (Fig. 4.18) especially for the $\rho + \omega$ p_T distribution, the Lévy-Tsallys functions is higher than power-low.

We have evaluated the ratio $N_\phi/(N_\rho + N_\omega) = BR(\phi \to \mu^+\mu^-)\sigma_\phi/[BR(\rho \to \mu^+\mu^-)\sigma_\rho + BR(\omega \to \mu^+\mu^-)\sigma_\omega]$, corrected for acceptance and efficiency. The p_T dependence of this ratio is constant, as shown in Fig. 4.19. It was calculated for $1 < p_T < 5$ GeV/c, giving $0.416 \pm 0.032(\text{stat}) \pm 0.004(\text{syst})$. Systematic uncertainties (the red boxes) are due to

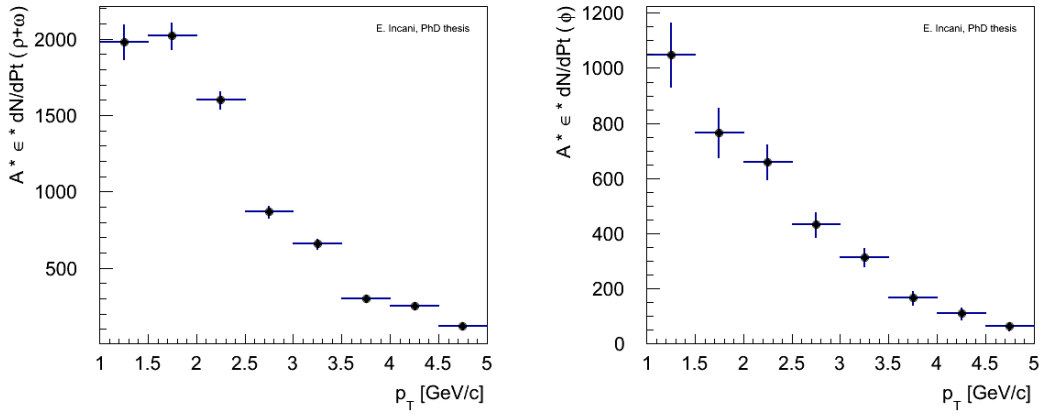

Figure 4.16: Raw p_T distribution for $\rho + \omega$ (left) and ϕ (right).

Table 4.3: Coefficients of the fit to the corrected p_T distributions using a Lévi-Tsallis function.

	T	n
$\rho + \omega$	8.43 ± 1.20	3.33 ± 0.35
ϕ	6.96 ± 1.54	3.59 ± 0.70

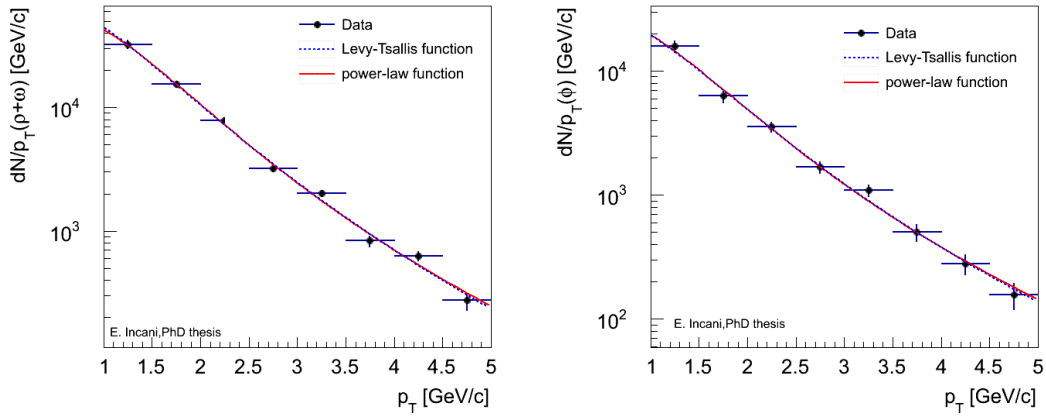

Figure 4.17: p_T distribution for $\rho + \omega$ (left) and ϕ (right).

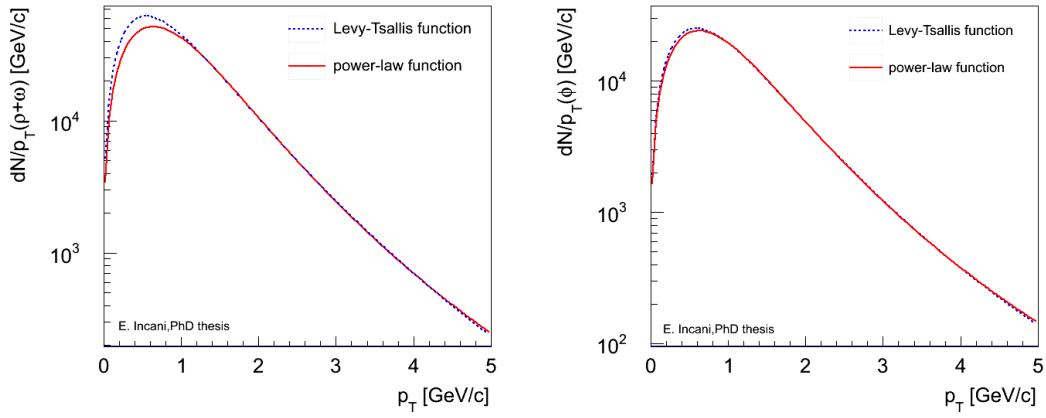

Figure 4.18: Function used to fit p_T distribution for $\rho + \omega$ (left) and ϕ (right), in red the power-low, in blue the Ĺevy-Tsallis function.

the normalizations of $\omega \to \mu^-\mu^+\pi^0$, $\eta \to \mu^-\mu^+\gamma$ and combinatorial background. The uncertainty due to the acceptance and the efficiency is negligible.

4.3.2 Differential ϕ cross section

The ϕ production cross section was evaluated in the range $2.5 < y < 4$, $1 < p_T < 5$ GeV/c through the formula:

$$\sigma_\phi = \frac{N_\phi^{raw}}{A_\phi \epsilon_\phi BR(\phi \to l^+l^-)L} \tag{4.8}$$

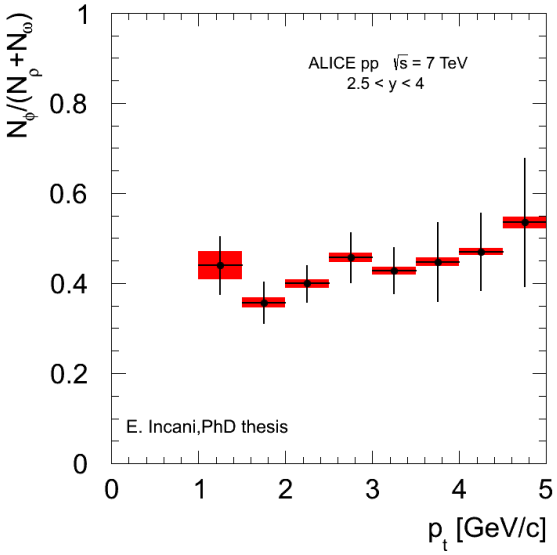

Figure 4.19: Ratio $N_\phi/(N_\rho + N_\omega) = BR(\phi \to \mu^+\mu^-)\sigma_\phi/[BR(\rho \to \mu^+\mu^-)\sigma_\rho + BR(\omega \to \mu^+\mu^-)\sigma_\omega]$ as a function of the dimuon transverse momentum.

where N_ϕ is the measured number of the ϕ mesons, A_ϕ and ϵ_ϕ are the geometrical acceptance and the efficiency respectively, $BR(\phi \to l^+l^-) = (2.95 \pm 0.03) \times 10^{-4}$ is the branching ratio into lepton pairs (we have assumed the lepton universality as described in the previous chapter).

As said before, the numbers of resonances have been evaluated using two methods:

- fit the signal in the whole p_T range obtaining the raw number and then correct for the acceptance×efficiency;
- integrate the p_T distribution corrected for the acceptance×efficiency

With the first method we obtain $N_\phi^{raw} = (1.73 \pm 0.12) \times 10^3$, $A_\phi\epsilon_\phi = 11.6\%$ and thus the cross section value is 0.910 ± 0.062 mb; with the second one, $N_\phi = (15.45 \pm 0.14) \times 10^3$ and the cross section value is 0.940 ± 0.084 mb.

In order to check if those two values are compatible, the criterion described in [79] was used. According to this criterion, results are compatible if the difference between the two measurements is lower than the difference in quadrature between the errors. The difference between the two measurements is $\Delta = 0.030$ and $\delta\Delta = \sqrt{0.084^2 - 0.062^2} = 0.057$ so that they are compatible within one sigma.

We have used the second approach, because in this way the dependence of the acceptance correction on the input p_T distribution used for the Monte Carlo simulation becomes insignificant and we obtain $\sigma_\phi(1 < p_T < 5 \text{ GeV}/c,\ 2.5 < y < 4) = 0.940 \pm 0.084(\text{stat})$ mb.

Different sources of systematic error were considered, and the greatest part of contributions to the systematic uncertainty, common to all analyses in the dimuon channel, is extensively discussed elsewhere [80]:

- The uncertainty on the background normalization of 5% translates into a 2% systematic uncertainty on the cross section, which was evaluated by varying the normalization by ±5% and repeating the fit procedure on the resulting background subtracted spectra.

- The muon trigger efficiency is 4%, as estimated from the J/ψ analysis by comparing the results with one and two matched muons (a similar check at the ϕ mass is not possible because the sample with one matched muon is affected by a too large background at the ϕ mass).

- The tracking efficiency was evaluated starting from the determination of the efficiency for individual chambers, computed by taking advantage from the redundancy of the tracking information in each station. The same procedure was applied to the data and to the Monte Carlo simulations. The difference in the results gives the systematic uncertainty on the tracking efficiency. The systematic uncertainty on tracking efficiency is around 3%.

- The ratio $N_\mu^{MB}/N_\mu^{\mu-MB}$, that connects the minimum bias data sample used to normalize to the inelastic cross section and the dimuon trigger sample, is affected by a 3% error.

- The error on the minimum bias cross section is mainly due to the uncertainties in the beam intensities and in the analysis procedure adopted for the determination of the beam luminosity via the van der Meer scan; its value is 4%.

- In addition the systematic uncertainty resulting from the uncertainty on the ϕ branching ratio into dileptons is 1%.

The uncertainty on the input p_T distribution in the Monte Carlo simulation is negligible, as discussed above. The uncertainty due to the unknown spin alignment of ϕ was evaluated on the basis of the measurements reported in [81–83] and was found to be negligible. Summing in quadrature all those errors, one obtains finally:

$$\sigma_\phi(1 < p_T < 5 \text{ GeV}/c,\ 2.5 < y < 4) = 0.940 \pm 0.084(\text{stat}) \pm 0.076(\text{syst}) \text{ mb}. \quad (4.9)$$

The differential cross section $d^2\sigma_\phi/dydp_T$ is shown in Fig. 4.20 and the numerical values are reported in Table 4.4. p_T-dependent contributions to the systematic uncertainties, due to the uncertainty on trigger and tracking efficiency and background subtraction, are indicated as red boxes. The uncertainty on the minimum bias cross section, branching ratio and $N_\mu^{MB}/N_\mu^{\mu-MB}$ ratio contribute to the uncertainty in the overall normalization. As stated above, the ϕ cross section is extracted from a subsample of the data used to determine the p_T distribution, and it is thus affected by a

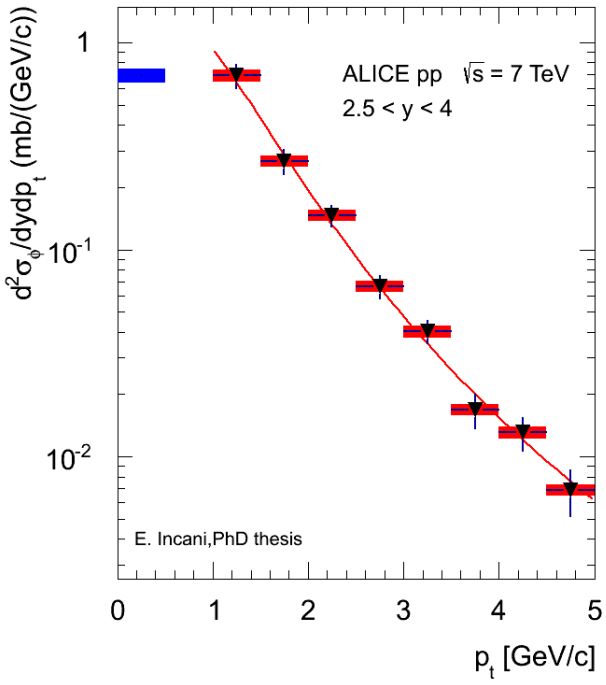

Figure 4.20: Inclusive differential ϕ production cross section $d^2\sigma_\phi/dydp_T$ for $2.5 < y < 4$. The error bars represent the quadratic sum of the statistical and systematic uncertainties, the red boxes the point-to-point uncorrelated systematic uncertainty, the blue box on the left the error on normalization. Data are fitted with Eq. 4.6

Table 4.4: ϕ differential cross section for $2.5 < y < 4$ at $\sqrt{s} = 7$ TeV. Statistical, bin-to-bin uncorrelated and correlated systematic errors are reported.

p_T [GeV/c]	$\mathrm{d}^2\sigma_\phi/\mathrm{d}y\mathrm{d}p_T$ [mb/ [GeV/c]]
$[1, 1.5]$	$0.695 \pm 0.079 \pm 0.046 \pm 0.051$
$[1.5, 2]$	$0.268 \pm 0.032 \pm 0.018 \pm 0.020$
$[2, 2.5]$	$0.147 \pm 0.014 \pm 0.010 \pm 0.011$
$[2.5, 3]$	$0.0665 \pm 0.0074 \pm 0.0044 \pm 0.0049$
$[3, 3.5]$	$0.0403 \pm 0.0044 \pm 0.0027 \pm 0.0030$
$[3.5, 4]$	$0.0169 \pm 0.0031 \pm 0.0011 \pm 0.0012$
$[4, 4.5]$	$0.0131 \pm 0.0022 \pm 0.0009 \pm 0.0010$
$[4.5, 5]$	$0.0069 \pm 0.0017 \pm 0.0005 \pm 0.0005$

larger statistical uncertainty, resulting in a 5% contribution to the normalization error. The curve is obtained fitting the expression in Eq. 4.6 to the differential cross section.

4.3.3 ρ/ω and ϕ/ω ratios

In order to extract the ω cross section, the ρ and ω contributions must be disentangled, leaving the ρ normalization as an additional free parameter in the fit to the dimuon mass spectrum. The fit is shown in Fig. 4.21.

Leaving the ρ/ω yield ratio free in the mass spectrum fit we obtain:

$$\frac{\sigma_\rho}{\sigma_\omega} = \frac{N_\rho/BR(\rho \to \mu^+\mu^-)}{N_\omega/BR(\omega \to \mu^+\mu^-)} = 1.15 \pm 0.20(\text{stat.}) \pm 0.12(\text{syst.}) \tag{4.10}$$

The rather large error is due mainly to the non optimal mass resolution ($\sim$ 50 MeV at the ω mass) and to the limited statistics. The stability of the ratio was checked by changing the background by 10%, which corresponds to twice the uncertainty in the normalization, the $\omega_{Dalitz}/\omega_{2\ body}$ ratio up to $\pm$15% and the η'/η ratio up to $\pm$20%. Results are shown in Fig. 4.22. The resulting systematic uncertainty is 12%, the overall uncertainty is thus dominated by the statistical error.

Once the ratio $\sigma_\rho/\sigma_\omega$ is measured, the ratio $\sigma_\phi/\sigma_\omega$ can be extracted from $N_\phi/(N_\rho + N_\omega) = BR(\phi \to \mu^+\mu^-)\sigma_\phi/[BR(\rho \to \mu^+\mu^-)\sigma_\rho + BR(\omega \to \mu^+\mu^-)\sigma_\omega]$, already obtained in 4.3.1. Results are reported in Fig. 4.23 as a function of p_T. The blue box on the left represents the overall uncertainty on the ratio due to the uncertainty on $\sigma_\rho/\sigma_\omega$.

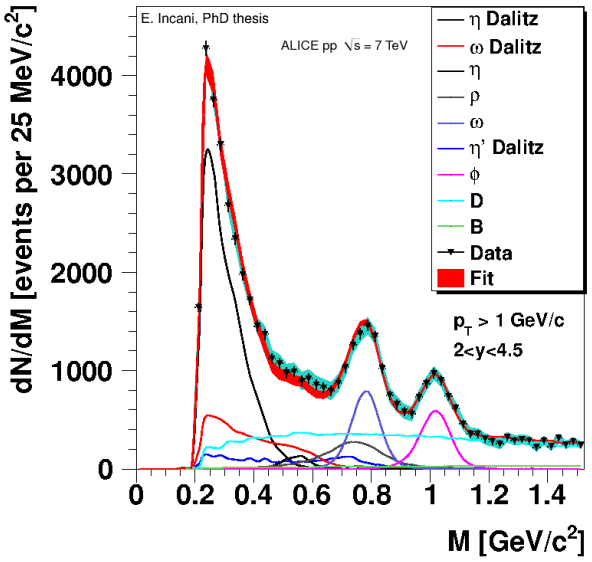

Figure 4.21: Dimuon invariant mass spectrum in pp at $\sqrt{s} = 7$ TeV after combinatorial background subtraction for $1 < p_T < 5$ GeV/c leaving the ρ normalization as an additional free parameter.

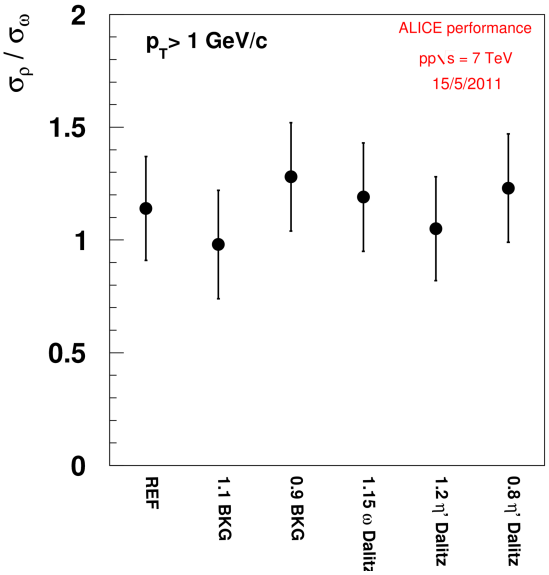

Figure 4.22: Systematic checks to study $\sigma_\rho/\sigma_\omega$.

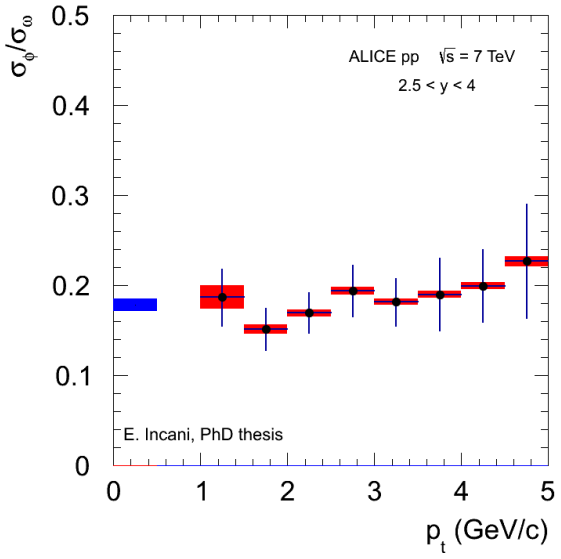

Figure 4.23: Ratio $\sigma_\phi/\sigma_\omega$ as a function of the dimuon transverse momentum.

4.3.4 ω cross section

The ω cross section for $1 < p_T < 5$ GeV and $4 < y < 2.5$ is obtained combining the results on $\sigma_\phi/\sigma_\omega$ and σ_ϕ:

$$\sigma_\omega(1 < p_T < 5 \text{ GeV}/c,\ 2.5 < y < 4) = 5.28 \pm 0.54(\text{stat}) \pm 0.49(\text{syst}) \text{ mb}. \quad (4.11)$$

The resulting $d^2\sigma_\omega/dydp_T$ is shown in Fig. 4.24 and the numerical values are reported in Table 4.5. The curve is obtained fitting the expression in Eq. 4.6 to the differential cross section.

4.3.5 Rapidity distributions and differential ϕ and ω cross sections as a function of y

In order to determine the rapidity distributions, we fit the mass spectrum for each $y = 0.2$ interval in the p_T range covered by the analysis (Fig. 4.25). Figure 4.26 shows on the top the raw rapidity distribution of $\rho+\omega$ (left) and ϕ (right) and on the bottom the rapidity distributions for $\rho+\omega$ (left) and ϕ (right). The acceptance×efficiency-corrected rapidity distributions are fitted using the function used in AliGenMUONLMR (Eq.4.12),

Table 4.5: ω differential cross section for $2.5 < y < 4$ at $\sqrt{s} = 7$ TeV. Statistical, bin-to-bin uncorrelated and correlated systematic errors are reported.

p_T [GeV/c]	$\mathrm{d}^2\sigma_\omega/\mathrm{d}y\mathrm{d}p_T$ [mb/ [GeV/c]]
$[1, 1.5]$	$3.69 \pm 0.35 \pm 0.24 \pm 0.31$
$[1.5, 2]$	$1.75 \pm 0.15 \pm 0.12 \pm 0.15$
$[2, 2.5]$	$0.857 \pm 0.069 \pm 0.057 \pm 0.073$
$[2.5, 3]$	$0.339 \pm 0.029 \pm 0.022 \pm 0.029$
$[3, 3.5]$	$0.220 \pm 0.019 \pm 0.011 \pm 0.019$
$[3.5, 4]$	$0.0880 \pm 0.0088 \pm 0.0058 \pm 0.0075$
$[4, 4.5]$	$0.0648 \pm 0.0062 \pm 0.0043 \pm 0.0055$
$[4.5, 5]$	$0.0301 \pm 0.0039 \pm 0.0020 \pm 0.0026$

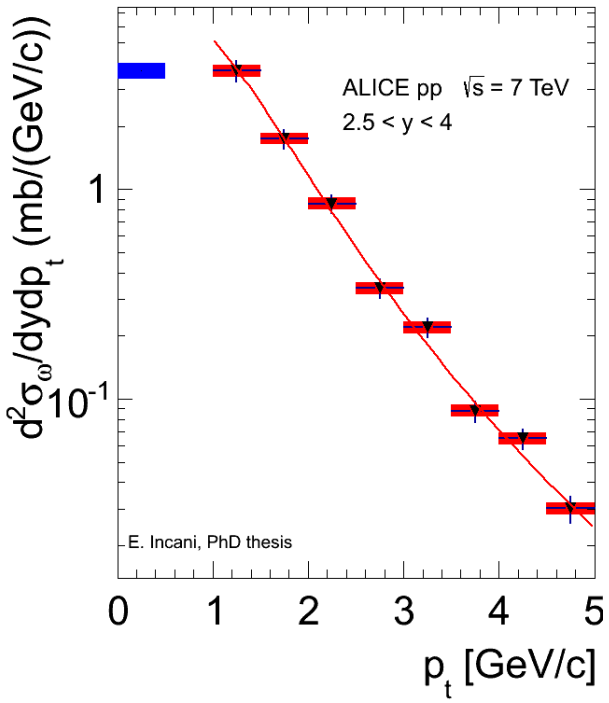

Figure 4.24: Inclusive differential ω production cross section $d^2\sigma_\omega/dydp_T$ for $2.5 < y < 4$. The error bars represent the quadratic sum of the statistical and systematic uncertainties, the red boxes the point-to-point uncorrelated systematic uncertainty, the blue box on the left the error on normalization. Data are fitted with Eq. 4.6.

and the parameters y_0 and σ_y are fixed at the values used in the generator.

$$\frac{dN}{dy} = \begin{cases} \text{const.} & \text{for } |y| < y_0 \\ e^{-\frac{1}{2}\frac{(|y|-y_0)^2}{\sigma_y^2}} & \text{for } |y| > y_0 \end{cases} \tag{4.12}$$

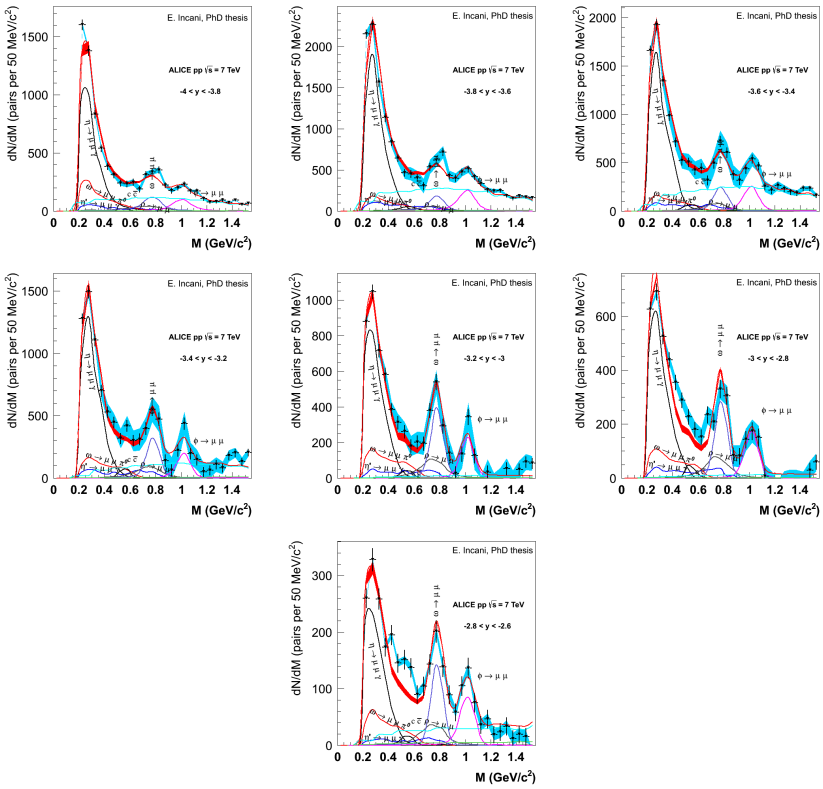

Figure 4.25: Fit to the signal mass spectrum at 7 TeV in several rapidity bins.

The differential cross sections $d^2\sigma_\phi/dydp_T$ and $d^2\sigma_\omega/dydp_T$ are shown in Fig. 4.27 and 4.28 (numerical values are shown in Table 4.6), The error bars represent the quadratic sum of the statistical and systematic uncertainties, the red boxes the point-to-point uncorrelated systematic uncertainty, the blue box on the left the error on normalization. The open symbols are the reflection points in the regions of positive rapidity.

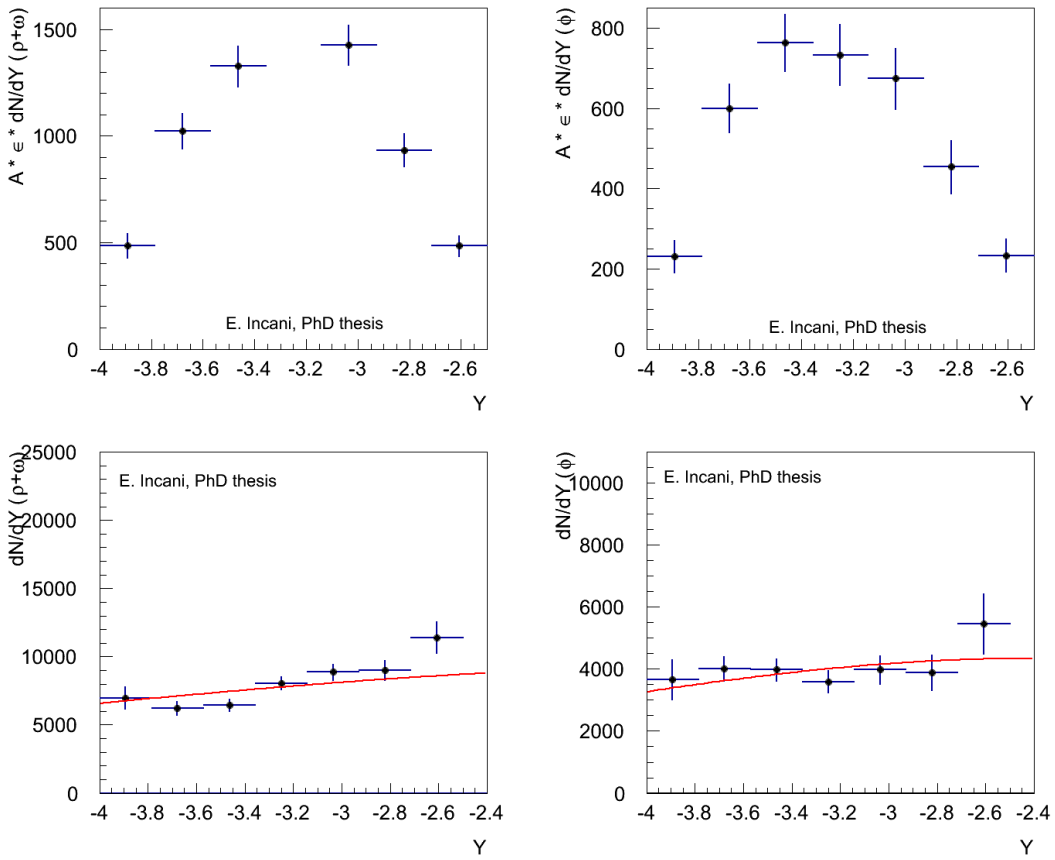

Figure 4.26: Raw y distribution for $\rho + \omega$ (left) and ϕ (right) on the top, and the y distributions for $\rho + \omega$ (left) and ϕ (right).

Table 4.6: ϕ and ω differential cross sections for $1 < p_T < 5$ GeV/c at $\sqrt{s} = 7$ TeV. Statistical, bin-to-bin uncorrelated and correlated systematic errors are reported.

y	$\mathrm{d}^2\sigma_\phi/\mathrm{d}y\mathrm{d}p_T$ [mb/GeV/c]	$\mathrm{d}^2\sigma_\omega/\mathrm{d}y\mathrm{d}p_T$ [mb/GeV/c]
$[4.0, 3.8]$	$0.150 \pm 0.026 \pm 0.010 \pm 0.014$	$0.807 \pm 0.095 \pm 0.053$
$[3.8, 3.6]$	$0.165 \pm 0.017 \pm 0.011 \pm 0.015$	$0.721 \pm 0.059 \pm 0.048$
$[3.6, 3.4]$	$0.163 \pm 0.015 \pm 0.011 \pm 0.015$	$0.747 \pm 0.054 \pm 0.049$
$[3.4, 3.2]$	$0.148 \pm 0.015 \pm 0.010 \pm 0.013$	$0.933 \pm 0.057 \pm 0.062$
$[3.2, 3.0]$	$0.164 \pm 0.019 \pm 0.011 \pm 0.015$	$1.03 \pm 0.07 \pm 0.07$
$[3.0, 2.8]$	$0.160 \pm 0.023 \pm 0.011 \pm 0.014$	$1.04 \pm 0.09 \pm 0.07$
$[2.8, 2.6]$	$0.225 \pm 0.040 \pm 0.015 \pm 0.020$	$1.32 \pm 0.13 \pm 0.09$

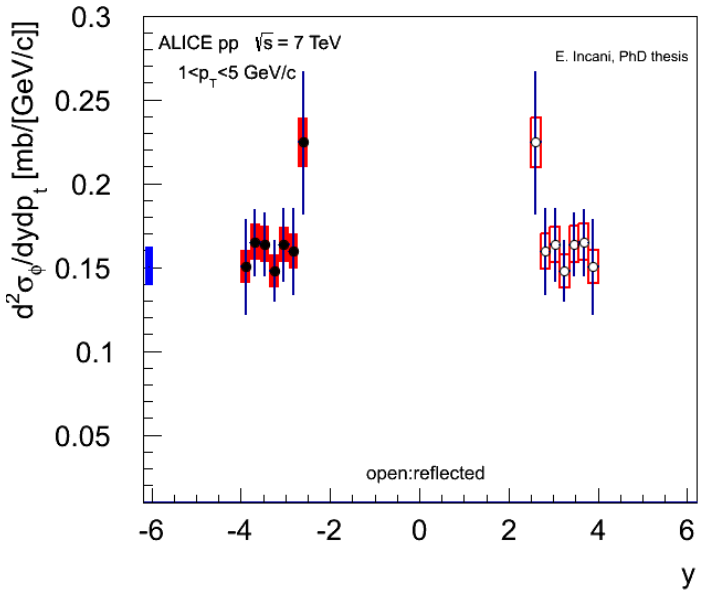

Figure 4.27: Differential ϕ production cross section $d^2\sigma_\phi/dydp_T$ for $1 < p_T < 5$ GeV/c. The error bars represent the quadratic sum of the statistical and systematic uncertainties, the red boxes the point-to-point uncorrelated systematic uncertainty, the blue box on the left the error on normalization. The open symbols are the reflection points in the regions of positive rapidity.

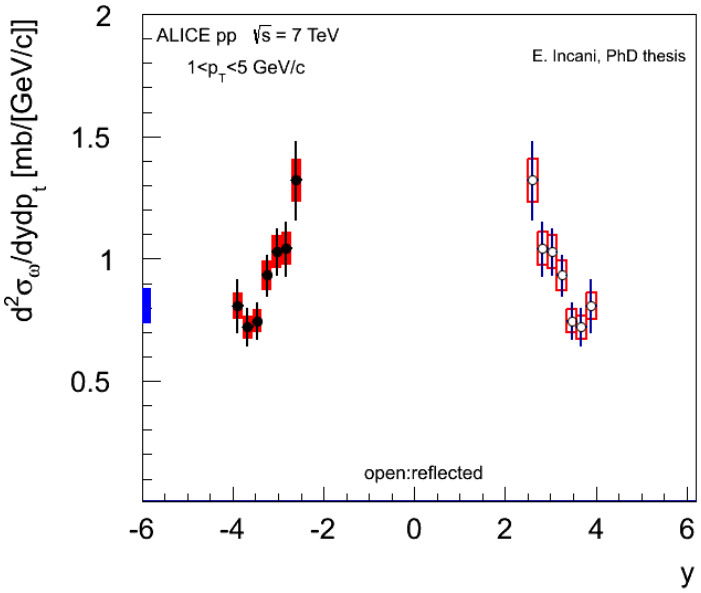

Figure 4.28: $d^2\sigma_\omega/dydp_T$ for $1 < p_T < 5$ GeV/c. The error bars represent the quadratic sum of the statistical and systematic uncertainties, the red boxes the point-to-point uncorrelated systematic uncertainty, the blue box on the left the error on normalization. The open symbols are the reflection points in the regions of positive rapidity.

5

Low mass vector meson analysis via dimuon channel in pp collision at $\sqrt{s} = 2.76$ TeV

Contents

In this chapter I describe the extraction of the inclusive ϕ cross section in pp collisions at $\sqrt{s} = 2.76$ TeV through its decay in the dimuon channel. The p_T and rapidity regions covered in this analysis are $p_T > 1$ GeV/c and $2.5 < y < 4$.

The analysis strategy is the same as at 7 TeV (Chapter 4): the OS pairs, after combinatorial background subtraction, have been described as a superposition of the light meson decays in muon pairs, in addition to open charm and open beauty.

5.1 Data sample

Data were taken during the March 2011 pp run at $\sqrt{s} = 2.76$ TeV (the run list is reported in the Appendix 6.3.2).

In this analysis we have also used data collected with a single-muon trigger and the integrated luminosity has been evaluated using the MB trigger.

The minimum bias cross section σ_{MB} value at 2.76 TeV is 54.8 ± 0.1 mb [70] and the integrated luminosity is 17.6 nb^{-1}, much lower than the one used for the 7 TeV analysis, 55.7 nb^{-1}. The statistical uncertainty for the analysis at 2.76 TeV is thus much larger.

5.2 Event selection and analysis

5.2.1 Data selection

We have applied the same event selection as at 7 TeV in the data analysis at 2.76 TeV:

- a cut on the muon pseudorapidity $-4 < \eta_\mu < -2.5$, that removes the tracks at the borders of the detector acceptance;
- the matching between the tracks reconstructed in the muon tracker and the tracklets reconstructed in the muon trigger was required for both tracks;
- a cut on dimuon rapidity $-4 < y_{\mu\mu} < -2.5$.

With the selected muons, the invariant mass spectrum was obtained both for OS and LS muon pairs. The numbers of OS and LS muon pairs in the full sample that satisfy the selections are:

- $OS \sim 19600$
- $LS^{++} \sim 4500$
- $LS^{--} \sim 5500$

For comparison, the corresponding statistics at 7 TeV is one order of magnitude higher ($OS \sim 29.1 \cdot 10^4$, $LS^{++} \sim 9.1 \cdot 10^4$, $LS^{--} \sim 10.6 \cdot 10^4$).

5.3 Background subtraction

We have evaluated the background using the event mixing technique, which is described in the $\sqrt{s} = 7$ TeV analysis in the previous chapter 4.2.3. Also in this case, the

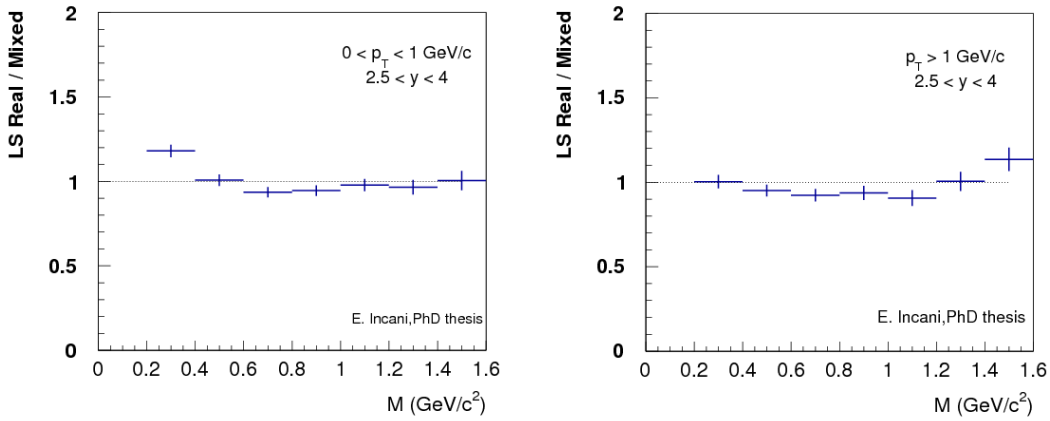

Figure 5.1: Ratio between the real LS and LS produced using the event mixing technique, for $0 < p_T < 1$ GeV/c (left) and $p_T > 1$ GeV/c (right).

quality of the event mixing was tested comparing the like sign mass spectra obtained from the event mixing and from the data. Figure 5.1 shows the ratio between the LS real and mixed spectra as a function of the mass. The ratio for $p_T > 1$ GeV/c is about 0.97, differing from the unity by about 3%, which is taken as an estimate of the systematic uncertainty on background subtraction. It reflects in 1% uncertainty in the determination of N_ϕ, which will be shown below.

Figure 5.2 shows the invariant mass spectrum for opposite sign muon pairs for $1 < p_T < 4$ GeV/c, together with the combinatorial background estimated with the event mixing technique. The plot is limited at 4 GeV/c because for p_T bigger than this value the statistics is too low to extract the numbers of resonances. The signal has been obtained subtracting the background to the OS mass spectrum. The ratio between the signal and the background is shown in figure 5.3, compared with the one at 7 TeV. We can see that at the ω and ϕ pole masses, this ratio at 2.76 TeV is about twice as high as the same quantity at 7 TeV.

5.4 Signal extraction

The fit to the signal invariant mass spectrum, performed with the criteria already detailed in Section 4.2.4, is reported in Fig. 5.4. The contributions have been simulated as described in Chapter 3. The red band comes from the uncertainty in the relative

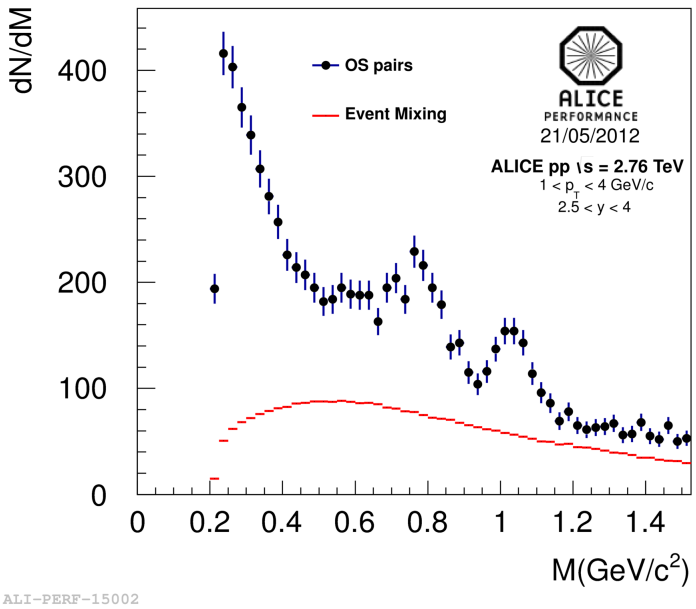

Figure 5.2: Raw invariant mass spectra for opposite-sign muon pairs in pp at $\sqrt{s} =$ 2.76 TeV (full circles) and combinatorial background (red histogram).

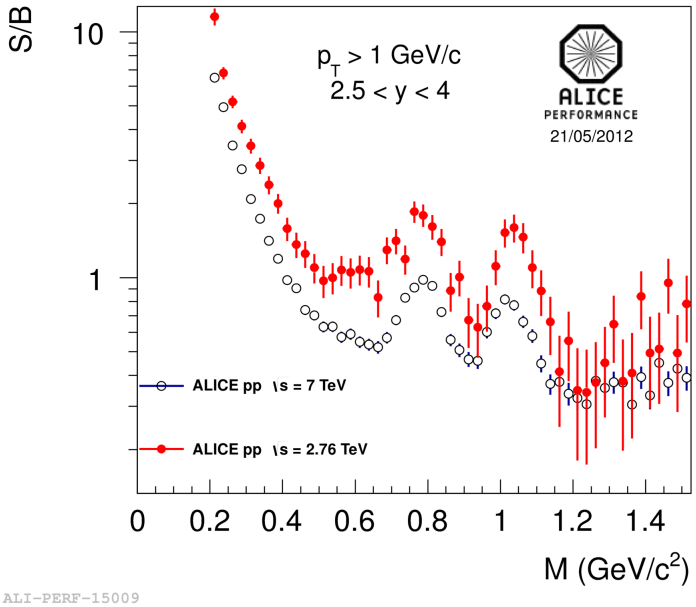

Figure 5.3: Signal over background ratio as a function of the invariant mass for the data at 2.76 TeV (red full circles) and 7 TeV (black open circles).

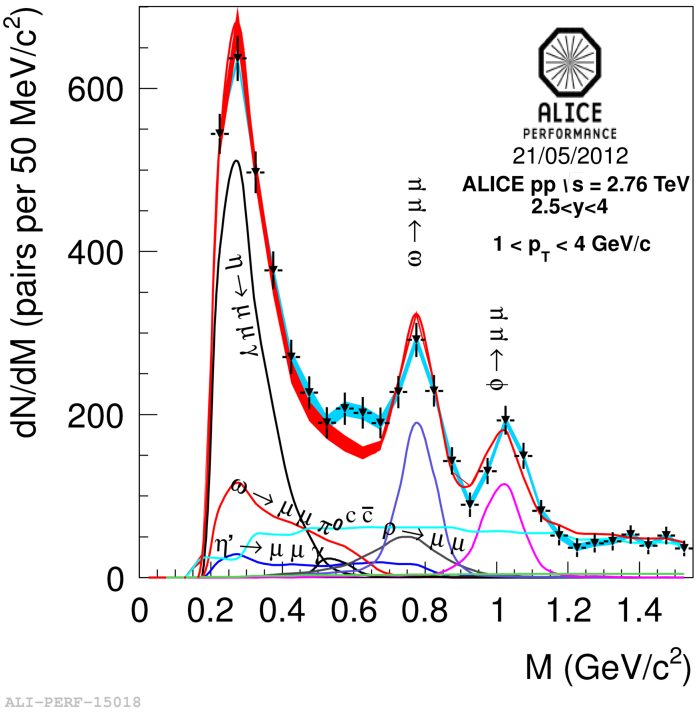

Figure 5.4: Dimuon invariant mass spectrum in pp at $\sqrt{s} = 2.76$ TeV after combinatorial background subtraction for $1 < p_T < 4$ GeV/c (triangles). Light blue band: systematic uncertainty from background subtraction. Red band: sum of all simulated contributions. The width of the red band represents the uncertainty on the relative normalization of the sources.

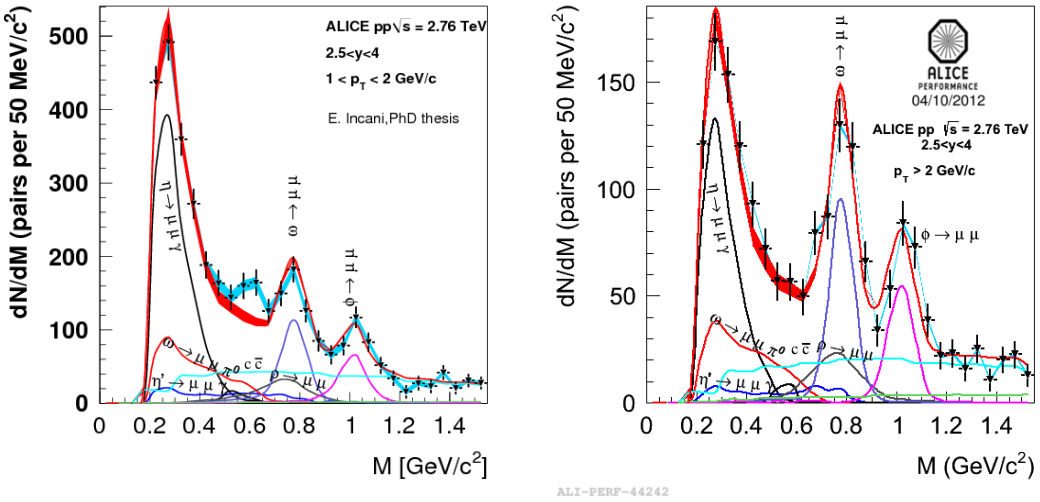

Figure 5.5: Dimuon invariant mass spectrum in pp at $\sqrt{s} = 2.76$ TeV after combinatorial background subtraction for $1 < p_T < 2$ GeV/c (left) and for $p_T > 2$ GeV/c (right).

normalization of the sources, mainly due to the error on the branching ratios for the ω and η' Dalitz decays. The blue band represents a systematic error coming from background subtraction.

A small excess around $M = 0.6$ GeV/c^2, which does not appear in the 7 TeV data, is present. It is located in the region $1 < p_T < 2$ GeV/c, as can be inferred by comparing the two plots in Fig. 5.5.

We have tried several possible selections in order to remove this excess, including cuts on the single track p_T, correlation between momentum and DCA, R_{abs} (R_{abs} is the radial coordinate of the track at the end of the front absorber), and asking/removing the requirement on the trigger match. As shown in Fig. 5.6, none of them was successful in removing this excess, rather we have a worse fit in the ϕ region. We have thus decided to use the same cuts used in the 7 TeV analysis and limit our analysis for $p_T > 1$ GeV/c to the ϕ, for which the yield is not affected by this excess, while for the ω, which is closer to this excess, we preferred not to compute the cross section for $p_T < 2$ GeV. Since the excess is not present for $p_T > 2$ GeV/c, the analysis in this range is extended to both particles.

The raw numbers of ϕ and $\rho + \omega$ resonances in the peaks are $N_\phi = 350 \pm 40$ and $N_{\rho+\omega} = 801 \pm 43$ (about 10% of the statistics collected at 7 TeV). As at 7 TeV, the signal for $p_T < 1$ GeV/c is not under sufficient control, as can be seen in figure 5.7,

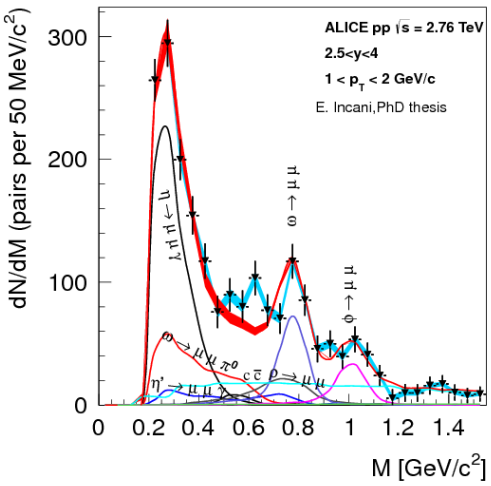

(a) Other cuts in single muons : trigger matching, p as a function of DCA (see Chapter 4.2.2)

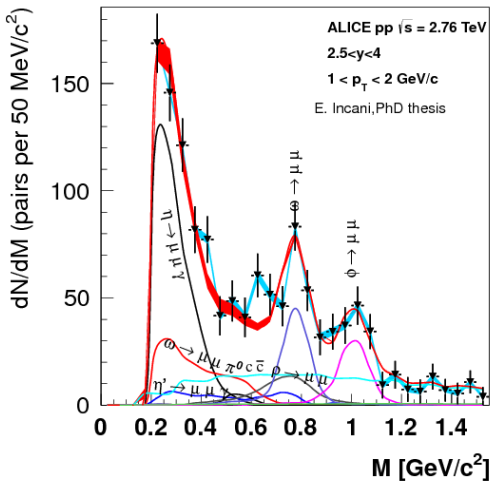

(b) Other cuts in single muons: trigger matching, $p_{T\mu} > 0.5$ GeV/c.

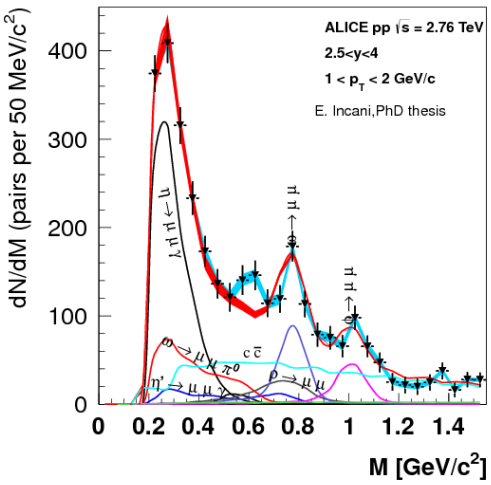

(c) Other cuts in single muons: trigger matching,$17.5 < R_{abs} < 89.5$ cm

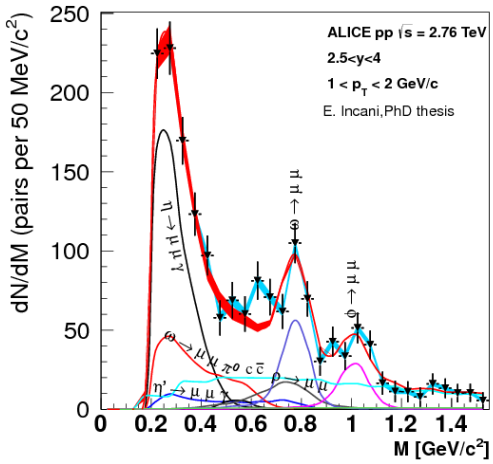

(d) Other cuts in single muons:$17.5 < R_{abs} < 89.5$ cm, $p_{T\mu} > 0.4$ GeV/c

Figure 5.6: Dimuon invariant mass spectrum in pp at $\sqrt{s} = 2.76$ TeV after combinatorial background subtraction for $1 < p_T < 2$ GeV/c obtained using usually cut: pseudorapidity $-4 < \eta_\mu < -2.5$ and rapidity $-4 < y_{\mu\mu} < -2.5$ with other cuts.

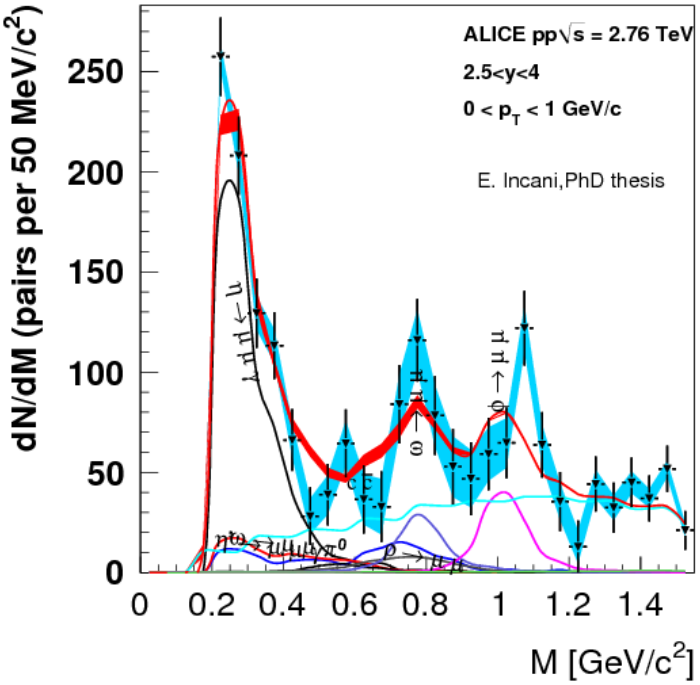

Figure 5.7: Dimuon invariant mass spectrum in pp at $\sqrt{s} = 2.76$ TeV after combinatorial background subtraction for $p_T < 1$ GeV/c.

where the ϕ peak appears displaced from its nominal position. We therefore limit our analysis to $p_T > 1$ GeV/c.

5.5 ϕ integrated cross sections

In order to evaluate the ϕ cross section we have applied the same procedure used in the analysis at 7 TeV. The ϕ cross section has been calculated as:

$$\sigma_\phi = \frac{N_\phi^{raw}}{A_\phi \epsilon_\phi BR(\phi \to l^+l^-)L} \tag{5.1}$$

N_ϕ is the number of ϕ mesons obtained from the fit; $BR(\phi \to l^+l^-)$ is the branching ratio into lepton pairs for the ϕ decay, used instead of $BR(\phi \to \mu^+\mu^-)$; the product between acceptance and efficiency $A \times \epsilon$ is 0.1177 ± 0.0023(syst), with a negligible statistical error. In Chapter 3 I have described two different p_T distributions for the

ρ, ω and ϕ: the difference between the values obtained with the two assumptions has been used as a systematic error.

The cross section value obtained is 0.573 ± 0.65(stat) mb.

Different sources of systematic error were considered, and the greatest part of contributions to the systematic uncertainty, common to all analyses in the dimuon channel, are extensively discussed elsewhere [84]:

- Uncertainty from the background subtraction resulting in an uncertainty in the cross section of 1%.
- Systematic error on the muon trigger efficiency, leading to an uncertainty in the cross section of 5% (described below).
- Systematic error on tracking efficiency, resulting in an uncertainty in the cross section of 4% [84].
- Uncertainty on the ratio $N_{\mu}^{\mu-MB}/N_{\mu}^{MB}$ of 3% [84].
- Systematic error on the minimum bias cross section of 1.9%.
- Uncertainty from $A \times \epsilon$ correction, described in Chapter 3, of 2%.
- Uncertainty on the branching ratio of 1%.

The systematic error on the muon trigger efficiency has been estimated varying uniformly by a certain amount the efficiency of the trigger boards and re-calculating $A \times \epsilon$ (Fig. 5.8). A realistic estimate of the uncertainty on the trigger board is 2% and the resulting variation of the cross section is 5%.

Summing in quadrature all these errors, one obtains finally:

$$\sigma_{\phi}(1 < p_T < 4GeV/c, 2.5 < y < 4) = 0.573 \pm 0.065(\text{stat}) \pm 0.044(\text{syst}).$$

5.5.1 p_T and rapidity distributions

We have evaluated the p_T distribution of ϕ mesons by performing a fit to the mass spectrum for each $p_T = 0.5$ GeV/c interval in the transverse momentum range covered by the analysis (Fig. 5.9).

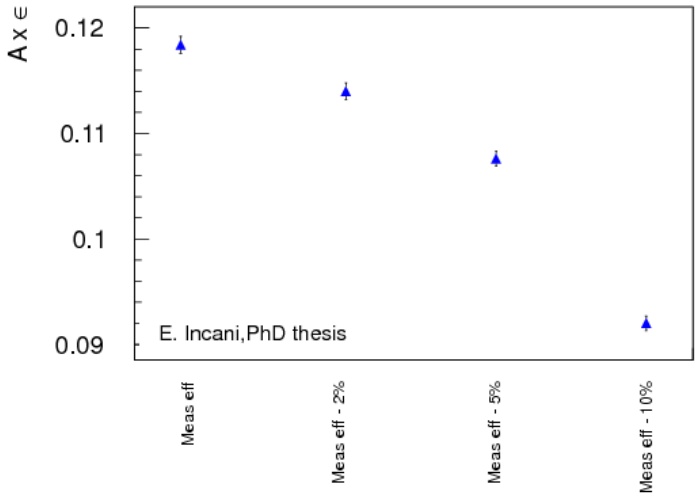

Figure 5.8: $A \times \epsilon$ in function of variation by a certain amount the efficiency of the trigger boards.

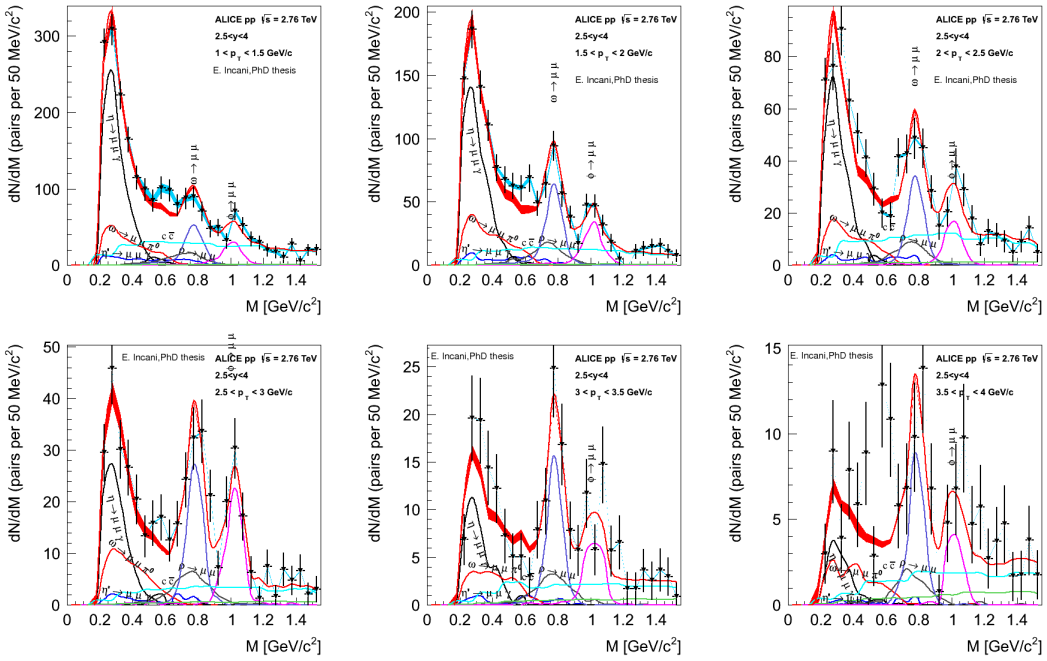

Figure 5.9: Fit to the mass spectrum after combinatorial background at 2.76 TeV in several p_T bins.

Plots of figure 5.10 show the raw (left) and acceptance×efficiency-corrected p_T distribution for the ϕ (right). The last one is fitted using the power-law function (Eq.4.6), and the parameters A and n are fixed to the values used in the AliGenMUONLMR generator, as described in Chapter 3.

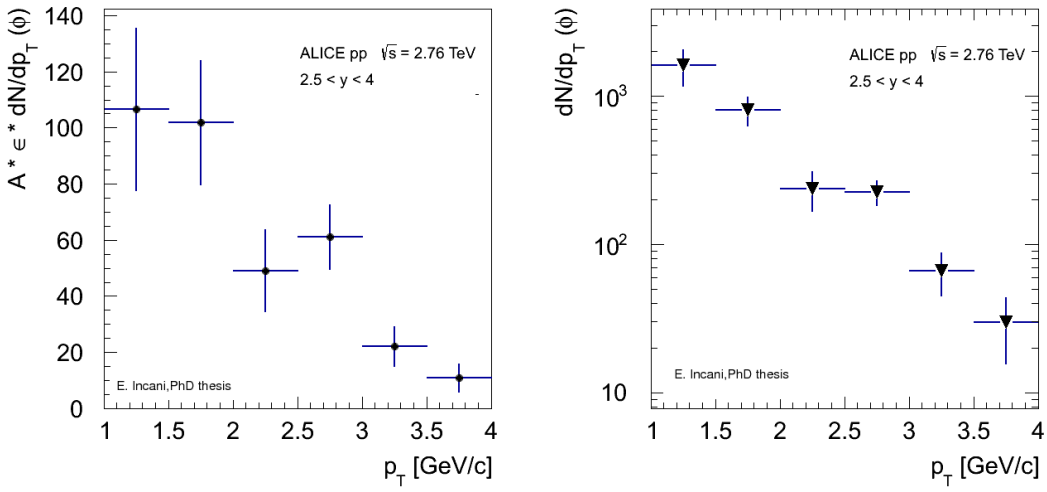

Figure 5.10: Raw p_T distribution for ϕ (left) and the acceptance×efficiency-corrected p_T distribution (right).

The rapidity distribution is obtained fitting the mass spectrum for each $y = 0.3$ interval in the p_T range covered by the analysis, as shown in Fig. 5.11.

Figure 5.12 shows on the left the raw rapidity distribution and on the right the acceptance×efficiency corrected rapidity distribution for the ϕ. The rapidity distribution is fitted using the function used in AliGenMUONLMR (Eq.4.12), and the parameters y_0 and σ_y are fixed at the values used in the generator.

5.5.2 Differential ϕ cross sections

The differential cross section $d^2\sigma_\phi/dydp_T$ as a function of p_T is shown in Fig. 5.13; the systematic uncertainties, described above, are indicated as orange boxes. For comparison the differential ϕ production cross section at 7 TeV is shown, this latter is slightly harder than the other one.

The differential cross section $d^2\sigma_\phi/dydp_T$ as a function of rapidity is shown in Fig. 5.14, the error bars represent the quadratic sum of the statistical and systematic

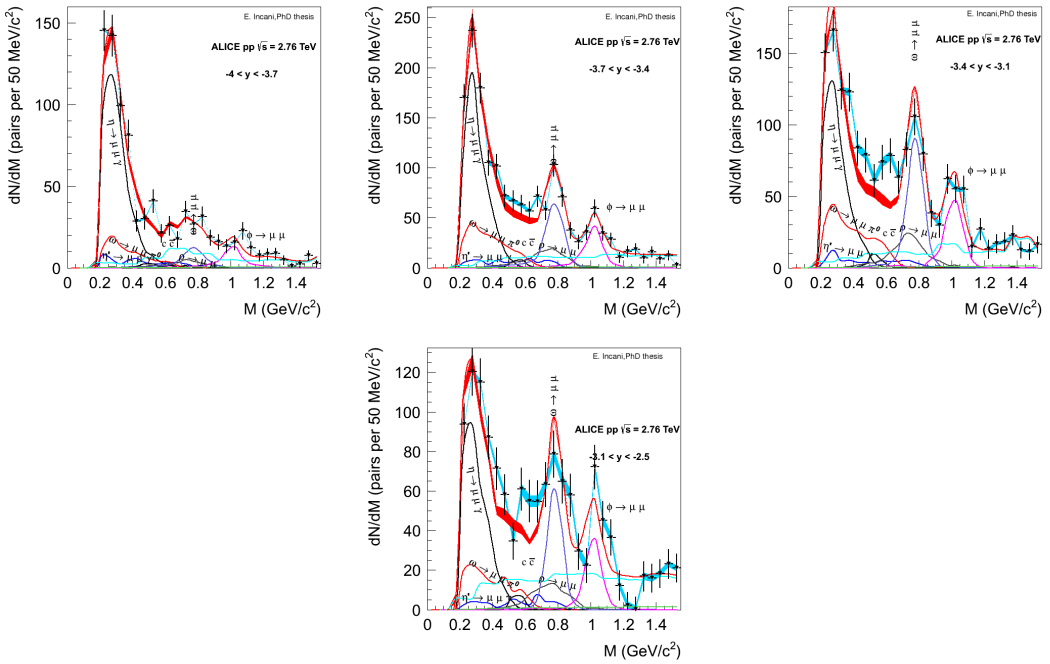

Figure 5.11: Fit to the mass spectrum after combinatorial background at 2.76 TeV in several y bins.

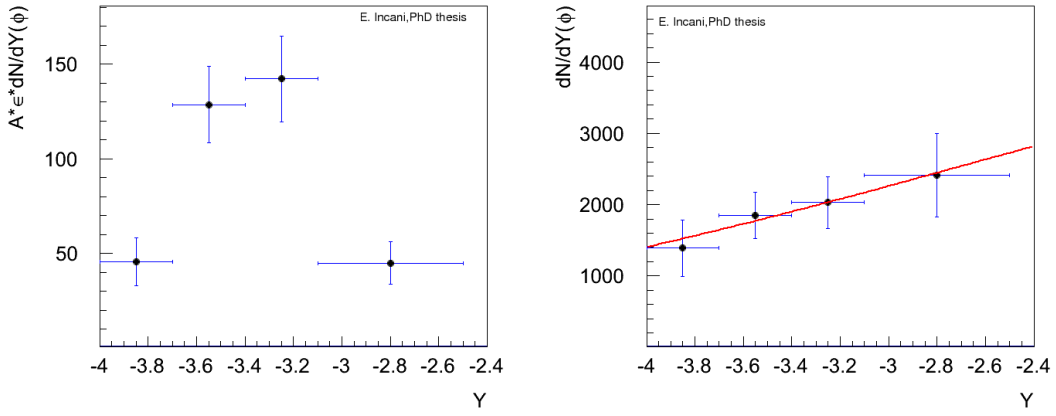

Figure 5.12: Raw rapidity distribution (left) and acceptance×efficiency-corrected rapidity distribution for ϕ (right).

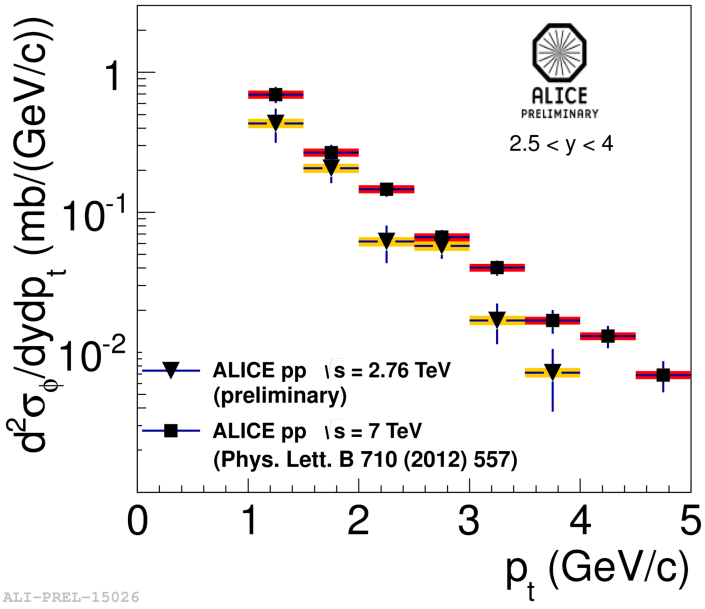

Figure 5.13: Differential ϕ production cross section $d^2\sigma_\phi/dydp_T$ for $2.5 < y < 4$. The error bars represent the quadratic sum of the statistical and systematic uncertainties, the orange boxes the point-to-point uncorrelated systematic uncertainty. On the right the result at 7 TeV is also shown for comparison (black squares).

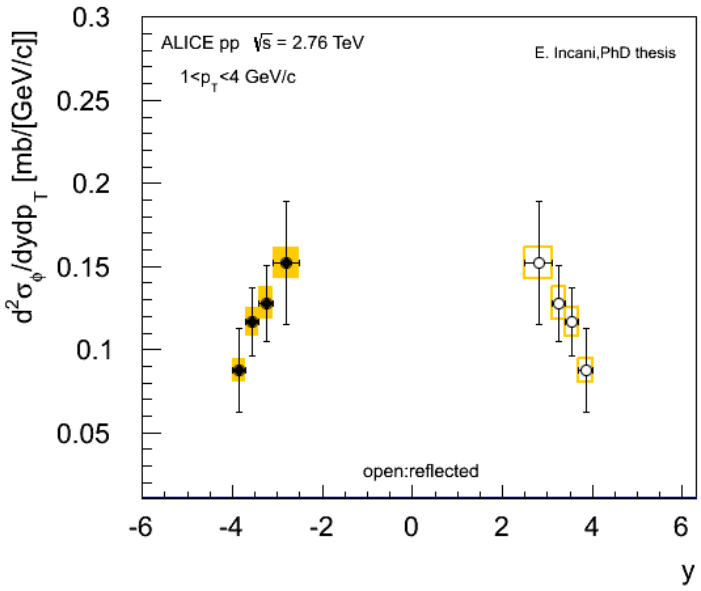

Figure 5.14: Differential ϕ production cross section $d^2\sigma_\phi/dydp_T$ for $1 < p_T < 4$ GeV/c. The error bars represent the quadratic sum of the statistical and systematic uncertainties, the orange boxes the point-to-point uncorrelated systematic uncertainty. The open symbols are the reflection points in the regions of positive rapidity.

uncertainties, the orange boxes the point-to-point uncorrelated systematic uncertainty. The open symbols are the reflection points in the region of positive rapidity.

5.6 pp as baseline for the heavy-ion data

In the ALICE experiment this short period of data collected at $\sqrt{s} = 2.76$ TeV is very important because it provides a reference for the PbPb data which were taken at the same $\sqrt{s}$ per A-A collision.

The p_T range of ϕ analysis in Pb-Pb is limited to $p_T > 2$ GeV/c, because of a higher trigger p_T threshold in that data taking. We have evaluated the ϕ cross section in pp collisions for $p_T > 2$ GeV/c. The number of resonances, obtained from the fit shown in the right panel of Fig. 5.5, is: $N_\phi = 155 \pm 22$, $N_{\rho+\omega} = 370 \pm 29$. The final value of the ϕ cross section is:

$$\sigma_\phi(p_T > 2GeV/c, 2.5 < y < 4) = 0.109 \pm 0.016(\text{stat}) \pm 0.008(\text{syst}).$$

From the same fit, it is possible to extract the ratio:

$$N_\phi/N_{\rho+\omega}(p_T > 2 \text{ GeV}/c, 2.5 < y < 4) = 0.430 \pm 0.078(\text{stat}) \pm 0.010(\text{syst})$$

and, taking the ratio $\sigma_\rho/\sigma_\omega$ from the measurement at 7 TeV, the ω cross section:

$$\sigma_\omega = (p_T > 2 \text{ GeV}/c, 2.5 < y < 4) = 0.685 \pm 0.053(\text{stat}) \pm 0.017(\text{syst})$$

5. LOW MASS VECTOR MESON ANALYSIS VIA DIMUON CHANNEL IN PP COLLISION AT $\sqrt{S} = 2.76$ TEV

6

Comparison with some theoretical models and other measurements

Contents

We have compared the data analysed in this thesis with two event generators: PYTHIA (in some commonly used tunes: Perugia-0, Perugia-11, ATLAS-CSC and D6T) and PHOJET, already described in Section 1.3.

In this chapter I will compare the results obtained in this thesis with these generators and other measurements.

6.1 Comparison of the data with some theoretical models

6.1.1 Comparison of the data at $\sqrt{s} = 7$ TeV with some theoretical models

In table 6.1 the ϕ cross section and the ratio $\frac{N_\phi}{N_{\rho+\omega}}$ measured in the range $1 < p_T < 5$ GeV/c, $2.5 < y < 4$, are compared with the models listed above. It can be seen that for the ϕ cross section Perugia-0 and Perugia-11 underestimate the measurement (by

Table 6.1: Measured ϕ cross section and ratio $\frac{N_\phi}{N_{\rho+\omega}}$ at $\sqrt{s} = 7$ TeV compared to the calculation from PYTHIA with several tunes and PHOJET in the range $1 < p_T < 5$ GeV/c, $2.5 < y < 4$

	σ_ϕ [mb]	$\frac{N_\phi}{N_{\rho+\omega}}$
ALICE $\mu\mu$ measurement	$0.940 \pm 0.084 \pm 0.076$	$0.416 \pm 0.032 \pm 0.004$
PYTHIA/Perugia-0	0.50	0.22
PYTHIA/Perugia-11	0.62	0.20
PYTHIA/ATLAS-CSC	0.91	0.35
PYTHIA/D6T	1.12	0.30
PHOJET	0.87	0.30

Table 6.2: Measured ratio $\sigma_\rho/\sigma_\omega$ and ω cross section at $\sqrt{s} = 7$ TeV compared to the calculation from PYTHIA with several tunes and PHOJET in the range $1 < p_T < 5$ GeV/c, $2.5 < y < 4$

	$\sigma_\rho/\sigma_\omega$	σ_ω (mb)
ALICE $\mu\mu$ measurement	$1.15 \pm 0.20 \pm 0.12$	$5.28 \pm 0.54 \pm 0.49$
PYTHIA/Perugia-0	1.03	5.60
PYTHIA/Perugia-11	1.03	7.81
PYTHIA/ATLAS-CSC	1.05	6.50
PYTHIA/D6T	1.04	9.15
PHOJET	1.08	6.89

about a factor of 2 and 1.5, respectively), while the others agree with the measurement within its error. On the other hand the ratio $\frac{N_\phi}{N_{\rho+\omega}}$ is underestimated by all models, only PYTHIA-ATLAS-CSC agrees within the uncertainty of the measurement.

The ratios $\sigma_\rho/\sigma_\omega$ predicted from the models are in agreement with our measurement, as shown in Table 6.2. The ω production cross section, calculated from this ratio is in agreement with the Perugia-0 tune, while the other PYTHIA tunes and PHOJET overestimate the ω cross section, as shown in the same table.

In Fig. 6.1 the ratio $\frac{N_\phi}{N_{\rho+\omega}}$ is plotted as a function of p_T. Perugia-0, Perugia-11 and D6T tunes systematically underestimate this ratio, while PHOJET correctly reproduces the data for $p_T > 3$ GeV/c, and ATLAS-CSC is in agreement with the measurement for $p_T > 1.5$ GeV/c.

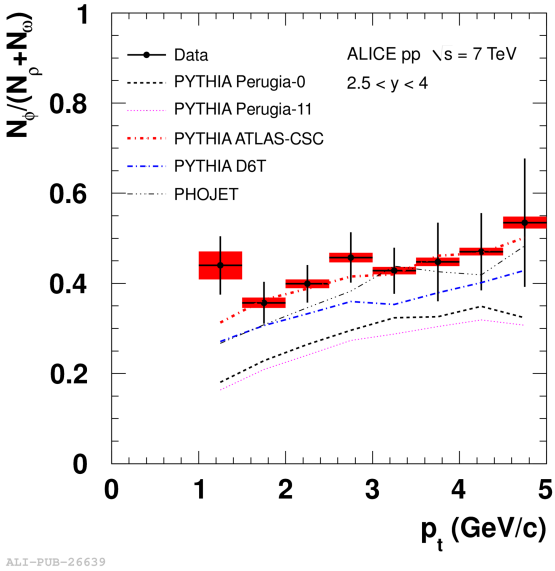

Figure 6.1: Ratio $N_\phi/(N_\rho + N_\omega)$ as a function of the dimuon transverse momentum.

In Fig. 6.2, $d^2\sigma_\phi/dp_T dy$ and $d^2\sigma_\omega/dp_T dy$, displayed as a function of p_T in the rapidity range of $2.5 < y < 4$, are compared with the models (top), while the bottom panels show the ratio between the measurements and the model predictions. In Fig. 6.3 the same quantities are plotted as a function of y in the range $1 < p_T < 5$ GeV/c.

From Figure 6.2 it can be seen that PYTHIA with ATLAS-CSC and D6T tunes reproduce the measured ϕ differential cross sections, while the others predict a slightly harder p_T spectrum. For the ω all the PYTHIA tunes reproduce the p_T slope, while PHOJET gives a slightly harder spectrum.

As for what concerns the differential cross sections as a function of rapidity, for the ϕ it is hard, with our data, to discriminate between the shapes provided by the models. Measurements at midrapidity, which will be discussed later, will allow to have a clearer picture. The shape of the ω differential cross section as a function of y is better reproduced by PYTHIA with ATLAS-CSC and Perugia-0 tunes, while D6T and PHOJET predict a slightly wider y distribution, and Perugia-11 a narrower one.

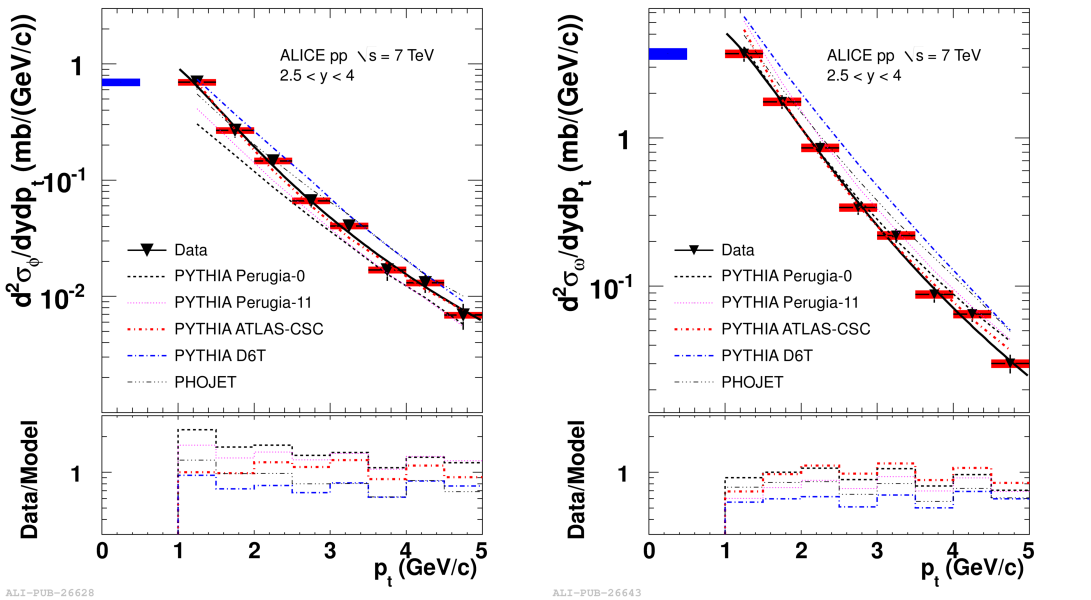

Figure 6.2: Left: Inclusive differential ϕ production cross section $\mathrm{d}^2\sigma_\phi/\mathrm{d}y\mathrm{d}p_T$ for $2.5 < y < 4$ compared with the Perugia-0, Perugia-11, ATLAS-CSC and D6T PYTHIA tunes and with PHOJET (top), and ratio between data and models (bottom). Right: same for the ω

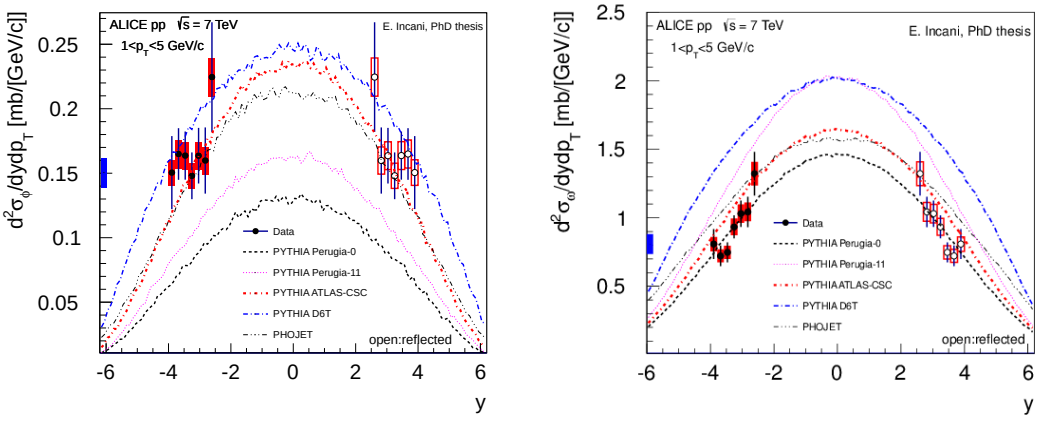

Figure 6.3: Inclusive differential ϕ (left) and ω (right) production cross sections for $1 < p_T < 5$ GeV/c as a function of y compared with the Perugia-0, Perugia-11, ATLAS-CSC and D6T PYTHIA tunes and with PHOJET. The open symbols are the reflection points in the regions of positive rapidity.

Table 6.3: Measured ϕ cross section at 2.76 TeV compared to the calculation from PYTHIA with several tunes and PHOJET in the range $1 < p_T < 4$ GeV/c, $2.5 < y < 4$

	σ_ϕ [mb]
ALICE $\mu\mu$ measurement	$0.573 \pm 0.065 \pm 0.044$
PYTHIA/Perugia-0	0.275
PYTHIA/Perugia-11	0.293
PYTHIA/ATLAS-CSC	0.464
PYTHIA/D6T	0.625
PHOJET	0.487

Table 6.4: Measured ϕ and ω cross sections at 2.76 TeV compared to the calculation from PYTHIA with several tunes and PHOJET in the range $p_T > 2$ GeV/c, $2.5 < y < 4$

	σ_ϕ [mb]	σ_ω [mb]
ALICE $\mu\mu$ measurement	$0.109 \pm 0.016 \pm 0.008$	$0.685 \pm 0.053 \pm 0.017$
PYTHIA/Perugia-0	0.067	0.601
PYTHIA/Perugia-11	0.064	0.625
PYTHIA/ATLAS-CSC	0.078	0.508
PYTHIA/D6T	0.123	0.863
PHOJET	0.112	0.826

6.1.2 Comparison of the data at $\sqrt{s} = 2.76$ TeV with some theoretical models

Also the data at 2.76 TeV were compared with the same commonly used models, for which the cross sections are written in Tables 6.3 and 6.4. In Table 6.3 the ϕ cross section measured and calculated in the range $1 < p_T < 4$ GeV/c and $2.5 < y < 4$ is listed, while in Table 6.4 the ϕ and ω cross sections measured in the range $p_T > 2$ GeV/c and $2.5 < y < 4$ are reported. For the ϕ, PHOJET and PYTHIA with ATLAS-CSC and D6T tunes reproduce σ_ϕ, while Perugia-0 and Perugia-11 underestimate the data in both cases, similarly to the 7 TeV analysis.

For the ω, at $p_T > 2$ GeV/c, Perugia and ATLAS-CSC tunes underestimate the data, while PHOJET and PYTHIA-D6T overestimate the ω production cross section as at 7 TeV.

The differential cross sections are reported in (Figure 6.4). Given the statistical accuracy of our measurement, it is not possible to discriminate between the shapes provided by the various models.

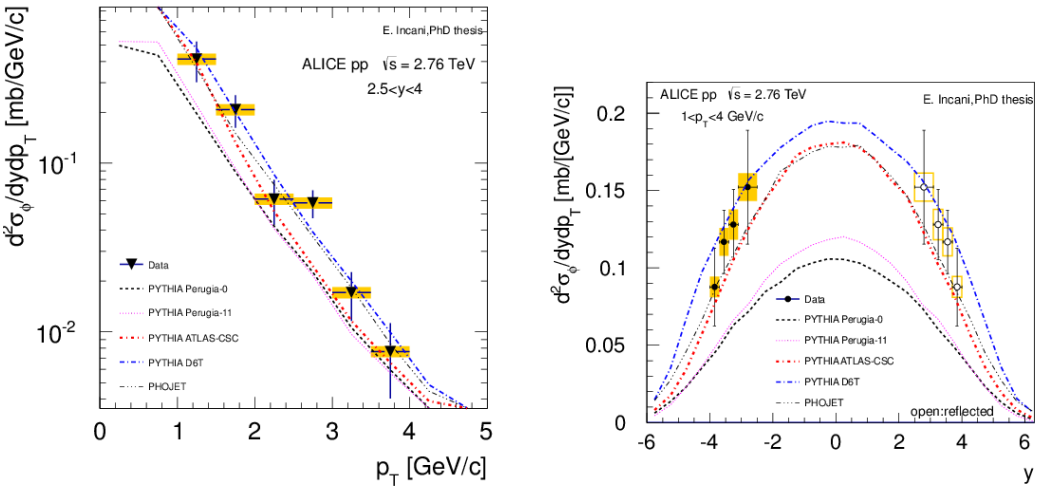

Figure 6.4: Inclusive differential ϕ cross sections as a function of p_T (left) and of y (right) compared with Perugia-0, Perugia-11, ATLAS-CSC and D6T PYTHIA tunes and with PHOJET. The open symbols are the reflection points in the regions of positive rapidity.

6.1.3 Summary of the comparisons

Finally we can summarize the results in Figure 6.5, where we have confronted our data with some models in the region $1 < p_T < 5$ GeV/c and $2.5 < y < 4$.

6.2 Other measurements

Other measurements of ϕ meson production in pp collisions at $\sqrt{s} = 7$ TeV have been executed by the LHCb experiment and by ALICE in the central-barrel (see Chapter 2).

The LHCb detector at the LHC has measured the cross section for inclusive ϕ meson production and the differential cross section as a function of p_T and rapidity in the region $0.6 < p_T < 5.0$ GeV/c and $2.44 < y < 4.06$. The cross section for inclusive ϕ production in this kinematic range is $\sigma(pp \to \phi X) = 1758 \pm 19(stat)^{+43}_{-14}(\text{syst}) \pm 182(\text{scale})\mu\text{b}$.

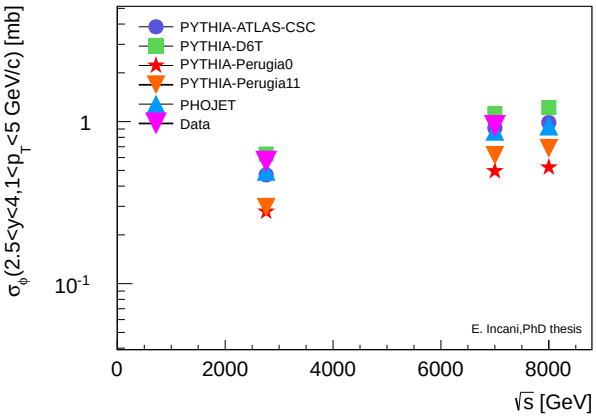

Figure 6.5: σ_ϕ measured with the ALICE data and calculated with different event generators in $1 < p_T < 5$ GeV/c and $2.5 < y < 4$.

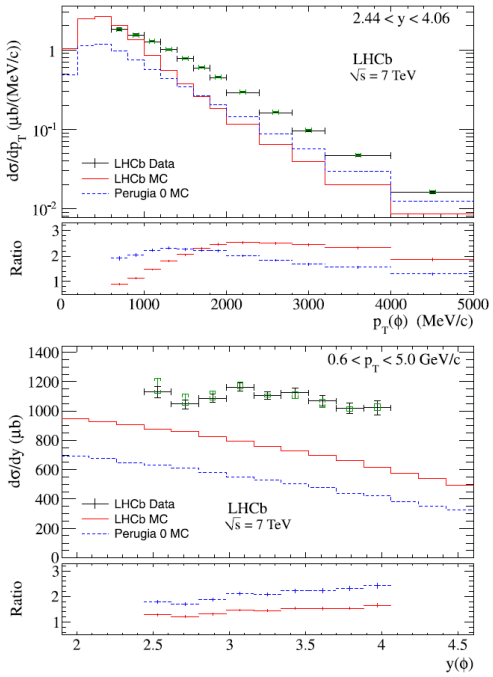

Figure 6.6: ϕ cross section as a function of p_T (top) and y (bottom), measured with data (points), and compared to the LHCb default MC tune (solid line) and Perugia-0 tune (dashed line).

In Fig. 6.6 it is shown the differential ϕ production cross section measured as a function of p_T (points), and compared to the LHCb default MC tune (solid line) and

Perugia 0 tune (dashed line) [85]. The simulations underestimate the ϕ cross section by a factor 1.43 ± 0.15 (LHCb MC) and 2.06 ± 0.22 (Perugia-0) and the shapes of the p_T and y spectra differ between the data and the simulation.

The ALICE experiment has measured the transverse momentum spectra $d^2N/dydp_T$ at midrapidity $|y| < 0.5$ in the range $0.4 < p_T < 6$ GeV/c using the $\phi \to K^+K^-$ channel. The p_T spectrum is well described by the Lévy-Tsallis function and the comparison with the models shows the same trend observed in our data: the ϕ spectrum is rather well reproduced by ATLAS-CSC and D6T tunes, while Perugia-0 and Perugia-11 tunes underestimate the data, as it is shown in Fig. 6.7 [37].

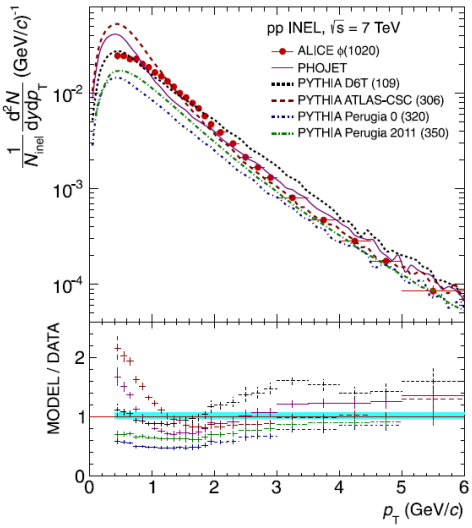

Figure 6.7: Comparison of the ϕ p_T spectrum with PHOJET and PYTHIA tunes D6T, ATLAS-CSC, Perugia-0 and Perugia-11.

Our results are compared to the measurements of $\phi \to K^+K^-$ for $2.44 < y < 4.06$ by the LHCb Collaboration and of $\phi \to K^+K^-$ for $|y| < 0.5$ by ALICE in the central barrel. The observed shapes of the p_T distributions (see Fig. 6.8) are similar, but the ALICE $\phi \to K^+K^-$ measurement is higher by about 30%. A study executed using different PYTHIA tunes [37] shows a variation of the ϕ yield by 20%-50% between forward ($2.5 < y < 4$) and mid-central ($|y| < 0.5$) rapidities.

In order to compare with our integrated cross section result, the differential cross section measurement by LHCb was integrated for $1 < p_T < 5$ GeV/c and scaled by a small correction factor, obtained from PYTHIA (Perugia-0), to account for the slight

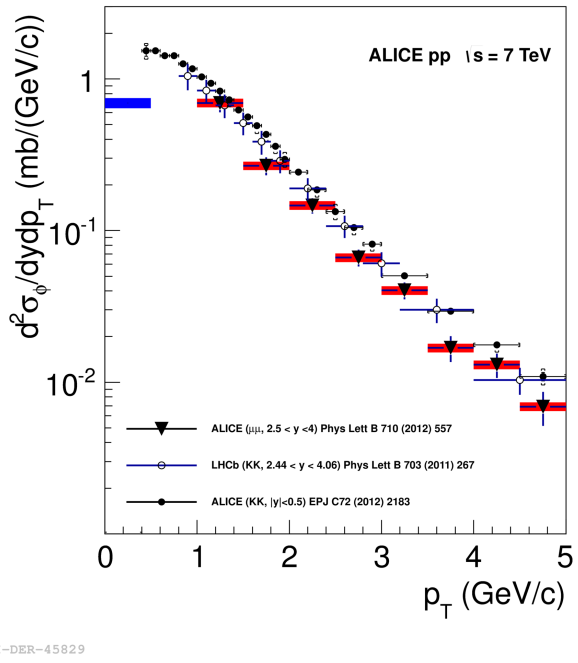

Figure 6.8: Comparison of the ϕ p_T spectrum with ALICE in the central barrel and LHCb.

difference in rapidity acceptance. The result is $\sigma_\phi = 1.07 \pm 0.15(\text{stat.} + \text{syst.})$ mb. If the statistical errors and the part of the systematic uncertainty, which is not correlated among the two experiments, are properly taken into account, the two measurements are in agreement. The agreement is more visible in $d^2\sigma_\phi/dydp_T$ as a function of y (see Fig. 6.9). In this figure the distribution of ϕ cross section measured by LHCb is displayed only in the range $1 < p_T < 5$ GeV/c: ours and the LHCb measurements look flatter than the trend predicted by models; on the other hand, the ratio between the ϕ cross section in the forward and central rapidity is reproduced by the event generators.

6.3 Differential ϕ cross section as a function of p_T and rapidity combining all data

In the previous section we have compared our results with other measurements: the ϕ cross section measured by LHCb in similar rapidity range and with a more extended coverage at low p_T (down to 0.6 GeV/c), and the ϕ cross section measured by ALICE

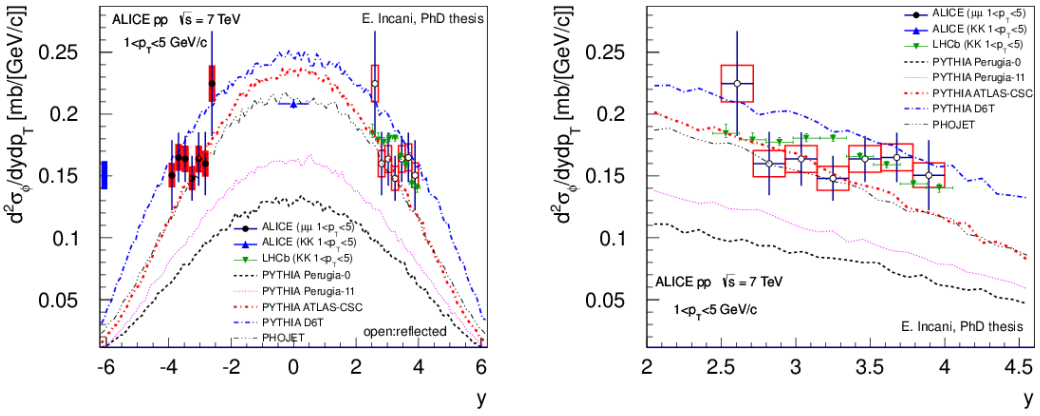

Figure 6.9: Comparison of the ϕ y spectrum with ALICE in the central barrel, LHCb, PHOJET and PYTHIA tunes D6T, ATLAS-CSC, Perugia-0 and Perugia-11.

in central rapidity. In the following I will show how we have combined these results with ours to obtain more precise p_T and rapidity distributions. These results are useful to further tune AliGenMUONLMR at 7 TeV.

6.3.1 Differential ϕ cross section as a function of p_T

To obtain a more precise differential ϕ cross section as a function of p_T, we performed a combined fit to our p_T-differential cross section together with the LHCb one, using two functions, a power-law:

$$\frac{dN}{dp_T} \propto \frac{p_T}{\left[1 + \left(\frac{p_T}{A}\right)^2\right]^n} \tag{6.1}$$

and a Lévi-Tsallis function:

$$\frac{dN}{dp_T} \propto \frac{(n-1)(n-2)}{nA[nA + m(n-2)]} p_T \left(1 + \frac{m_T - m}{nA}\right)^{-n}. \tag{6.2}$$

The result is shown in Figure 6.10 and fit parameters and their reduced χ^2 are listed in Table 6.5.

6.3.2 Differential ϕ cross section as a function of rapidity

We performed the same exercise as a function of rapidity using a similar method, combining our data, the LHCb and the ALICE ones in central rapidity.

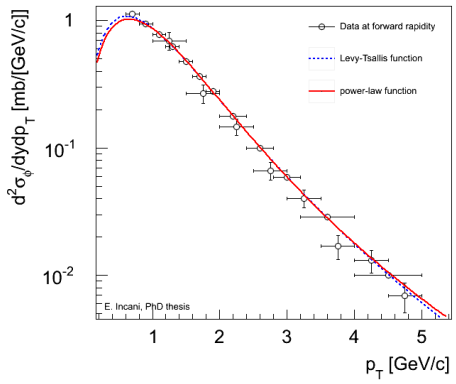

Figure 6.10: $d^2\sigma_\phi/dydp_T$ for $2.5 < y < 4$ as a function of p_T obtained from our ($2.5 < y < 4$) and LHCb ($2.44 < y < 4.06$) data.

Table 6.5: Fit parameters and their reduced χ^2 evaluated with the fit functions

	power-law function	Lévi-Tsallis function
A	7.91 ± 0.30	1.51 ± 0.03
n	3.26 ± 0.07	3.07 ± 0.05
χ^2/NDF	0.91	1.14

One function used to fit the data is:

$$\text{function1} = \frac{dN}{dy} \propto \frac{1}{e^{\sigma_y \cdot y^2} + e^{-\sigma_y \cdot y^2}}, \tag{6.3}$$

that reasonably reproduces the rapidity distributions obtained with the models, as we can see in Figure 6.11, where we have fitted the ϕ cross section as a function of rapidity evaluated between 1 and 5 GeV/c of p_T by PYTHIA Perugia-0. We observed similar agreement with the other generators used in this analysis.

Another one is the function used in AliGenMUONLMR:

$$\text{function2} = \frac{dN}{dy} = \begin{cases} \text{const.} & \text{for } |y| < y_0 \\ e^{-\frac{1}{2}\frac{(|y|-y_0)^2}{\sigma_y^2}} & \text{for } |y| > y_0 \end{cases} \tag{6.4}$$

The last test function that was used is a gaussian centered at $y = 0$.

The fits are shown in Figure 6.12 and fit parameters and their reduced χ^2 are listed in Table 6.6.

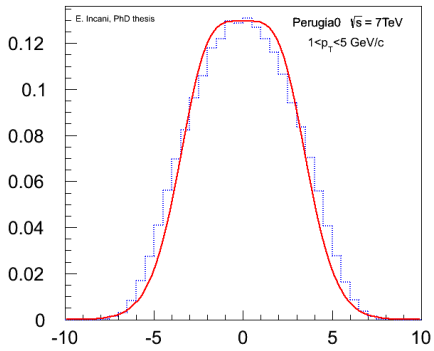

Figure 6.11: $d^2\sigma_\phi/dydp_T$ for $1 < p_T < 5$ GeV/c as a function of rapidity evaluated by PYTHIA Perugia-0.

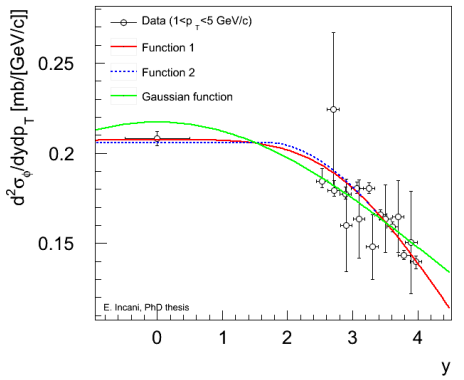

Figure 6.12: $d^2\sigma_\phi/dydp_T$ for $2.5 < y < 4$ as a function of rapidity obtained from our, the ALICE data central-barrel and LHCb data.

Table 6.6: Fit parameters and their reduced χ^2 evaluated with the fit functions

	function 1	function 2	Gaussian function
y_0		1.66 ± 0.24	0
σ_y	$(5.97 \pm 0.19)10^{-2}$	2.67 ± 0.26	4.56 ± 0.13
χ^2/NDF	1.77	2.11	3.73

Summary & Outlook

ϕ and ω meson production was measured with the data collected by the ALICE experiment in proton-proton collisions at $\sqrt{s} = 7$ and $\sqrt{s} = 2.76$ TeV via dimuon channel.

For the analysis at 7 TeV we have evaluated:

1. the ratio $N_\phi/(N_\rho+N_\omega) = 0.416\pm0.032$ (stat)±0.004 (syst) for $1 < p_T < 5$ GeV/c, $2.5 < y < 4$. The value of this ratio as a function of p_T is constant;

2. the inclusive ϕ cross section $\sigma_\phi(1 < p_T < 5 \text{ GeV}/c,\ 2.5 < y < 4) = 0.940 \pm 0.084(\text{stat}) \pm 0.076(\text{syst})$ mb, and the differential cross section as a function of p_T and rapidity;

3. the ratio $\sigma_\rho/\sigma_\omega = 1.15 \pm 0.20(\text{stat.}) \pm 0.12(\text{syst.})$

4. the inclusive ω cross section $\sigma_\omega(1 < p_T < 5 \text{ GeV}/c,\ 2.5 < y < 4) = 5.28 \pm 0.54(\text{stat}) \pm 0.49(\text{syst})$ mb, and the differential cross section as a function of p_T and rapidity.

We have compared the ϕ cross section to the measurement of $\phi \to K^+K^-$ for $2.44 < y < 4.06$ by the LHCb Collaboration, observing a good agreement between the two measurements. We have also compared our result to the one in $\phi \to K^+K^-$ for $|y| < 0.5$ by ALICE in the central barrel. The ratio between the ϕ cross section in the forward and central rapidity is reproduced by the models taken into account.

For the data sample at 2.76 TeV, because of the limits in statistics, we have evaluated only:

1. $N_\phi/N_{\rho+\omega}(p_T > 2 \text{ GeV}/c, 2.5 < y < 4) = 0.430 \pm 0.078(\text{stat}) \pm 0.010(\text{syst})$ ratio;

2. the ϕ cross section $\sigma_\phi(1 < p_T < 4GeV/c, 2.5 < y < 4) = 0.573 \pm 0.065(\text{stat}) \pm 0.044(\text{syst})$ and $\sigma_\phi(p_T > 2GeV/c, 2.5 < y < 4) = 0.109\pm0.016(\text{stat})\pm0.008(\text{syst})$;

3. the ω integrated cross section $\sigma_\omega = (p_T > 2 \text{ GeV}/c, 2.5 < y < 4) = 0.685 \pm 0.053(\text{stat}) \pm 0.017(\text{syst})$.

In both analyses we have compared the data with two event generators: PYTHIA (in some commonly used tunes: Perugia-0, Perugia-11, ATLAS-CSC and D6T) and PHOJET. PHOJET and PYTHIA with the tunes ATLAS-CSC and D6T agree with the ϕ cross sections measured at 7 TeV and 2.76 TeV, whereas PYTHIA Perugia-0 and Perugia-11 underestimate both cross sections. On the other hand, the ω cross section is in agreement with the Perugia-0 tune at 7 TeV, while the other PYHTIA tunes and PHOJET overestimate the measurement. At 2.76 TeV, and in a different p_T range, the Perugia and ATLAS-CSC tunes underestimate the ω cross section, while PHOJET and PYTHIA-D6T overestimate the ω production cross section as at 7 TeV.

The next step of the ϕ and ω production analysis in proton-proton collisions will be to study the last data collected by the ALICE experiment at 8 TeV. As for the study of QGP, it will be to study the data collected in Pb-Pb collisions in 2011 (analysis already started) and the ones in p-Pb collisions (running).

Appendix A: Run list 7 TeV

Runs used had been tagged as "good"run by the DQA experts (i.e. the data acquisition was successful and that the running conditions were stable and under control) and they had passed some quality checks (Quality Assurance - QA) (i.e. the number of cluster associated to a tracking track, the number of tracks per muon trigger, etc.).

- **LHC10b**:
  117222, 117220, 117120, 117118, 117116, 117112, 117109, 117099, 117098, 117092, 117082, 117077, 117065, 117063, 117060, 117059, 117054, 117053, 117052, 117050, 117048, 116684, 116681, 116645, 116644, 116643, 116611, 116609, 116574, 116562, 116561, 116401, 116288, 116204, 116203, 116198, 116197, 116134, 116123, 116118, 116102, 116081, 116079, 115892, 115890, 115889, 115887, 115882, 115881, 115880, 115521, 115516, 115514, 115414, 115393, 115345, 115335, 115328, 115325, 115322, 115318, 115315, 115310, 115193, 114931, 114930, 114920, 114919, 114918

- **LHC10c**:
  120824, 120823, 120822, 120821, 120820, 120741, 120671, 120617, 120616, 120505, 120504, 120503, 120079, 120076, 120073, 120072, 120069, 120067, 119971, 119969, 119965, 119961, 119959, 119952, 119948, 119926, 119924, 119923, 119909, 119907, 119904, 119862, 119859, 119856, 119853, 119849, 119845, 119844, 119842, 119841, 119163, 119161, 119159

- **LHC10d**:
  126424, 126422, 126409, 126408, 126407, 126406, 126405, 126404, 126403, 126359, 126351, 126350, 126284, 126283, 126177, 126168, 126162, 126097, 126088, 126087, 126081, 126078, 126073, 126008, 126007, 126004, 125855, 125848, 125847, 125844, 125843, 125842, 125632, 125630, 125628, 125296, 125292, 125186, 125156, 125139, 125134, 125133, 125131, 125101, 125100, 125097, 125085, 125083, 124608, 124607, 124606, 124605, 124604, 124603, 124600, 124388, 124385, 124383, 124381, 124380, 124378, 124374, 124371, 124367, 124362, 124360, 124359, 124358, 124355, 124187, 124186, 124183, 122375, 122374

- **LHC10e**:
  130850, 130848, 130847, 130844, 130842, 130840, 130804, 130803, 130802, 130798,

130795, 130793, 130704, 130623, 130621, 130620, 130519, 130517, 130481, 130480, 130375, 130369, 130360, 130358, 130354, 130348, 130343, 130342, 130179, 130178, 130149, 129962, 129961, 129960, 129959, 129738, 129736, 129735, 129734, 129726, 129725, 129723, 129667, 129666, 129654, 129639, 129587, 129586, 129540, 129536, 129528, 129527, 129525, 129524, 129523, 129521, 129520, 129519, 129516, 129515, 129514, 129513, 129512, 129508, 129042, 128913, 128912, 128911, 128910, 128855, 128853, 128850, 128849, 128819, 128778, 128777, 128678, 128677, 128621, 128596, 128594, 128592, 128590, 128582, 128507, 128506, 128505, 128504, 128503, 128498, 128495, 128494, 128263, 128260, 128257, 128192, 128191, 128189, 128186, 128185, 128182, 128180, 128175, 127942, 127941, 127940, 127935, 127933, 127932, 127931, 127930, 127819, 127817, 127815, 127814

- **LHC10f** (high luminosity part):
  134919, 134914, 134905, 134841, 134685, 134679, 134666, 134497

- **LHC10f** (low luminosity part):
  134690, 134304, 134204, 133414, 133010, 133006, 133327, 133330, 133419, 133563, 133800, 133924, 133969, 133985, 134094, 134198

For the ϕ cross section calculation we did not use the runs from run 125083 to 125296 of the LHC10d period, because of a reduced efficiency of a tracking chamber (7-left), while the runs 134919, 134914, 134905, 134841, 134497 of the LHC10f period were rejected because the information on the minimum bias trigger was missing.

Appendix B: Run list 2.76 TeV

LHC11a:

146860 146859 146858 146856 146824 146817 146807 146806 146805
146804 146803 146802 146801 146748 146747 146746 146689 146688

Appendix B: Run list 2.76 TeV

Al termine del periodo di lavoro che mi ha portato alla stesura della tesi di dottorato vorrei ringraziare le persone che mi sono state vicine.

Desidero ringraziare il Dott. Alessandro De Falco, relatore di questa tesi, che mi ha aiutato e sostenuto con la sua competenza scientifica, la sua esperienza e la sua immensa pazienza aiutandomi nelle problematiche della ricerca e determinando una sempre maggiore autonomia lavorativa.

Il Prof. Gianluca Usai, relatore della tesi specialistica e correlatore in questa tesi, che mi ha permesso di lavorare all'interno di un gruppo di alto livello come il gruppo 3 di Cagliari ed è stato fondamentale per una parte importante di questa analisi.

Un particolare grazie a Ester, l'altra dottoranda del gruppo, che ha collaborato con simpatia e disponibilità a questo lavoro.

Il Prof. Piero Del Riccio, che con i suoi consigli è stato fondamentale per la determinazione della sezione d'urto della ω.

Un ringraziamento ai compagni di ufficio che si sono alternati in questi tre anni: Giovanna Rosa (che ha condiviso con me i tre anni di dottorato con tutti i problemi burocratici annessi), Cristina, Danilo, Mahsa, Alberto e, anche se non hanno la postazione nel nostro ufficio ma ci passano gran parte del loro tempo, Mauro, Carlo e l'ultima arrivata Cristina, per essermi stati vicini sia nei momenti difficili, sia nei momenti felici: sono stati per me più veri amici che semplici colleghi.

Devo ringraziare Michi, la persona che più mi è stata vicino e mi ha sempre incoraggiato in questo periodo di dottorato, mia cugina Sara che mi ha suggerito la bellissima epigrafe di questa tesi e i miei genitori che mi hanno sempre sostenuto e incoraggiato in questa avventura.

Bibliography

[1] Satz, Helmut . *Extreme States of Matter in Strong Interaction Physics*. Springer, 2012. 4, 7

[2] T. Banks and A. Casher. Chiral symmetry breaking in confining theories. *Nuclear Physics B*, 169(12):103 – 125, 1980. 6

[3] Abelev et al. (ALICE Collaboration). J/ψ Suppression at Forward Rapidity in Pb-Pb Collisions at $\sqrt{s_{\rm NN}} = 2.76$ TeV. *Phys. Rev. Lett.*, 109:072301, Aug 2012. 7

[4] Abelev et al. (ALICE Collaboration). Production of Muons from Heavy Flavor Decays at Forward Rapidity in *pp* and Pb-Pb Collisions at $\sqrt{s_{NN}}$=2.76 TeV. *Phys. Rev. Lett.*, 109:112301, Sep 2012. 7

[5] Aamodt et al. (ALICE Collaboration). Particle-Yield Modification in Jetlike Azimuthal Dihadron Correlations in Pb-Pb Collisions at $\sqrt{s_{\rm NN}} = 2.76$ TeV. *Phys. Rev. Lett.*, 108:092301, Mar 2012. 7

[6] Robert D. Pisarski. Phenomenology of the chiral phase transition. *Physics Letters B*, 110(2):155 – 158, 1982. 8

[7] R. Rapp, J. Wambach. Chiral Symmetry Restoration and Dileptons in Relativistic Heavy-Ion Collisions. *Adv.Nucl.Phys. 25 (2000) 1*, 25():1, 2000.

[8] G.E. Brown and Mannque Rho. On the manifestation of chiral symmetry in nuclei and dense nuclear matter. *Physics Reports*, 363(2):85 – 171, 2002. 8

[9] S. Okubo. ϕ-meson and unitary symmetry model. *Physics Letters*, 5(2):165 – 168, 1963. 8

[10] G. Zweig. An SU(3) Model for Strong Interaction Symmetry and its Breaking. *CERN Report Nos. TH-401 and TH-412*, :, 1964.

[11] Jugoro Iizuka and Kunihiko Okada and Okiyasu Shito. Systematics and Phenomenology of Boson Mass Levels. III. *Progress of Theoretical Physics*, 35(6):1061–1073, 1966. 8

[12] Shor, Asher. ϕ-Meson Production as a Probe of the Quark-Gluon Plasma. *Phys. Rev. Lett.*, 54:1122–1125, Mar 1985. 8

[13] Rafelski, Johann and Müller, Berndt. Strangeness Production in the Quark-Gluon Plasma. *Phys. Rev. Lett.*, 48:1066–1069, 1982. 8

[14] Johann Rafelski. Strangeness production in the quark gluon plasma. *Nuclear Physics A*, 418(0):215 – 235, 1984. .

[15] M. Jacob and J. Tran Thanh Van. Quark matter formation and heavy ion collisions: A general review and status report. *Physics Reports*, 88(5):321 – 413, 1982. .

[16] P. Koch and J. Rafelski. Time evolution of strange-particle densities in hot hadronic matter. *Nuclear Physics A*, 444(4):678 – 691, 1985.

[17] Baltz, A. J. and Dover, C. Quark model of ϕ" coalescence from kaons in heavy-ion reactions,. *Phys. Rev. C*, 53:362–366, Jan 1996.

[18] H. Sorge and M. Berenguer and H. Stcker and W. Greiner. Colour rope formation and strange baryon production in ultrarelativistic heavy ion collisions. *Physics Letters B*, 289(12):6 – 11, 1992. 8

[19] Kevin Haglin. Collision rates for ρ-, ω- and ϕ-mesons at nonzero temperature. *Nuclear Physics A*, 584(4):719 – 736, 1995. 8

[20] Smith, Wade and Haglin, Kevin L. Collision broadening of the ϕ meson in baryon rich hadronic matter. *Phys. Rev. C*, 57:1449–1453, Mar 1998.

[21] Ko, Che Ming and Seibert, David. What can we learn from a second ϕ meson peak in ultrarelativistic nuclear collisions? *Phys. Rev. C*, 49:2198–2202, Apr 1994. 8

[22] M. Asakawa and C.M. Ko. ϕ meson mass in hot and dense matter. *Nuclear Physics A*, 572(34):732 – 748, 1994. 8

[23] Chungsik Song. Effective mass of phi mesons at finite temperature. *Physics Letters B*, 388(1):141 – 146, 1996. 8

[24] M. Asakawa and C.M. Ko. Seeing the QCD phase transition with ϕ mesons. *Physics Letters B*, 322(12):33 – 37, 1994. 8

[25] V. Friese (NA49 Collaboration). Production of strange resonances in C+C and Pb+Pb collisions at 158 AGeV. *Nuclear Physics A*, 698(14):487 – 490, 2002. 9

[26] B. Alessandro and all. (NA50 Collaboration). ϕ production in PbPb collisions at 158 GeV/c per nucleon incident momentum. *Physics Letters B*, 555(34):147 – 155, 2003. 9

[27] E.V. Shuryak. What have we learned and want to learn from heavy ion collisions at CERN SPS? *Nuclear Physics A*, 661(14):119 – 129, 1999. 9

[28] Subrata Pal, C.M. Ko, and Zi wei Lin. Phi meson production in relativistic heavy ion collisions. *Nuclear Physics A*, 707(34):525 – 539, 2002. 9

[29] J. Milošević and all. (CERES Collaboration). Strange particle production and elliptic flow from CERES. *Journal of Physics G: Nuclear and Particle Physics*, 32(12):S97, 2006. 9, 62

[30] R. Arnaldi at all. (NA60 Collaboration). A comparative measurement of and in InIn collisions at the CERN SPS. *Physics Letters B*, 699(5):325 – 329, 2011. 9

[31] Abelev et all. (STAR Collaboration) . Energy and system size dependence of ϕ meson production in Cu+Cu and Au+Au collisions. *Phys.Lett.*, B673:183–191, 2009. 13

[32] Adare et all. (PHENIX Collaboration). Nuclear modification factors of ϕ mesons in $d + \mathbf{Au}$, $\mathbf{Cu} + \mathbf{Cu}$, and $\mathbf{Au} + \mathbf{Au}$ collisions at $\sqrt{s_{NN}} = 200$ **GeV**. *Phys. Rev. C*, 83:024909, Feb 2011. 13

[33] Subhash (ALICE Collaboration) Singha. Strange hadron and resonance production in Pb-Pb collisions at $\sqrt{s_{NN}} = 2.76$ TeV with ALICE experiment at LHC. 2012. 14

[34] S.V. Afanasiev and all. (NA49 Collaboration). Production of ϕ-mesons in p+p, p+Pb and central Pb+Pb collisions at Ebeam=158 AGeV. *Physics Letters B*, 491(12):59 – 66, 2000. 14

[35] Abelev et all. (STAR Collaboration). Measurements of ϕ meson production in relativistic heavy-ion collisions at the BNL Relativistic Heavy Ion Collider (RHIC). *Phys. Rev. C*, 79:064903, Jun 2009. 14

[36] A. Adare and others (PHENIX Collaboration). Identified charged hadron production in $p + p$ collisions at $\sqrt{s} = 200$ and 62.4 GeV. *Phys.Rev.*, C83:064903, 2011. 14

[37] Abelev and others (ALICE Collaboration). Production of $k(892)^0$ and $\phi(1020)$ in pp collisions at $\sqrt{s} = 7$ TeV. *The European Physical Journal C*, 72:1–17, 2012. 14, 67, 104

[38] M. L. Mangano, T. J. Stelzer. Tools for the simulation of hard hadronic collisions. *Annual Review of Nuclear and Particle Science*, 55:555–588, 2005. 16

[39] Sjöstrand, Torbjorn and Mrenna, Stephen and Skands, Peter Z. PYTHIA 6.4 Physics and Manual. *JHEP*, 0605:026, 2006. 16

[40] Skands, Peter Z. The Perugia Tunes. pages 284–297, 2009. 16

[41] Peter Zeiler Skands. Tuning Monte Carlo Generators: The Perugia Tunes. *Phys.Rev.*, D82:074018, 2010. 16

[42] C. Buttar et al. Simulations of minimum bias events and the underlyng event, MC tuning and prediction for the LHC. *Acta Phys. Pol. B*, 35:433, 2004. 16

[43] Arthur Moraes (ATLAS collaboration). Modeling the underlying event: generating predictions for the LHC. *ATLAS Note*, ATL-COM-PHYS-2009-119:, 2009. 16

[44] R. Field. . *Acta Phys. Pol. B*, 39:2611, 2008. 16

[45] Michael G. Albrow et al. Tevatron-for-LHC Report of the QCD Working Group. 2006. 16

[46] R. Engel. . *Z. Phys. C*, 66:203, 1995. 16

[47] Engel, R. and Ranft, J. Hadronic photon-photon interactions at high energies. *Phys. Rev. D*, 54:4244–4262, Oct 1996. 16

[48] K. Aamodt et al. (ALICE Collaboration). The ALICE experiment at the CERN LHC. *Journal of Instrumentation*, 3(08):S08002, 2008. 21

[49] Evans, Lyndon Bryant and Philip. LHC Machine. *JINST*, 3:S08001, 2008. 22

[50] Aad, G. and others (ATLAS Collaboration). The ATLAS Experiment at the CERN Large Hadron Collider. *JINST*, 3:S08003, 2008. 24

[51] G. Aad et all. (ATLAS Collaboration). Observation of a new particle in the search for the standard model higgs boson with the atlas detector at the lhc. *Physics Letters B*, 716(1):1 – 29, 2012. 24

[52] Peter Steinberg and others (ATLAS Collaboration). Recent heavy-ion results with the ATLAS detector at the LHC. *Journal of Physics G: Nuclear and Particle Physics*, 38(12):124004, 2011. 24

[53] S. Chatrchyan and others (CMS Collaboration). The CMS experiment at the CERN LHC. *JINST*, 3:S08004, 2008. 24

[54] (CMS Collaboration) S. Chatrchyan et all. Observation of a new boson at a mass of 125 GeV with the CMS experiment at the LHC. *Physics Letters B*, 716(1):30 – 61, 2012. 24

[55] Bolek Wyslouch and all. (CMS Collaboration). Overview of experimental results in PbPb collisions at $\sqrt{s_{\mathrm{NN}}} = 2.76$ TeV by the CMS Collaboration. *Journal of Physics G: Nuclear and Particle Physics*, 38(12):124005, 2011. 24

[56] A Augusto Alves Jr and others (LHCb Collaboration). The LHCb Detector at the LHC. *Journal of Instrumentation*, 3(08):S08005, 2008. 25

[57] M. (ALICE collaboration) Floris. Charged particle production in Pb-Pb collisions at the LHC with the ALICE detector. 2012. 25

[58] M Gallio, W Klempt, L Leistam, J De Groot, and Jrgen Schkraft. *ALICE Zero-Degree Calorimeter (ZDC): Technical Design Report.* Technical Design Report ALICE. CERN, Geneva, 1999. 35

[59] L. Aphecetche et al. ALICE Internal Note ALICE-INT-2009-044. 37

[60] K. Nakamura. Review of particle physics. *J. Phys. G37:075021, 2010.* 39, 40, 62

[61] L.G. Landsberg. Electromagnetic decays of light mesons. *Physics Reports*, 128(6):301 – 376, 1985. 39, 48

[62] Antonio Uras. Low Mass Dimuon Production in p-A Collisions at 400 GeV/c with the NA60 Detector. *Università degli Studi di Cagliari, 2011, PhD Thesis.* 40, 48, 62

[63] F. Klingl, Norbert Kaiser, and W. Weise. Effective Lagrangian approach to vector mesons, their structure and decays. *Z.Phys.*, A356:193–206, 1996. 40

[64] I. Abt et al. (HERA-B Collaboration). K^0 and Phi meson production in proton nucleus interactions at $\sqrt{s} = 41.6$ GeV. *Eur. Phys. J.*, C 50:315, 2007. 42

[65] K. Reygers (for the ALICE Collaboration). J. Phys. G38 (2011) 124076. 43

[66] R. Hagedorn. Statistical Thermodynamics of Strong Interactions at High-Energies. *Nuovo Cim. Suppl. 3 (1965) 147.* 46

[67] N. M. Kroll and W. Wada. Internal Pair Production Associated with the Emission of High-Energy Gamma Rays. 47

[68] R. Brun et al. CERN Program Library Long Write-up, W5013, GEANT3 Detector Description and Simulation Tool, 1994. 48

[69] B. Abelev et al. (ALICE Collaboration). Light vector meson production in pp collisions at $\sqrt{s} = 7$ TeV. *Physics Letters B*, 710(45):557 – 568, 2012. 51

[70] B. Abelev et al. (ALICE Collaboration). Measurement of inelastic, single- and double-diffraction cross sections in proton–proton collisions at the LHC with ALICE. *Eur. Phys. J. C*, 2012. 52, 82

[71] S. van der Meer. ISR-PO/68-31, KEK68-64. 52

[72] L. Aphecetche, et al. Numerical Simulations and Offine Reconstruction of the Muon Spectrometer of ALICE. *ALICE Internal Note ALICE-INT-2009-044*. 53

[73] G. Chabratova, et al. Development of the Kalman filter for tracking in the forward muon spectrometer of ALICE. *ALICE Internal Note ALICE-INT-2003-002*. 53

[74] R. Aaij and et al. (LHCb Collaboration). Prompt charm production in *pp* collisions at $\sqrt{s}$ =7 TeV. Dec 2010. 61, 62

[75] R. Aaij and et al. (LHCb Collaboration). Measurement of $\sigma(pp \to b\bar{b}X)$ at $\sqrt{s}$ = 7 TeV in the forward region. *Physics Letters B*, 694(3):209 – 216, 2010. 61, 62

[76] M. Aguilar-Benitez et all. (NA27 Collaboration). *Z. Phys. C*, 50(405426), 1991. 62

[77] Antonio Uras. Light neutral mesons production in p-A collisions at $\sqrt{s}$ = 27.5 GeV with the NA60 Experiment. *Acta Phys.Polon.Supp.*, 5:465–470, 2012. 62

[78] P.Z. Skands. arXiv: 0905.3418 (2009). 62

[79] R. Barlow. Advanced statistical techniques in particle physics. *in Advanced Statistical Techniques in Particle Physics (2002)*, Grey College, Durham, 18 -22 March 2002. 70

[80] K. Aamodt et al. (ALICE Collaboration). Rapidity and transverse momentum dependence of inclusive J/ψ production in pp collisions at $\sqrt{s}$ = 7 TeV. *Physics Letters B*, 704(5):442 – 455, 2011. 71

[81] Arnaldi et al. (NA60 Collaboration). ϕ production in InIn collisions at 158AGeV. *The European Physical Journal C*, 64:1–18, 2009. 72

[82] P Abreu et al. (DELPHI Collaboration). Measurement of the spin density matrix for the ρ^0, K^0 and ϕ produced in Z0 decays. *Physics Letters B*, 406(3):271 – 286, 1997.

[83] J. H. Chen and al. (STAR Collaboration). Spin alignment of $K^{*0}(892)$ and (1020) mesons in Au+Au and p+p collisions at $\sqrt{s_{NN}} = 200$ GeV. *Journal of Physics G: Nuclear and Particle Physics*, 35(4):044068, 2008. 72

[84] B. Abelev and others (ALICE Collaboration). Inclusive J/ψ production in pp collisions at $\sqrt{s} = 2.76$ TeV. *Phys.Lett.*, B718:295–306, 2012. 89

[85] R. Aaij et all. (LHCb Collaboration). Measurement of the inclusive ϕ cross-section in pp collisions at $\sqrt{s} = 7$ TeV. *Physics Letters B*, 703(3):267 – 273, 2011. 104